Environmental Science & Technology

pubs.acs.org/est

Article

Mn(II)-Mediated Abiotic Humification via Synergistic Interactions with Molecular Oxygen

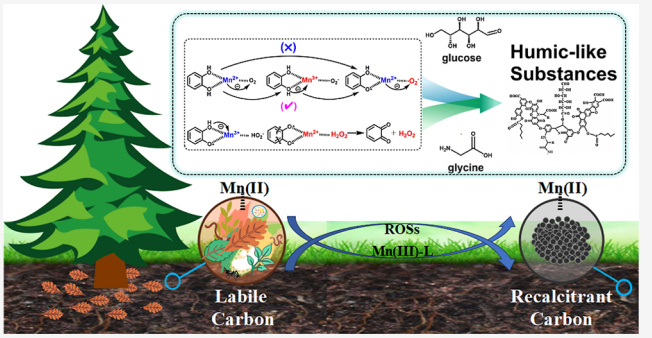
Feng Jiang,[#] Hong Su,[#] Qing-long Fu, Bruno Lanson, Xiaoming Wang, Hui Yin, Jingtao Hou, Wenfeng Tan,* Xionghan Feng,* and Caroline Peacock

Cite This: *Environ. Sci. Technol.* 2026, 60, 31669−31684

Read Online

ACCESS | Metrics & More | Article Recommendations | Supporting Information

ABSTRACT: Terrestrial organic carbon (OC) dynamics critically influence the global carbon budget. Humification is a key pathway for stabilizing OC by transforming labile compounds into macromolecular polymers. High-valent manganese oxides (e.g., $Mn(IV)O_2$) are well-known as efficient catalysts of abiotic humification, whereas the role of Mn(II) in OC transformation remains poorly understood. Here, dissolved Mn^{2+} drives oxidative polymerization and nitrogen-enriched humic-like product formation in the presence of common soil precursors—catechol, glycine, and glucose—through a synergistic interaction with molecular oxygen (O_2). Mechanistically, Mn^{2+} mediates sequential single-electron transfers from catechol to O_2, forming reactive intermediates that potentially couple with Maillard precursors to yield nitrogen-enriched macromolecules. FT-ICR-MS reveals that CHON species in lignin-like and highly condensed aromatic regions collectively account for 75.6% of total product relative abundance. This process is accompanied by the generation of reactive oxygen species (ROS), which could further enhance molecular diversity. Across 14 soil and freshwater DOM samples, 13.1−54.7% of assigned product formulas overlap with those in the corresponding DOM samples. Collectively, these shared formulas account for 78% of the total relative abundance of product formulas, indicating molecular-formula-level compositional similarity. These findings provide mechanistic and molecular-level insight into the underexplored role of Mn^{2+} in abiotic humification.



KEYWORDS: *soil organic matter, abiotic humification, catalytic polymerization, soluble Mn^{2+}, Mn-organic carbon interactions, FT-ICR MS*

1. INTRODUCTION

Soil organic carbon (SOC) strongly affects atmospheric CO_2 levels and global climate.[1,2] Globally, soils store an estimated 1500−2400 Pg C, roughly two to three times the carbon present in the atmosphere (~760 Pg C), and soil respiration releases approximately 68−101 Pg C yr^{-1} to the atmosphere.[1,2] Traditionally, mineral-organic matter association is regarded as the primary mechanism for stabilizing soil organic matter (SOM) against microbial respiration through physical isolation and sorptive interactions.[1,3−7] Yet mineral-mediated geopolymerization—transformation of simple organic molecules into chemically recalcitrant forms, via reactions like Maillard and polyphenol condensations, can enhance SOM molecular complexity and stability against degradation.[8−14] Recent studies emphasize mineral-mediated geopolymerization as an essential complementary pathway for stabilizing SOM and reducing CO_2 emissions,[12,15] while both iron (Fe)- and Mn-catalyzed transformations of simple organic molecules into complex macromolecules could sequester approximately 4.1 Tg C yr^{-1} in marine sediments,[16] underscoring the significance of reactive metal-catalyzed geopolymerization in carbon cycling. Given the abundance of reactive Fe/Mn and labile organic molecules in soils,[3,17−21] understanding the extent of geopolymerization processes appears essential for predicting the global carbon dynamics.

Mn biogeochemical cycling and organic carbon are strongly interlinked, with a notable correlation between Mn content in litter and decomposition rates across forest ecosystems.[22−27] In particular, Mn concentration is identified as the key factor influencing litter decomposition in forest biomes, where Mn redox cycling is tightly coupled to the formation of reactive Mn species and the oxidative breakdown of lignin and other aromatic litter components.[22], As plant material decomposes, polyphenols and quinones are released from tannins, lignins, and glycosides, potentially leading to the synthesis of

Received: August 7, 2026
Revised: October 16, 2026
Accepted: October 16, 2026
Published: October 27, 2026



Downloaded from pubs.acs.org/esthag/article-pdf/60/44/31669/6899314/acs.est.6c12201.pdf by UNIV GRENOBLE ALPES user on 10 November 2026

© 2026 American Chemical Society

secondary polymers through free radical coupling or nucleophilic reactions involving amino sugars and amino acids.[8,28−30] Mn(IV) oxides (e.g., birnessite) are widely reported to enhance the oxidative polymerization of polyphenols through semiquinone radical formation, a "browning" process recognized as a potential pathway for abiotic humic substance formation.[10−13,18,20,31−34] Yet the potential contributions of Mn species with other valence states in this process remain largely unknown.

In the abiotic transformation of organic matter, Mn(II) is commonly perceived as unreactive compared with higher-valent Mn(III) and Mn(IV), thus receiving limited attention in carbon transformation studies.[18] But it is found to be the most abundant Mn species in the organic surface layer ($\bar{x}$ = 54%), followed by Mn(III) ($\bar{x}$ = 32%) and Mn(IV) ($\bar{x}$ = 14%), based on analyses of temperate soil profiles.[35] In live foliage, Mn predominantly exists in its reduced form (i.e., Mn^{2+}), which can be released and redistributed during litter decomposition.[23] Recent investigation consistently suggests that Mn(II) primarily regulates humus soil C stocks in the boreal forest.[36] To date, Mn(II) has largely been regarded as a reducing agent rather than an active mediator of organic matter abiotic oxidation. Accordingly, its potential role in driving the oxidative polymerization of labile organic matter and subsequent abiotic humification remains poorly explored. Yet recent evidence suggests that Mn(II) may exhibit previously underestimated reactivity in phenol-rich, oxygenated systems.[33] Specifically, Mn(II)-catechol-dissolved oxygen reactions have been shown to induce oxidative transformation under neutral-to-alkaline conditions through the formation of transient Mn(III) intermediates.[33] This finding provides an important context for considering whether Mn(II)-mediated phenolic oxidation can further propagate into abiotic oxidative polymerization within a representative humification precursor system. Given the prevalence of Mn(II) and its coexistence with organic matter in terrestrial environments, this potential reactivity warrants a reassessment of the contribution of Mn(II) to soil organic matter formation and transformation.

The present study investigates the function of soluble Mn^{2+} in catalyzing the abiotic polymerization of catechol, glycine, and glucose, important humic precursors in soils, as model compounds of phenols, carbohydrates, and amino acids.[28,37] We acquired experimental evidence supporting an underexplored abiotic pathway in which the synergistic interplay between soluble Mn^{2+} and O_2 promotes oxidative polymerization and humification in such multiprecursor systems, leading to the formation and deposition of nitrogen-rich humic-like substances. The catalytic oxidation mechanism of Mn^{2+} in driving abiotic polymerization is elucidated using in situ electron paramagnetic resonance (EPR), in situ attenuated total reflectance-Fourier transform infrared (ATR-FTIR) spectroscopy, reactive oxygen species (ROS) trapping, X-ray absorption near edge structure (XANES) spectroscopy, and density functional theory (DFT) simulations. Fourier transform ion cyclotron resonance mass spectrometry (FT-ICR MS) and quadrupole-orbitrap high-resolution mass spectrometer (Q-Orbitrap-HRMS) analyses provide detailed molecular fingerprints and enable elucidation of the molecular composition of the resulting polymers. This study uncovers a previously overlooked abiotic role of soluble Mn^{2+} in organic matter transformation and provides mechanistic insight into a potential Mn-mediated pathway contributing to abiotic humification.

2. MATERIALS AND METHODS

Detailed information on the chemicals used is provided in Text S1.

2.1. Materials Preparation

δ-Mn(IV)O_2 (Birnessite) and γ-Mn(III)OOH (Manganite) were synthesized according to the method previously reported.[38,39] The successful synthesis of these minerals was confirmed by X-ray diffraction (XRD; Figure S1). The diffraction patterns are consistent with the corresponding standard reference data (δ-Mn(IV)O_2: JCPDS Card No. 80-1089; γ-MnOOH: JCPDS Card No. 74-1049), with no detectable impurity phases. The preparation of Mn(III)-PP stock solution followed the procedures outlined by Kostka et al.[40] In this study, $MnCl_2$ served as the source of soluble Mn^{2+}. Detailed preparation methods for δ-MnO_2, γ-MnOOH, and the Mn(III)-PP complex are provided in Text S2.

2.2. Incubation Experiment

Incubation experiments were conducted in 250 mL Erlenmeyer flasks kept at 25 °C in the dark, with mechanical stirring at 300 rpm under ambient oxygen conditions. Dark conditions were used to minimize potential photochemical interferences, such as phenolic photooxidation, light-induced Mn redox transformation, and ligand-to-metal charge transfer (LMCT) processes.[41−43] A solution containing 2 mM catechol (CT), 6 mM glycine (Gly), and 6 mM glucose (Glu), designated as CGG, was prepared in 250 mL of boric acid-sodium borate buffer (0.05 M, pH 8.00 ± 0.1). These precursor concentrations are identical to those used in previous studies on model polyphenol−Maillard humification systems.[44,45] The borate buffer was chosen for its noninterference with Mn^{2+} and bacteriostatic properties,[46] which were confirmed to ensure an abiotic environment (Figure S2). Reactions were initiated by adding 2 mM $MnCl_2$. This Mn(II) concentration is higher than typical levels in bulk soil solutions and was selected as a Mn-enriched model condition to accelerate reaction kinetics, enhance the detectability of transient reaction features, and enable in situ monitoring of dynamic polymerization processes. Mn^{2+} concentration-dependent experiments were further conducted over 0.1−6.0 mM to assess the role of Mn^{2+} availability. Anaerobic (N_2) experiments were conducted under ultrapure nitrogen (>99.999% N_2), whereas aerobic (O_2) experiments were conducted under ambient air. A CO_2-free synthetic air control (21% O_2 and 79% N_2, v/v) was included to distinguish the effects of O_2 removal from those of CO_2 depletion during N_2 purging. To assess the transient presence of Mn(III), a 40 mM pyrophosphate (PP) solution was added in dedicated experiments. The reaction solutions were subsequently monitored by UV−visible spectroscopy to track the formation of the Mn(III)−PP complex. To compare the roles of different manganese species in driving humification, δ-MnO_2, γ-MnOOH, and Mn(III)−PP complex were evaluated at an equal Mn concentration of 2 mM under identical reaction conditions. In parallel, the effect of phenolic precursor type was evaluated using catechol (CT), hydroquinone (Hyd), resorcinol (Re), and phenol (Phe). To ensure consistent comparison among different Mn species and phenolic precursors, pH 8.0 was used as a mechanistically favorable condition. This pH is widely adopted in mechanistic studies on Mn oxide−DOM interactions, especially those probing organic matter polymerization pathways.[11,13,16,20,47] Although forest litter layers are typically acidic to neutral, mildly alkaline conditions also occur in certain forest soils and adjacent aquatic systems.[48−51] To further evaluate the effect of pH, additional pH-dependent experiments were conducted over pH 6.0−8.0. During the incubation, 3 mL aliquots of the reaction mixture were withdrawn at various time intervals, filtered through a 0.45 μm filter, and the resulting brown-black solid was centrifuged, washed with deionized water, and freeze-dried for subsequent characterization. The humic-like acid (HLA) and fulvic-like acid (FLA) formed after the reaction were extracted and purified following the protocol of the international humic substances society (IHSS), and their concentrations were quantified by dissolved organic carbon (DOC) analysis (see Text S3 for details). Similar operational fractionation approaches have been used to quantify humic-like fractions in abiotic humification, mineral-mediated

Downloaded from pubs.acs.org/esthag/article-pdf/60/44/31669/6899314/acs.est.6c12201.pdf by UNIV GRENOBLE ALPES user on 10 November 2026

https://doi.org/10.1021/acs.est.6c12201
Environ. Sci. Technol. 2026, 60, 31669−31684

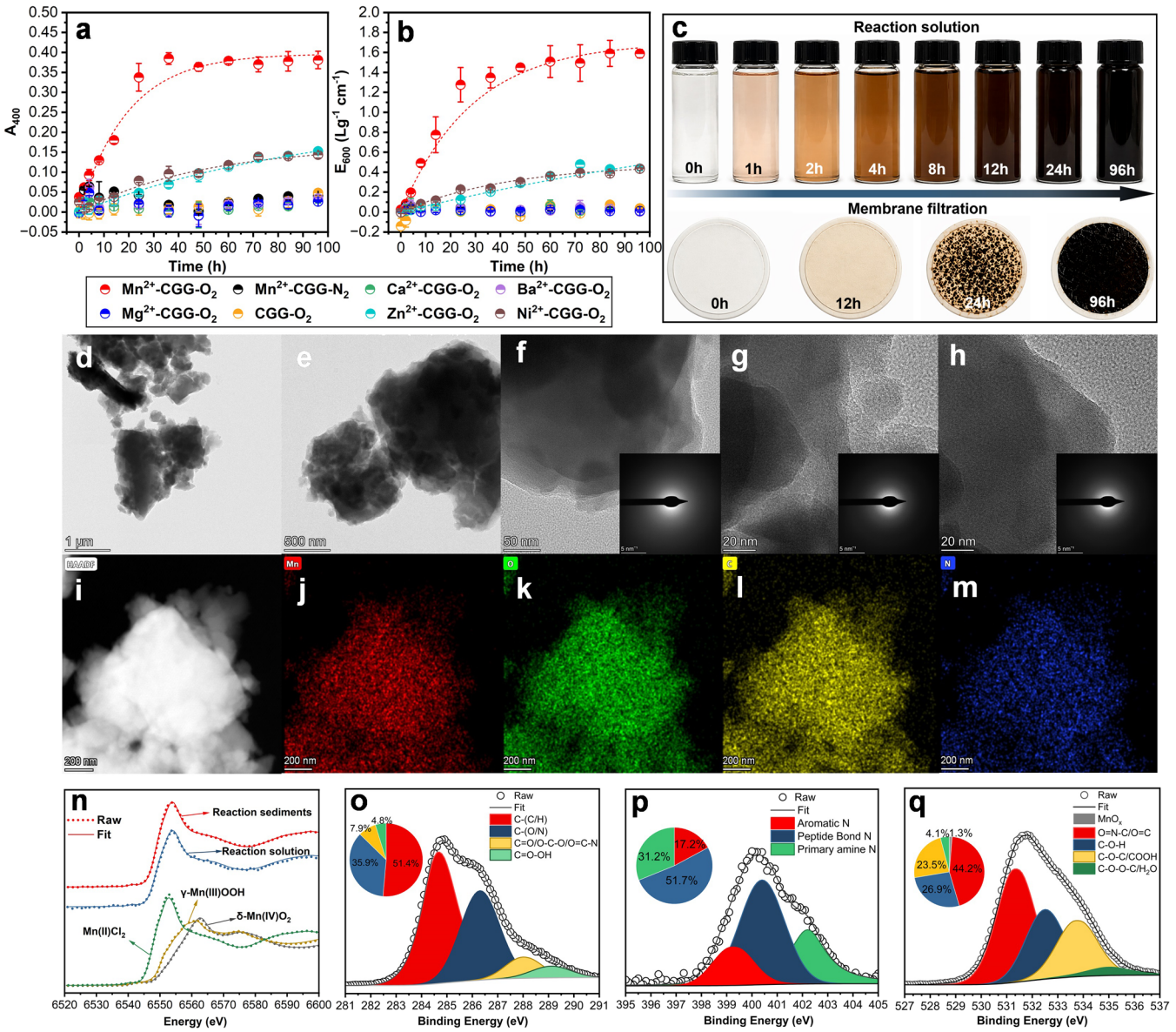


Figure 1. Kinetics and precipitation-product characterization of Mn^{2+}-driven humification. (a,b) Temporal changes in (a) A_{400} and (b) E_{600} of CGG (catechol−glucose−glycine) solutions reacting with Mn^{2+}, Ca^{2+}, Ba^{2+}, Mg^{2+}, Ni^{2+}, and Zn^{2+} under oxic (O_2) conditions, Mn^{2+}−CGG under N_2, and a cation-free control. Data are presented as mean ± SD (n = 3). (c) Visual appearance and physical state of the reaction solutions during humification. (d,e) Low-magnification TEM image and (f−h) high-resolution TEM (HRTEM) images with corresponding SAED patterns (insets) acquired from three representative regions. (i−m) EDS elemental mapping of a representative aggregate: HAADF image (i) and Mn (j), C (k), O (l), and N (m) distributions. (n) Mn K-edge XANES spectra of reaction precipitates and solutions. (o−q) High-resolution XPS spectra of C 1s (o), N 1s (p), and O 1s (q) for the precipitates.

oxidative polymerization, and composting systems.[44,45,52−54] Key quantitative data sets supporting the main conclusions were obtained from three independent experiments unless otherwise stated in the corresponding figure captions. In all figures, n denotes the number of independent experiments, and error bars represent mean ± SD.

2.3. Physicochemical Characterization and Mechanistic Simulations

UV−vis spectroscopy was employed to measure the absorbance of the reaction filtrate. The absorbance at 400 nm (A_{400}) was recorded, and the extinction coefficient at 600 nm (E_{600}) was calculated to evaluate the extent of humification.[9,14,54] DOC and total nitrogen (TN) were quantified using a multi-N/C analyzer. Mn concentrations were confirmed via atomic absorption spectroscopy (AAS). Catechol concentrations were quantified using high-performance liquid chromatography (HPLC). Fluorescence characteristics were subsequently characterized by excitation−emission matrix (EEM) analysis after removing dissolved Mn^{2+} with a cation-exchange resin to minimize cation-related fluorescence interference. The CO_2 production was quantified using a gas chromatograph (Agilent 8890 GC, Germany) equipped with a thermal conductivity detector. The production of hydrogen peroxide (H_2O_2) was measured according to established protocols,[55] and reactive oxygen species (ROS) were detected using electron paramagnetic resonance (EPR) spectroscopy. EPR further elucidated the unpaired electron structure of the formed HLA, enabled the detection of semiquinone radicals generated during the reaction, and allowed in situ monitoring of changes in the Mn^{2+} spin signal. X-ray diffraction (XRD) and high-resolution transmission electron microscopy (HRTEM) with energy dispersive spectrometry (EDS) were used to characterize the crystal phase, morphology, and elemental distribution of the reaction deposits. X-ray photoelectron spectroscopy (XPS) provided insights into surface elemental

Downloaded from pubs.acs.org/esthag/article-pdf/60/44/31669/6899314/acs.est.6c12201.pdf by UNIV GRENOBLE ALPES user on 10 November 2026

https://doi.org/10.1021/acs.est.6c12201
Environ. Sci. Technol. 2026, 60, 31669−31684

composition and Mn oxidation states, while the Mn X-ray absorption near-edge structure (XANES) spectroscopy was employed to further determine Mn valence states using the Combo method.[56] Attenuated total reflectance-Fourier transform infrared spectroscopy (ATR-FTIR) was utilized to identify surface functional groups of humic-like acid (HLA), and density functional theory (DFT) simulations were conducted to explore the catalytic oxidation mechanisms of Mn(II) during the polymerization process. Comprehensive details of the aforementioned calculations and characterization methods are provided in Text S4.

2.4. Molecular-Level Characterization via Mass Spectrometry Analysis

To characterize changes in molecular composition during polymerization, aliquots collected at 2, 8, and 24 h from one of three independent replicate reactions were analyzed using a 7 T FT-ICR MS instrument (Solarix XR, Bruker, Germany) equipped with an electrospray ionization (ESI) source operated in negative-ion mode.[57] Before analysis, samples were subjected to solid-phase extraction (SPE) using Bond Elut PPL columns (Agilent, USA; 500 mg/6 mL),[29] which yielded a DOC recovery of >58% (Text S5). The mass-to-charge ratio (m/z) data were collected within the range of 100−1000 Da with 450 scans and 0.5 s ion accumulation time. Peaks with a signal-to-noise ratio (S/N) ≥ 4 were identified, and molecular formulas were assigned using our FTMSDeu algorithm,[58] with elemental combinations constrained to $C_{\geq 3}H_{\geq 1}O_{\geq 1}N_{0-3}S_{0-1}$ and mass tolerances of <1.0 ppm. Additional constraints included 0 ≤ O/C ≤ 1.2, 0.3 ≤ H/C ≤ 2.5, and −10 ≤ DBE-O (double bond equivalent minus oxygen) ≤10. The relative abundance (RA) of each molecule was calculated as its peak intensity divided by the sum of the intensities of all detected molecules, whereas the relative intensity (RI) was determined by normalizing its peak intensity to that of the molecule with the highest intensity. Energy-resolved MS/MS was performed on 3 representative high-mass CHON ions detected in the reaction products (m/z 324.062639, 466.089203, and 574.110334) by CID at 0−12.5 eV to probe their fragmentation behavior and structural features. Detected compounds were classified into major biochemical classes based on O/C and H/C ratios (Table S1). The parameters such as m/z, H/C, O/C, N/C, modified aromaticity index (AI_{mod}), double bond equivalent per carbon (DBE/C), and nominal oxidation state of carbon (NOSC) were employed to describe the molecular properties of the reaction products, and the related calculations are summarized in Text S6. Kendrick mass defect (KMD) analysis was employed to identify homologous series with variations in COOH, OH, and NH_2 groups (Text S7). Molecular networks were constructed by identifying molecules with a specific m/z difference of $n \times 108.02113$ using Python to visualize the semiquinone radical coupling products. Edge and node files were generated to represent molecular connections, and networks were plotted using Gephi software (version 0.9.4). To evaluate the molecular similarity between the Mn^{2+}-catalyzed products and natural organic matter, 14 environmental dissolved organic matter (DOM) samples derived from soils and aquatic environments were used for comparative analysis. Given the inherent analytical constraints of FT-ICR MS (i.e., limited m/z range), the selectivity of SPE, and incomplete electrospray ionization of complex DOM, certain molecular species might not be fully captured during analysis. Accordingly, this comparative analysis reflects only the overlap of detectable molecular formulas and should not be interpreted as direct evidence for structural equivalence between the reaction products and natural DOM. Descriptions of these samples are provided in Text S8, with their types and collection sites listed in Table S2. High-resolution mass spectrometry (HRMS) using a quadrupole-Orbitrap mass spectrometer (QExactive, Thermo Fisher Scientific, USA) was performed on the reaction solution via electrospray ionization (ESI) in both positive and negative ion modes, yielding additional molecular information on the reaction products.

3. RESULTS AND DISCUSSION

3.1. Mn(II)-Catalyzed Formation and Precipitation of Humic-Like Substances via Synergistic Interaction with Molecular Oxygen

Comparative humification assays using δ-Mn(IV)O_2, γ-Mn(III)OOH, Mn(III)−PP complex, and dissolved Mn^{2+} within a catechol−glucose−glycine (CGG) model system reveal distinct kinetic and compositional differences (Figure S3). Under identical Mn-normalized conditions, Mn^{2+} exhibits the most pronounced increases in humification indices (A_{400} and E_{600}) over 96 h (Figure S3a,b), indicating greater chromophore development and aromatic condensation relative to the tested higher-valent Mn species. Consistently, Mn^{2+} yields the highest humic-like acid (HLA) concentration (Figure S3c) and comparatively low fulvic-like acid (FLA) production (Figure S3d), resulting in a markedly elevated HLA/FLA ratio (Figure S3e). These differences reflect fundamentally distinct reaction pathways and accessible reactive interfaces among dissolved Mn^{2+}, Mn(III)−PP complexes, and solid Mn(III/IV) oxides. Therefore, the observed trends reflect Mn-normalized system-level humification outcomes across both heterogeneous and homogeneous regimes, rather than intrinsic differences in catalytic activity. Nevertheless, the strong participation of Mn^{2+} in humic-like polymer formation is notable given its traditionally lower perceived redox reactivity and its underrepresentation in abiotic humification frameworks.[11−13,18,37] Motivated by these observations, we subsequently sought to elucidate the fundamental mechanisms underlying Mn^{2+}-driven humification.

Control assays under anoxic conditions reveal that Mn^{2+} induces only minimal UV−vis spectral changes, whereas under oxic conditions it induces a pronounced red shift (Figure S4a−c) accompanied by increased A_{400} and E_{600} values (Figure 1a,b). Humification-associated spectral evolution is also retained under CO_2-free aerobic conditions, indicating that the suppressed transformation under N_2 cannot be attributed simply to CO_2 removal (Figure S4d). These findings support a humification pathway involving synergistic interactions between Mn^{2+} and O_2 and indicate that nonredox precursor association mediated by cation bridging alone is insufficient to account for the observed humification in the absence of O_2.[16] This interpretation is further supported by cation-exchange resin treatment of selected reaction aliquots immediately before UV−vis analysis. After removal of most dissolved Mn, the time-dependent spectral evolution and A_{400} increase are largely retained, although slightly attenuated (Figure S5), supporting organic chromophore formation as the major contributor to the optical response rather than residual Mn-associated optical contributions or reversible Mn-induced association. Similarly, alkaline earth metals (Ca^{2+}, Mg^{2+}, and Ba^{2+}) produce no significant UV−vis spectral shifts (Figure S4e−g) or changes in A_{400} and E_{600} (Figure 1a,b), even under O_2 conditions, indicating that nonspecific electrostatic interactions are insufficient to account for the observed transformation. To further probe metal−precursor coordination, Ni^{2+} and Zn^{2+} were used as coordination-capable divalent-metal controls (Figure S4h,i). Both metals have been reported to form inner-sphere complexes with phenolic donors, with catecholate complexation stability constants (log K_1) of 8.92 and 9.90, respectively, compared with 7.72 for Mn^{2+}.[59] Under oxic conditions, both Ni^{2+} and Zn^{2+} cause measurable increases in A_{400} and E_{600} and UV−vis spectral

Downloaded from pubs.acs.org/esthag/article-pdf/60/44/31669/6899314/acs.est.6c12201.pdf by UNIV GRENOBLE ALPES user on 10 November 2026

https://doi.org/10.1021/acs.est.6c12201
Environ. Sci. Technol. 2026, 60, 31669−31684

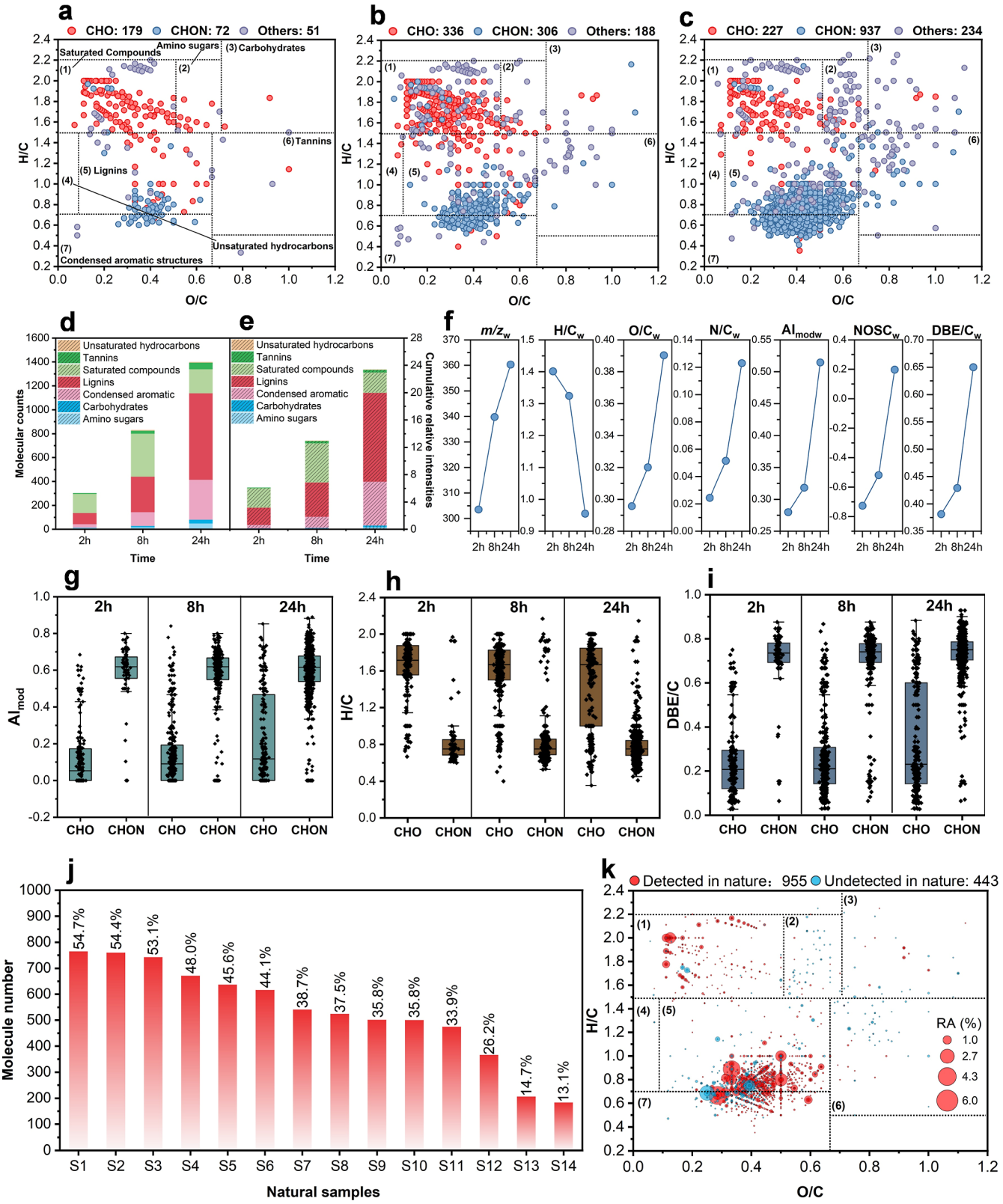


Figure 2. Molecular characterization of polymerization products from Mn^{2+}−CGG reactions by FT-ICR MS. (a−c) Van Krevelen diagrams of reaction products at 2 h (a), 8 h (b), and 24 h (c). (d) Total molecular counts and (e) cumulative relative intensities categorized by biochemical classes. (f) Temporal variations in intensity-weighted average molecular indices, including mass-to-charge ratio (m/z_w), hydrogen-to-carbon (H/C_w), oxygen-to-carbon (O/C_w), nitrogen-to-carbon ratio (N/C_w), modified aromaticity index (AI_{modw}), nominal oxidation state of carbon ($NOSC_w$), and double bond equivalent per carbon (DBE/C_w). (g−i) Distribution of CHO and CHON formulas in terms of (g) AI_{mod}, (h) H/C, and (i) DBE/C at 2, 8, and 24 h. (j) Comparison of molecular formulas shared between the reaction products and natural organic matter samples from soils and freshwaters, showing total counts and matching rates (proportion of product molecules detected in natural samples). (k) Van Krevelen diagram showing the distribution of formulas detected or not detected in natural samples; RA denotes relative abundance.

Downloaded from pubs.acs.org/esthag/article-pdf/60/44/31669/6899314/acs.est.6c12201.pdf by UNIV GRENOBLE ALPES user on 10 November 2026

https://doi.org/10.1021/acs.est.6c12201
Environ. Sci. Technol. 2026, 60, 31669−31684

shifts, although their effects remain significantly weaker than those of Mn^{2+} (Figures 1a,b and S4h,i). These results suggest that Mn^{2+}-initiated humification is associated with inner-sphere metal−precursor coordination, which may facilitate subsequent oxidative polymerization. The substantially stronger effect of Mn^{2+} relative to Ni^{2+} and Zn^{2+} may be associated with its more favorable redox properties, potentially facilitating ligand-assisted electron transfer between coordinated precursors and O_2.

This $Mn^{2+}-O_2$ coupled humification process is pH-dependent, proceeding across the pH range of 6.0−8.0 and increasing with alkalinity (Figure S6), consistent with previous reports that higher pH favors polyphenol condensation and the progression of Maillard reactions.[10,11,13,29] Mechanistically, higher pH may promote phenolic deprotonation, thereby enhancing both coordination with Mn^{2+} and the oxidizability of the precursors, while also shifting Mn^{2+} speciation toward hydrolyzed forms such as $MnOH^+$, which is more favorable for inner-sphere electron transfer to O_2.[60] Together, these changes likely facilitate ligand-assisted electron transfer from Mn^{2+}−precursor complexes to O_2, thereby promoting the O_2-coupled oxidative transformation underlying humification. The efficiency of Mn^{2+}-driven humification is also modulated by phenolic precursor structure (Figure S7; details in Text S9). In the absence of Mn^{2+}, the hydroquinone-containing system exhibits the strongest spontaneous oxidative polymerization (highest A_{400} in Figure S7a), likely because hydroquinone is susceptible to autoxidation by O_2, consistent with its stronger electron-donating ability and lower stability as indicated by Frontier molecular orbital calculations (higher E(HOMO) and smaller E_g; Figure S7f). In contrast, in the presence of Mn^{2+}, humification enhancement follows the order catechol > resorcinol > hydroquinone > phenol, as reflected by increases in E_{600} and HLA yield (Figure S7d,e), indicating that humification efficiency is not governed by intrinsic molecular stability alone. Instead, as discussed in Text S9, the observed trend is more consistent with differences in phenolic pK_a values and hydroxyl substitution patterns. In particular, the lower pK_a of catechol and its ortho-positioned hydroxyl groups may facilitate phenoxide formation and Mn^{2+} coordination, potentially favoring electron transfer from Mn-phenolate complexes to O_2 and thereby enhancing Mn^{2+}-driven oxidative polymerization.

Furthermore, to evaluate the robustness of the Mn^{2+}−CGG system under ligand-amended conditions, we introduced oxalate (OA), citrate (CA), and pyruvate (PYR) at a 1:1 molar ratio to Mn^{2+} (Figure S8). UV−vis spectra and kinetic analyses show that humification proceeds in all ligand-amended systems (Figure S8a−e), indicating that ligand complexation does not abolish the Mn(II)−O_2-coupled pathway. However, the ligands modulate product distribution: OA and CA moderately reduce HLA yields from ∼90 to 73−78 mg L^{-1}, whereas PYR has only a minor effect, with HLA remaining at ∼86 mg L^{-1} (Figure S8f). Meanwhile, all ligands promote FLA formation and lower the HLA/FLA ratio, suggesting a shift toward lower-molecular-weight fractions, consistent with partial limitation of Mn(II) availability by ligand complexation (Figure S8g,h). Nevertheless, despite ligand-induced suppression of HLA formation, substantial HLA production indicates that the Mn(II)−O_2-driven humification pathway remains effective under the present ligand-amended conditions.

During the reaction between CGG and Mn^{2+}, the reaction mixture gradually darkens, yielding a brown−black precipitate (Figure 1c), accompanied by decreases in catechol (CT), dissolved Mn, dissolved organic carbon (DOC), and total nitrogen (TN) concentrations under O_2 (Figure S9a−d). Dissolved inorganic carbon (DIC) shows no appreciable accumulation under either oxic or anoxic conditions, while CO_2 production is detected in CO_2-free air but accounts for less than 0.3% of the initial carbon and remains negligible under N_2, indicating that mineralization contributes only minimally to the overall carbon loss during the reaction (Figure S9e−g). Transmission electron microscopy (TEM; Figure 1d−h) and selected-area electron diffraction (SAED; Figure 1f−h) indicate that the precipitates are amorphous, consistent with the absence of crystalline phases observed in the XRD pattern (Figure S10a). EDS mapping further reveals homogeneous distributions of Mn, O, C, and N (Figures 1i−m and S10b). High-resolution Mn 3s XPS results indicate an average oxidation state of 2.1 (Figure S10c), corroborated by Mn K-edge XANES (Figure 1n and Table S3), which confirms Mn(II) as the dominant species in both reaction-formed sediments and the coexisting solution. Deconvolution of high-resolution C 1s, N 1s, and O 1s XPS spectra (Figure 1o−q and Table S4) identifies major functional groups, including aromatic/aliphatic carbon (C−(C, H)), peptide-bound nitrogen, and carbon- or nitrogen-bound oxygen (O═C/O═N−C). Furthermore, in the N 1s region, pristine glycine exhibits a single symmetric peak at ∼401.7 eV (Figure S10d,e), assigned to the protonated primary amine ($-NH_3^+$) of zwitterionic glycine.[61] In contrast, the precipitate from the Mn(II)-driven CGG reaction exhibits a broadened N 1s spectrum extending toward lower binding energy, with aromatic N (399.2 eV, 17.2%) and peptide bond N (400.4 eV, 51.7%) together accounting for 68.9% of total N (Figure 1p). Together with the humic-like characteristics established above, this supports the incorporation of glycine-derived N into the newly formed humic-like products. Additional details on polymerization and precipitation under varying Mn^{2+} concentrations, along with excitation−emission matrix (EEM), ATR-FTIR, and EPR analyses, are provided in Figures S11−S15 and discussed in Text S10. Overall, elevated Mn^{2+} levels accelerate oxidative conversion of precursors to HLA, enhance charge- and hydrophobic-driven self-assembly of HLA−Mn(II) complexes, and induce selective precipitation of highly aromatic macromolecular fractions.

3.2. Temporal Evolution of Molecular Compositions during Humification and Comparison with Natural Organic Matter

FT-ICR MS analysis (Figure S16) reveals the temporal evolution of molecular compositions during the interaction of CGG with Mn^{2+}(Figure 2a−c). After 2, 8, and 24 h of reaction time, 302, 829, and 1398 molecular formulas are identified, respectively, indicating increasing molecular diversity. Compounds are dominated by lignin-like (RA = 38.8−55.6%), saturated (RA = 12.7−46.7%), and condensed aromatic-like (RA = 8.2−27.4%) classes, with cumulative relative intensities (Figure 2d,e) showing a progressive enrichment of lignin-like and condensed aromatic structures, suggesting their potential role as nuclei for HLA formation.[62] Intensity-weighted molecular indices (Figure 2f) reveal increasing mass-to-charge ratio (m/z), oxygen-to-carbon ratio (O/C), nitrogen-to-carbon ratio (N/C), modified aromaticity

Downloaded from pubs.acs.org/esthag/article-pdf/60/44/31669/6899314/acs.est.6c12201.pdf by UNIV GRENOBLE ALPES user on 10 November 2026

https://doi.org/10.1021/acs.est.6c12201
Environ. Sci. Technol. 2026, 60, 31669−31684

index (AI_{mod}), nominal oxidation state of carbon (NOSC), and double bond equivalents per carbon (DBE/C), with decreasing hydrogen-to-carbon ratio (H/C), indicating a shift toward molecules that are more aromatic, unsaturated, highly condensed, and enriched in nitrogen and oxygen.

Glycine participation in progressive polymerization is supported by the marked increase in the number and relative abundance of assigned CHON formulas, from 72 (RA = 18.9%) at 2 h to 937 (RA = 76.9%) at 24 h (Figure 2a−c). Because free glycine (M_W = 75.067) falls below the FT-ICR MS detection range (m/z 100−1000), the detected CHON formulas represent N-containing products with molecular masses greater than that of glycine. As the reaction progresses, CHON formula counts increase substantially in the m/z 300−400, 400−500, and ≥500 intervals (Figure S17), indicating the formation of higher-molecular-mass N-containing products. Moreover, CHON compounds assigned to the lignin-like and highly condensed aromatic regions together account for 75.6% of the total assigned product relative abundance at 24 h (Figure 2a−c), indicating a preferential accumulation of N-containing molecular structures with aromatic and highly condensed characteristics. Consistently, CHON species exhibit higher AI_{mod} and DBE/C values and lower H/C ratios than CHO species, further indicating more unsaturated, aromatic, and condensed compositions (Figure 2g−i). To gain further insight into the association of N with the product frameworks, energy-resolved MS/MS was performed on three representative CHON ions at m/z 324.062639, 466.089203, and 574.110334, assigned to $C_{16}H_{11}O_5N_3$, $C_{22}H_{17}O_9N_3$, and $C_{28}H_{21}O_{11}N_3$, respectively (Figure S18). Increasing the collision energy from 0 to 7.5, 10, and 12.5 eV promotes precursor-ion dissociation and product-ion formation (Figure S18a,b). At 12.5 eV, precursor-ion intensities decrease by 64.4%, 63.5%, and 78.5%, respectively, relative to those at 0 eV, while their contributions to the summed intensity of the assigned major ions fall to 22.9%, 20.4%, and 13.2%. Accurate-mass differences support fragmentation pathways dominated by neutral losses of CO_2, H_2O, and CH_2, whereas product ions associated with loss of the N-containing neutral C_2H_3NO are less abundant (Figure S18b,c). Specifically, sequential H_2O and CH_2 losses from m/z 324.062639 yield product ions at m/z 306.051646 and 292.036366, with no assigned product ion indicating loss of an N-containing moiety. For m/z 466.089203, successive CO_2 losses generate N_3-retaining product ions at m/z 422.099502 and 378.109543, which together account for 57.1−67.8% of the summed assigned-ion intensity at collision energies of 7.5−12.5 eV. In contrast, the N_2-containing product ion at m/z 321.088078, attributed to subsequent C_2H_3NO loss, contributes only 4.7−12.6%. Similarly, m/z 574.110334 yields two N_3-retaining product-ion series through successive CO_2 losses (m/z 530.120499 and 486.130676) and CH_2 loss from m/z 530.120499 followed by CO_2 loss (m/z 516.104502 and 472.114928) (Figure S18c). At 12.5 eV, these four ions collectively account for 82.9% of the summed assigned-ion intensity, whereas the N_2-containing product ion at m/z 429.108905, attributed to C_2H_3NO loss from m/z 486.130676, is detected only at this energy and contributes 4.0%. Thus, all assigned fragments retain N, and N_3-containing products dominate throughout the collision-energy series. Such preferential N retention during extensive precursor-ion dissociation, together with the increasing diversity of higher-mass CHON formulas and their aromatic and condensed compositional characteristics, supports glycine-derived N incorporation into the products formed during polymerization.

To evaluate the potential environmental relevance of Mn^{2+}-catalyzed polymerization, we compare the detectable molecular formulas of its products with those identified in 14 soil and freshwater DOM samples (Table S2). A substantial fraction of product molecular formulas (13.1−54.7%, sample-dependent) overlap with formulas assigned in individual environmental samples (Figure 2j). Variation in formula-matching rate among environmental samples is associated with the bulk molecular characteristics of DOM, with higher matching rates generally observed in samples exhibiting higher DBE/C_w, AI_{modw}, N/C_w, $NOSC_w$, and O/C_w, but lower H/C_w (Figure S19). These compositional trends are consistent with the more oxidized, unsaturated, and aromatic molecular features typically associated with more highly humified DOM.[62,63] Across the full sample set, 955 molecular formulas, corresponding to 68.3% of all detected product formulas, overlap with molecular formulas detected across the analyzed environmental DOM samples (Figure 2k). These overlapping formulas account for 78% of the total product relative abundance, suggesting molecular-formula-level compositional similarity between Mn^{2+}-catalyzed products and environmental DOM. Yet, as a given molecular formula can encompass multiple isomeric structures, the observed overlap supports formula-based comparison rather than indicating structural equivalence.

3.3. The Catalytic Oxidation Mechanism of Mn(II) for Polymerization Reaction

To elucidate the mechanism of Mn^{2+}-catalyzed oxidative polymerization, ROS commonly involved in O_2-based reactions, including H_2O_2, $^{\bullet}O_2^-$, and $^{\bullet}OH$ were investigated. In particular, synergistic catalysis of H_2O_2 formation from Mn^{2+}, O_2, and CGG interactions is demonstrated by using a UV−vis colorimetric assay, which reveals a characteristic H_2O_2 absorption peak at 352 nm only when the three components coexist (Figure S20a−h).[55,64] Quantitative data show H_2O_2 concentration reaching a maximum of 0.166 mM before declining (Figure S20i). H_2O_2 is generated during Mn^{2+}-catalyzed CT oxidation by O_2, as supported by the absence of appreciable humification in CT-free systems (Figure S21) and the lack of detectable H_2O_2 formation in the absence of CT over the 96 h reaction period (Figure S20g). The subsequent decline in H_2O_2 concentration likely reflects progressive CT depletion, which limits the availability of precursors for continued H_2O_2 production, together with the concurrent consumption or decomposition of the H_2O_2 already formed. Similar O_2-to-H_2O_2 reduction by Mn^{2+}−catecholate complexes has been reported previously.[65] Mechanistically, H_2O_2 formation from O_2 may proceed via two distinct pathways, a concerted two-electron reduction (eq 1) or a two-step single-electron reduction process (eqs 2 and 3).[55,64,66]

$$O_2 + 2H^+ + 2e^- \rightarrow H_2O_2 \quad (1)$$

$$O_2 + e^- \rightarrow \text{superoxide radicals}(^{\cdot}O_2^-) \quad (2)$$

$$^{\cdot}O_2^- + 2H^+ \rightarrow H_2O_2 \quad (3)$$

As inferred from the equations, H_2O_2 formation via two consecutive single-electron transfers proceeds with $^{\bullet}O_2^-$ as a key intermediate. EPR spin trapping with DMPO in methanol reveals the characteristic 6-line DMPO−$^{\bullet}O_2^-$ signal after 5 min in the Mn^{2+}−CGG system, whereas the corresponding signal is negligible in both the Mn^{2+}-only and CGG-only

Downloaded from pubs.acs.org/esthag/article-pdf/60/44/31669/6899314/acs.est.6c12201.pdf by UNIV GRENOBLE ALPES user on 10 November 2026

https://doi.org/10.1021/acs.est.6c12201
Environ. Sci. Technol. 2026, 60, 31669−31684

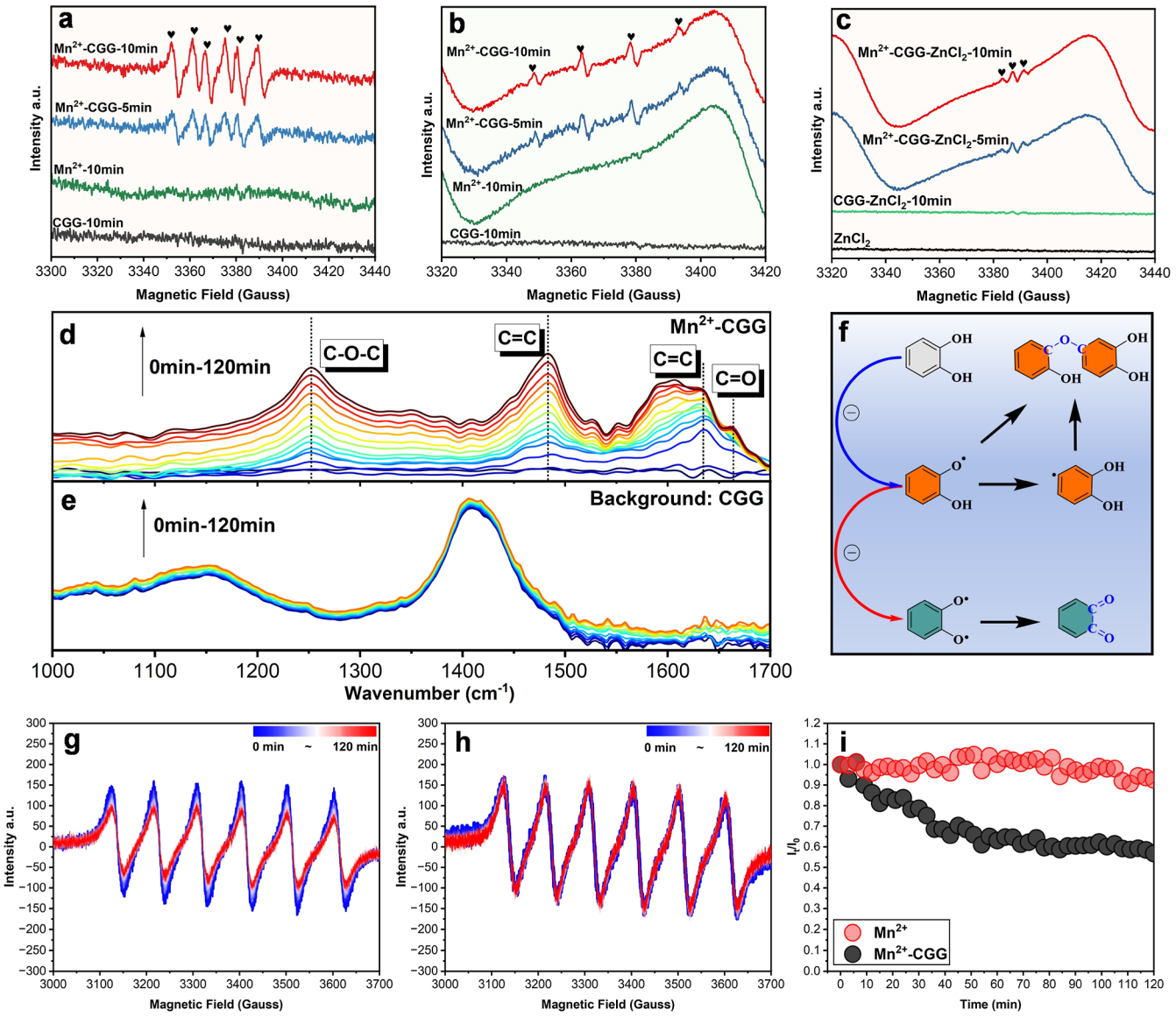


Figure 3. Determination of reactive species generated during the reaction. (a) Detection of superoxide radicals ($^{\bullet}O_2^-$). (b) Detection of hydroxyl radicals ($^{\bullet}OH$). (c) Detection of semiquinone radicals stabilized with $ZnCl_2$ as a complexing agent. (d) In situ ATR-FTIR spectra of the Mn^{2+} interaction with CGG. (e) In situ ATR-FTIR spectra of CGG in the absence of Mn^{2+}. (f) Proposed formation pathways of the corresponding functional groups based on the ATR-FTIR spectra of the Mn^{2+}−CGG interaction. (g) In situ EPR monitoring of Mn^{2+} paramagnetic signals in the presence of CGG and (h) without CGG. (i) Variations in spin signal intensity (average of maximum intensities from 6 peaks).

controls under otherwise identical conditions (Figure 3a). This observation is consistent with the proposed two-step single-electron-transfer pathway. Detection of a DMPO−$^{\bullet}$OH adduct with the characteristic 1:2:2:1 quartet signal in aqueous solution further indicates $^{\bullet}$OH generation in the Mn^{2+}−CGG system, whereas the corresponding controls show no clearly detectable signal (Figure 3b).[66] These reactive radicals may further oxidize organic molecules, enhancing molecular diversity. Additionally, single-electron oxidation of catechol units can generate organic radical species bearing unpaired electrons, such as semiquinone radicals. Such radicals can be stabilized through bidentate chelation with Zn(II) and detected by EPR.[67,68] Figure 3c shows pronounced EPR signals characteristic of semiquinone radicals after the Mn^{2+}−CGG reaction,[67,68] whereas only a negligible signal appears in the absence of Mn^{2+}. This detection of semiquinone radicals further supports the occurrence of single-electron-transfer processes during the reaction.

In situ flow infrared spectroscopy (Figure 3d,e) was employed to track time-resolved spectra during the reaction of Mn^{2+} with CGG. The CGG-only spectrum remains nearly unchanged during the first 120 min (Figure 3e), confirming the stability of the CGG background during the measurement. The spectra in Figure 3d are background-corrected using the spectrum of the initial CGG solution before Mn^{2+} addition as the reference, so the emerging bands reflect Mn^{2+}-induced spectral changes relative to the original CGG matrix. Upon Mn^{2+} addition, distinct peaks gradually emerge at 1252, 1484, 1636, and 1660 cm^{-1} (Figure 3d). The bands at 1252 and 1484 cm^{-1} can be assigned to aryl ether C−O−C bonds and aromatic C═C vibrations, respectively.[69,70] Peak deconvolution of the 1550−1700 cm^{-1} region further resolves evolving components centered at approximately 1589, 1612, 1635, and

https://doi.org/10.1021/acs.est.6c12201
Environ. Sci. Technol. 2026, 60, 31669−31684

Downloaded from pubs.acs.org/esthag/article-pdf/60/44/31669/6899314/acs.est.6c12201.pdf by UNIV GRENOBLE ALPES user on 10 November 2026

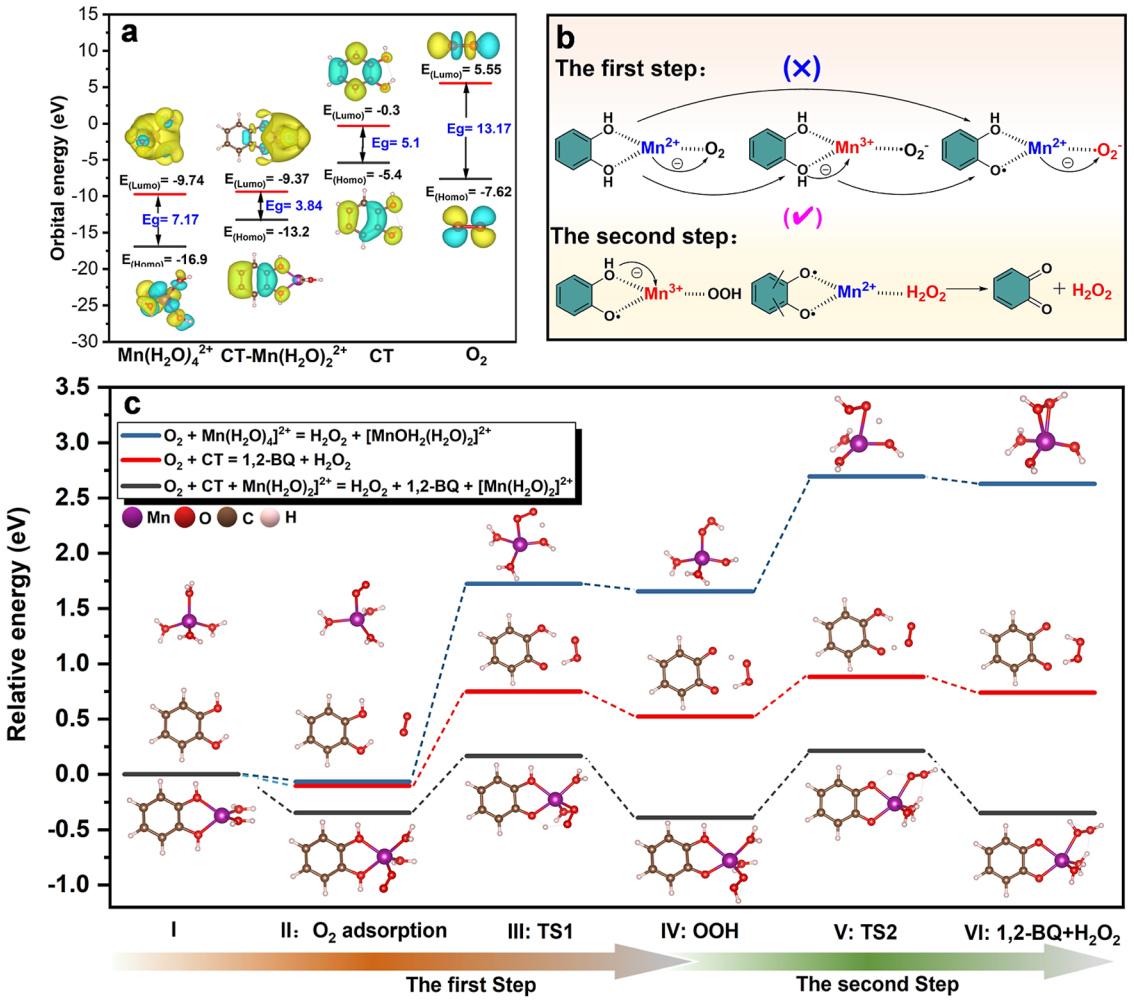


Figure 4. Mechanistic investigation of Mn^{2+} driven catalytic oxidation. (a) Frontier orbital energies of $[Mn(H_2O)_4]^{2+}$ (Mn^{2+}), $[Mn(H_2O)_4]^{2+}$-Catechol (Mn(II)-CT), catechol (CT), and molecular oxygen (O_2). (b) Proposed two-step electron transfer mechanism for catalytic oxidation. (c) DFT transition state calculations of the relative energies along the reaction pathways for Mn^{2+}, CT, and Mn(II)−CT during catalytic reduction of O_2 to H_2O_2 and CT oxidation to *ortho*-benzoquinone (1,2-BQ).

1660 cm^{-1} (Figure S22). The deconvoluted bands at approximately 1589, 1612, and 1635 cm^{-1} could be assigned to aromatic C=C skeletal vibrations, while the band at 1660 cm^{-1} could reflect conjugated C=O groups.[69,70] The simultaneous emergence of aryl ether and aromatic C=C bands is consistent with semiquinone radical coupling and oxidative polymerization processes involving single-electron transfer reactions, whereas the conjugated C=O band may reflect the formation of quinone-like products through further oxidation of CT-derived semiquinone intermediates (Figure 3f).

Mn^{2+} paramagnetic signal variations were monitored using in situ EPR spectroscopy. Hydrated Mn^{2+} ions exhibit a 6-line hyperfine splitting signal near g = 2.005, attributable to the high-spin d^5 center (Figure 3g,h).[71] This signal remains stable in the absence of CGG but declines markedly upon CGG addition in the presence of O_2 (Figure 3g−i), indicating changes in the Mn-centered d-electron spin environment during the reaction. Such attenuation may reflect redistribution of Mn-centered spin/electron density associated with changes in the local coordination environment and oxidation-related changes in the Mn-centered electronic state. DFT calculations quantify Mn-centered atomic spin population as 4.92 μ_B (Mn^{2+}), 4.91 μ_B (Mn(II)−CT), and 4.68 μ_B (CT−Mn(II)−O_2) (Figure S23). The pronounced 0.23 μ_B decrease upon O_2 coordination (Δ = 4.91 → 4.68 μ_B) suggests a partial charge transfer from the Mn(II) center to the O_2 moiety, consistent with incipient oxidation of the Mn^{2+}. Importantly, no Mn(III/IV) oxides are detected in the final product (Figure 1n), indicating no detectable accumulation of solid higher-valent Mn. The attenuation of the Mn^{2+} EPR signal may reflect the transient involvement of soluble Mn(III)-like species, whose d^4 electronic configuration with an integer-spin ground state could result in diminished hyperfine splitting.[72,73] Previous work also proposed that Mn(II) drives catechol oxidative ring-opening under aerobic conditions, involving Mn(II)/Mn(III) cycling.[33] To further probe the possible involvement of Mn(III) intermediates, pyrophosphate, a common Mn(III) complexing agent, was added to the reaction system (Figure S24). UV spectroscopy reveals a significant absorption peak at 258 nm (Figure S24a), which develops during the reaction of Mn^{2+} with CGG, corresponding to the characteristic feature of the Mn(III)-PP complex.[74] By contrast, no comparable sharp absorption peak at 258 nm is observed in the control experiments without PP or CGG, or when the Mn^{2+}−CGG reaction is conducted in the presence of PP under anoxic

Downloaded from pubs.acs.org/esthag/article-pdf/60/44/31669/6899314/acs.est.6c12201.pdf by UNIV GRENOBLE ALPES user on 10 November 2026

https://doi.org/10.1021/acs.est.6c12201
Environ. Sci. Technol. 2026, 60, 31669−31684

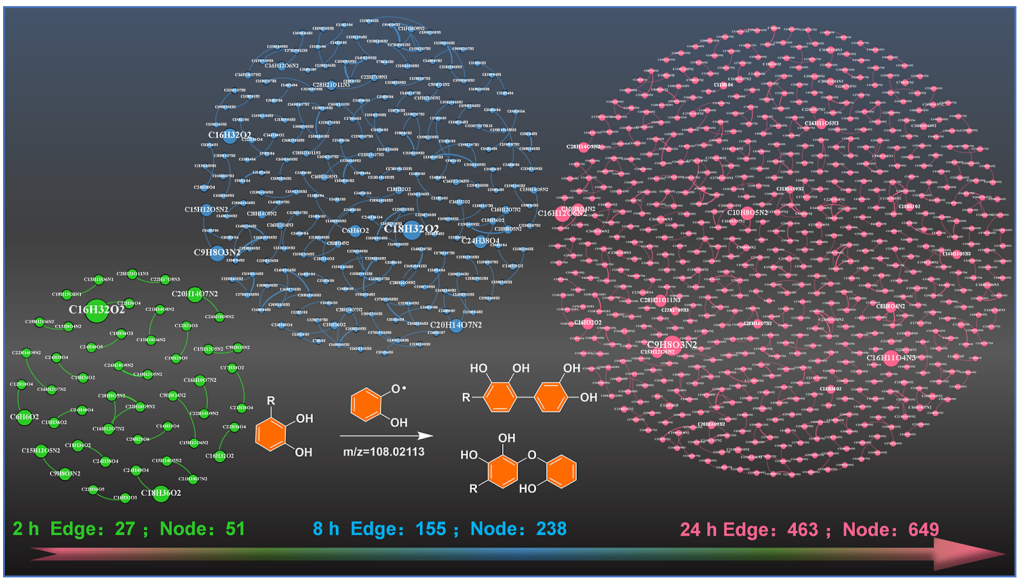


Figure 5. Molecular network analysis associated with semiquinone radical coupling. Chemical transformation network diagram showing molecular formula relationships consistent with the proposed coupling of semiquinone-derived units at 2, 8, and 24 h. Each node (circle) represents the molecular formula, with node size reflecting the relative intensity of each molecule. The edges (chemical transformations) connecting the nodes are defined by the mass difference ($n \times 108.02113$) between the corresponding m/z values.

conditions (Figure S24b−d). To further evaluate whether PP itself could induce a similar absorption feature from soluble organic chromophores, >99% of dissolved Mn was removed by cation-exchange resin before PP addition. In the Mn-depleted solution, the broad UV background persisted, but no comparable sharp absorption peak at 258 nm was generated upon subsequent PP addition (Figure S24e). This comparison indicates that this sharp spectral feature was primarily associated with Mn-containing species rather than an artifact of PP-induced absorption by soluble CGG-derived chromophores. Together, the in situ EPR results, DFT calculations, and PP-trapping experiments are consistent with the transient involvement of Mn(III)-like intermediates, although their direct quantification remains challenging because of their transient nature and the potential perturbation of reaction kinetics by the trapping agent.

Frontier molecular orbital analysis provides further insight into the electron-transfer process (Figure 4a). In redox reactions, electron transfer typically occurs from the HOMO (highest occupied molecular orbital) of the reductant to the LUMO (lowest unoccupied molecular orbital) of the oxidant, with a smaller energy gap favoring the transfer. Upon complexation with Mn^{2+}, the HOMO remains localized on CT but drops significantly from −5.4 eV to −13.2 eV, indicating a substantial reduction in its electron-donating ability. This suggests that the complex does not promote CT oxidation via direct HOMO elevation. Instead, the reaction likely proceeds via a stepwise pathway, in which CT−Mn^{2+} complexation promotes the oxidation of Mn^{2+} by O_2, followed by electron transfer from CT to the oxidized Mn intermediate, thereby initiating the reaction.

Based on the above results, a catalytic oxidation pathway is proposed (Figure 4b), involving two sequential single-electron transfers that reduce O_2 to H_2O_2. In the first step, the Mn^{2+} metal center forms a ternary complex with CT and O_2. Coordination of CT to Mn^{2+} may further facilitate Mn^{2+}-to-O_2 electron transfer.[75] Similar to oxygen-activating metalloenzymes, O_2 is proposed to bind to the reduced metal to yield an oxidized metal-superoxide complex (Mn(III)-$^{\bullet}O_2^-$).[76,77] This intermediate is short-lived, as CT rapidly donates an electron to the Mn(III) center, regenerating Mn^{2+} and forming a semiquinone radical.[76] In the second step, the resulting $^{\bullet}O_2^-$ could oxidize Mn^{2+} again to Mn^{3+}, which then accepts an electron from CT's hydroxyl group, regenerating Mn^{2+} and reducing $^{\bullet}O_2^-$ to H_2O_2.[33,78]

DFT transition-state calculations were further performed to provide a mechanistic rationale for the proposed catalytic oxidation pathway. Figure 4c presents the free energy profiles for reactions involving the two-step electron transfer of Mn^{2+}, CT, and Mn(II)-CT complexes, reducing molecular oxygen to produce H_2O_2 and *ortho*-benzoquinone (1,2-BQ). Reactions involving Mn^{2+} or CT alone with O_2 exhibit increased relative energies, indicating they are thermodynamically unfavored. In contrast, the Mn(II)-CT complex exhibits a favorable energy decrease upon reaction with O_2, supporting the thermodynamic plausibility of the pathway proposed in Figure 4b. Importantly, CT complexation reduces the relative energy associated with the adsorption of molecular oxygen at the Mn^{2+} center (Figure 4c, Step II), suggesting that CT coordination may facilitate O_2 activation and subsequent Mn oxidation (Figure 4c, Steps II−IV). Throughout this process, Mn^{2+} acts essentially as an electron shuttle, facilitating the electron transfers between CT and O_2. During these electron transfers, the formed organic radicals (e.g., semiquinone radicals) and active quinonoid derivatives may undergo nucleophilic attack by similar radicals or nucleophiles (e.g., amino sugars, amino acids), leading to polymerization into structurally diverse products.[79−82]

3.4. Semiquinone Radical-Mediated Molecular Coupling and Functional Group Dynamics in Mn(II)-Catalyzed Humification

Semiquinone radical-mediated coupling reactions were visualized by constructing molecular networks based on FT-ICR MS data, in which CT-derived semiquinone radicals were introduced as transformations (edges) and chemical formulas

Downloaded from pubs.acs.org/esthag/article-pdf/60/44/31669/6899314/acs.est.6c12201.pdf by UNIV GRENOBLE ALPES user on 10 November 2026

https://doi.org/10.1021/acs.est.6c12201
Environ. Sci. Technol. 2026, 60, 31669−31684

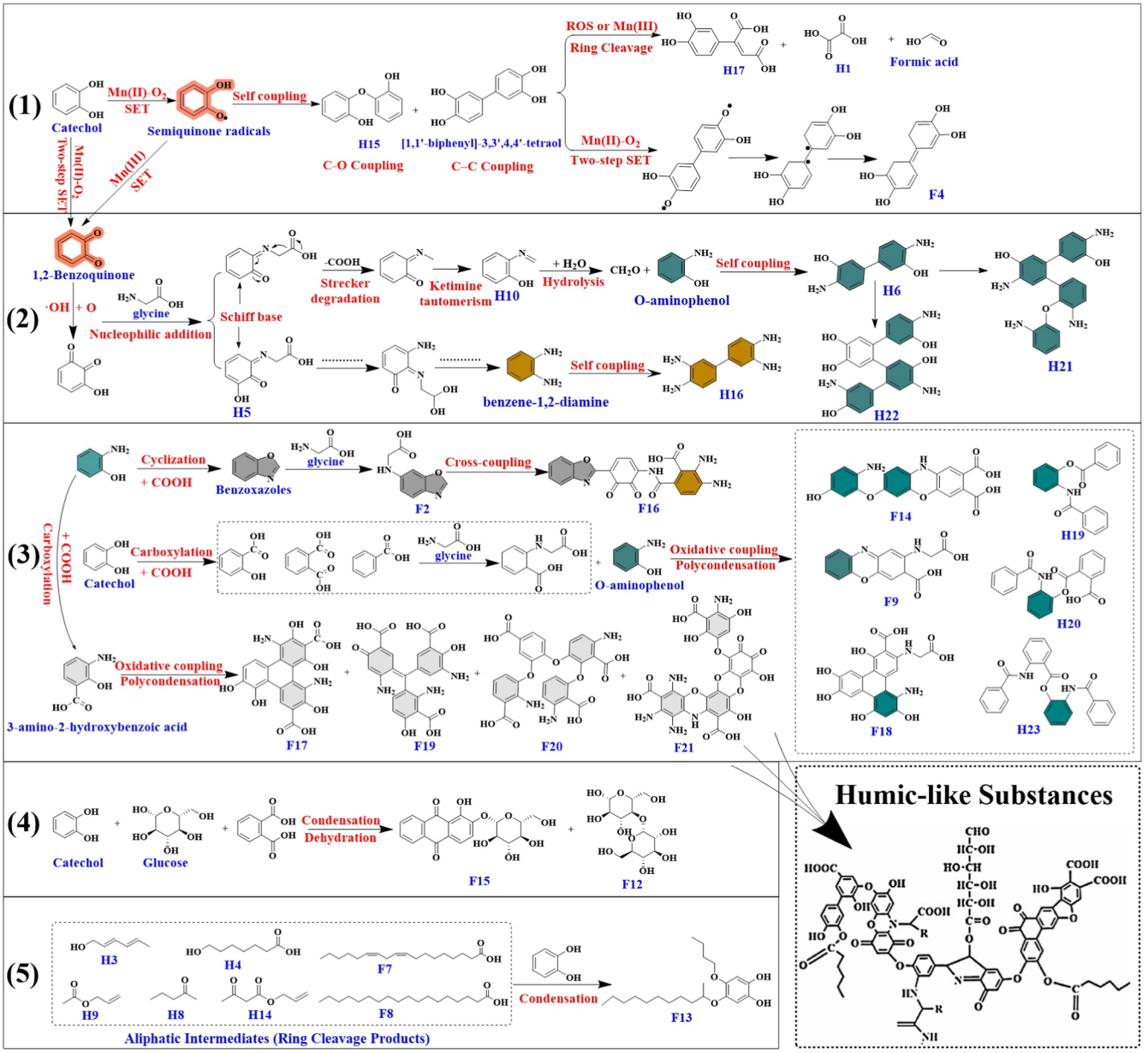


Figure 6. Proposed reaction scheme for Mn^{2+}-mediated humification. Specific structures and pathways represent tentative interpretations of the molecular-formula data.

as nodes (Figure 5). Molecular formulas differing by integer multiples of $C_6H_4O_2$ (108.02113 Da) were connected in the networks to illustrate formula-level relationships potentially associated with semiquinone radical coupling. After 2, 8, and 24 h of reaction, the networks contain 51, 238, and 649 nodes and 27, 155, and 463 edges, respectively. The proportion of network nodes relative to the total number of detected molecular formulas thus increases from 16.7% at 2 h to 28.7% at 8 h and 46.7% at 24 h. Within these networks, the numbers of nitrogen-containing nodes increase from 27 to 166 and 603, with their proportions rising from 52.9% to 69.7% and 92.9%, respectively. Together with the increase in molecular mass and compositional diversity (Figure 2a–c), this network expansion is consistent with the coupling process involving CT-derived semiquinone radicals during humification.

Functional-group dynamics underlying humification were examined using Kendrick mass defect (KMD) analysis, with particular focus on carboxyl (COO), hydroxyl (O), and amino (NH) moieties—key mediators of cross-linking, nitrogen incorporation, and redox reactivity during polymerization.[79−82] All molecules within a homologous series (differing only in the number of COO, O, and NH groups) share the same KMD value and appear on the same horizontal line in the Kendrick plot (Figure S25). The increasing number of molecules with identical KMD(COO), KMD(O), and KMD(NH) values, along with a redshift toward formulas containing more C, O, and N atoms, demonstrates time-dependent enrichment of these functional groups, consistent with ongoing polymer growth and increasing structural complexity.

To further elucidate the molecular transformation mechanisms, the reaction products were analyzed using Q-Orbitrap-HRMS in both ion modes (Figure S26) as a complement to FT-ICR MS. Major ion signals and the corresponding tentative structural assignments inferred from the molecular formulas

https://doi.org/10.1021/acs.est.6c12201
Environ. Sci. Technol. 2026, 60, 31669−31684

Downloaded from pubs.acs.org/esthag/article-pdf/60/44/31669/6899314/acs.est.6c12201.pdf by UNIV GRENOBLE ALPES user on 10 November 2026

obtained by FT-ICR MS and Q-Orbitrap-HRMS are summarized in Tables S5 and S6. Based on these structures and preceding analyses, plausible humification pathways are proposed (Figure 6). (1) Mn^{2+}-catalyzed oxidation of CT is proposed to proceed via single-electron transfer (SET), generating semiquinone radicals. These radicals may undergo C−C or C−O self-coupling to form dimers and oligomers.[83,84] Subsequent oxidation by ROS or transient Mn(III) could promote ring cleavage and organic acid formation. (2) Amino acids may react with quinones generated through Mn^{2+}-driven two-step single-electron transfer, thereby contributing to the formation of nitrogen-containing polymers.[13] In this proposed pathway, the amino group of glycine may undergo nucleophilic addition to the quinone C═O group, forming a Schiff base (imine).[85] Subsequently, quinones could induce Strecker degradation of amino acids.[86,87] O-aminophenol is proposed to form through ketimine tautomerism and hydrolysis of the resulting rearrangement product.[45,88] Further reaction of both C═O groups on the benzene ring with glycine could lead to benzene-1,2-diamine. Through oxidative coupling, *o*-aminophenol and benzene-1,2-diamine may serve as key intermediates contributing to the formation of aromatic polymers containing nitrogenous heterocycles and amide structures.[85] (3) Benzoxazole-like structures may form via cyclization reactions involving *o*-aminophenol and carboxylic acids or aldehydes, and may subsequently become incorporated into higher-molecular-weight products such as the tentatively assigned F2 and F16 species (Figure 6; Table S5).[89] In addition, aromatic acids like benzoic acid and 3-amino-2-hydroxybenzoic acid may arise from carboxylation or related substitution reactions of catechol- and *o*-aminophenol-derived structures. These compounds could serve as structural motifs that further contribute to the formation of larger molecular assemblies. (4) Glucose may condense with phenols and aromatic acids to form glycosides (F15) or undergo direct dehydration to produce disaccharides (F12). Glucose and glycine may also undergo a Maillard reaction to form condensation polymers.[16,90] Yet the specific condensation product is not directly identified among the dominant mass spectral species, potentially reflecting further transformation of initially formed condensation products. (5) Ring cleavage of self-coupling products and other aromatic structures may generate long-chain aliphatic species, which may be further catalyzed to reintegrate into aromatic ring structures. Ultimately, the products generated through these proposed pathways may associate to form supramolecular assemblies through hydrogen bonding, van der Waals forces, $\pi-\pi$ interactions, and Mn^{2+} bridging interactions. Although cation-mediated bridging alone does not appear sufficient to initiate polymerization, Mn^{2+}-mediated bridging may contribute secondarily to the later−stage association, aggregation, or stabilization of products generated through oxidative polymerization. Overall, the combined experimental observations are consistent with a central role of Mn^{2+}-driven radical and quinone chemistry in the polymerization process. Amino, carboxyl, and hydroxyl groups likely serve as important reactive functionalities contributing to the generation of diverse aromatic derivatives, while *o*-aminophenol is proposed as a potentially important intermediate or structural motif in several polymeric products.

3.5. Environmental Implications

In soil biogeochemistry, attention is largely focused on the role of high-valent Mn(III/IV) in the oxidative transformation of organic matter, whereas Mn(II) is generally regarded as redox-inert.[11−13,18] Contrary to this paradigm, our study reveals an overlooked abiotic pathway in which soluble Mn^{2+}, through synergistic interactions with molecular oxygen, drives oxidative polymerization and the formation of nitrogen-enriched humic-like substances in a model system comprising the common soil precursors catechol, glycine, and glucose. This finding suggests that reduced Mn pools, commonly regarded as intermediates or end products of Mn redox cycling, may also participate in the abiotic transformation of organic matter under oxic or redox-fluctuating conditions. At equivalent Mn loadings, dissolved Mn^{2+} produces a greater cumulative yield of humic-like acids than the tested solid Mn(III/IV) phases or Mn(III) complexes under the experimental conditions. While this comparison reflects system-level humification performance rather than intrinsic catalytic activity, it suggests that the potential contribution of dissolved Mn^{2+} should be considered when evaluating Mn-mediated abiotic humification. Importantly, unlike relatively immobile solid-phase Mn(III/IV) oxides whose oxidative activity is largely restricted to mineral surfaces, dissolved Mn^{2+} may exhibit higher mobility within the soil matrix, potentially allowing it to access organic-rich microsites relevant to organic matter transformation.[17,18,91,92] Nevertheless, the quantitative contribution of this pathway to soil organic matter transformation and stabilization in natural environments remains unresolved, owing to potential constraints arising from redox heterogeneity, ligand competition, realistic Mn(II) availability, and the unresolved influence of product-associated Mn on downstream reactivity, apparent functionality, and long-term environmental behavior.

FT-ICR MS-based comparison of Mn^{2+}-catalyzed products with natural soil and freshwater DOM samples shows that detectable product molecular formulas shared with the environmental DOM molecular pool collectively account for 78% of the total relative abundance, indicating molecular-formula-level compositional similarity. While molecular formulas do not uniquely constrain specific structures and may encompass substantial isomeric diversity, the observed molecular-formula overlap suggests that Mn^{2+}-driven polymerization generates a subset of products with elemental compositions and molecular compositional characteristics comparable to those detected in natural organic matter. Notably, similar molecular features may also arise from reactions mediated by other manganese species and reactive phases (e.g., iron oxides, metal-rich clays, and enzymes), producing overlapping or distinct molecular features. Broader environmental sampling across gradients in Mn abundance, coexisting metal-ion composition, soil type, mineral assemblage, and extracellular enzymatic activity, together with the identification of shared and catalyst-specific molecular fingerprints, will therefore be necessary to disentangle these contributions and better constrain their roles in shaping natural organic matter.

In addition, Mn is recognized for its pivotal role in promoting organic matter decomposition and mineralization, particularly in forest litter layers where fungal exoenzymes oxidize Mn(II) to reactive Mn(III) species that degrade complex substrates such as lignin.[22−27,93] As litter decomposition proceeds, released Mn(II) may coexist with polyphenols, reducing sugars, amino acids, and other labile

Downloaded from pubs.acs.org/esthag/article-pdf/60/44/31669/6899314/acs.est.6c12201.pdf by UNIV GRENOBLE ALPES user on 10 November 2026

https://doi.org/10.1021/acs.est.6c12201
Environ. Sci. Technol. 2026, 60, 31669−31684

intermediates in organic-rich microsites, creating a plausible chemical setting for Mn(II)-mediated abiotic polymerization. Thus, Mn may play a dual role by facilitating both organic matter decomposition and abiotic polymerization, highlighting the need for a broader framework to evaluate how these processes jointly shape organic carbon transformation in Mn-rich environments. Given the abiotic focus of the present study, a more complete understanding of Mn-driven carbon transformation requires further integration of abiotic reactions with microbial processes in natural soils. At microhabitat scales, microbial degradation may supply and transform reactive intermediates that fuel Mn-mediated abiotic reactions, while Mn-driven redox-active species may, in turn, alter local chemical conditions and microbial activity. Resolving these coupled and competing biotic−abiotic interactions and clarifying their spatiotemporal coupling at microhabitat scales using litter-soil mesocosms and controlled comparative systems is important for assessing the contribution of Mn-driven abiotic humification to carbon stabilization in natural soils.

■ ASSOCIATED CONTENT

Supporting Information

The Supporting Information is available free of charge at https://pubs.acs.org/doi/10.1021/acs.est.6c12201.

Investigations into the effects of pH, Mn^{2+} concentration, phenolic compounds, and low-molecular-weight organic acids on humification processes, alongside quantitative analyses of FLA and HLA concentrations. Solid-phase HLA was characterized using EPR and ATR-FTIR, complemented by XRD analysis of the synthesized minerals. Reaction solutions were examined via EEM and UV−vis spectroscopy, with H_2O_2 concentrations determined quantitatively. Molecular-level compositional insights were obtained through FT-ICR MS and Q-Orbitrap HRMS, and further interpreted using Kendrick mass defect (KMD) analysis (PDF)

■ AUTHOR INFORMATION

Corresponding Authors

Wenfeng Tan − *Key Laboratory of Arable Land Conservation (Middle and Lower Reaches of Yangtze River), Ministry of Agriculture and Rural Affairs, College of Resources and Environment, Huazhong Agricultural University, Wuhan 430070, China; Hubei Key Laboratory of Soil Environment and Pollution Remediation, Wuhan 430070, China*; Email: tanwf@mail.hzau.edu.cn

Xionghan Feng − *Key Laboratory of Arable Land Conservation (Middle and Lower Reaches of Yangtze River), Ministry of Agriculture and Rural Affairs, College of Resources and Environment, Huazhong Agricultural University, Wuhan 430070, China; Hubei Key Laboratory of Soil Environment and Pollution Remediation, Wuhan 430070, China*; orcid.org/0000-0001-5499-7174; Phone: +86 27 87280271; Email: fxh73@mail.hzau.edu.cn; Fax: +86 27 87288618

Authors

Feng Jiang − *Key Laboratory of Arable Land Conservation (Middle and Lower Reaches of Yangtze River), Ministry of Agriculture and Rural Affairs, College of Resources and Environment, Huazhong Agricultural University, Wuhan 430070, China; Hubei Key Laboratory of Soil Environment and Pollution Remediation, Wuhan 430070, China*

Hong Su − *Key Laboratory of Arable Land Conservation (Middle and Lower Reaches of Yangtze River), Ministry of Agriculture and Rural Affairs, College of Resources and Environment, Huazhong Agricultural University, Wuhan 430070, China; Hubei Key Laboratory of Soil Environment and Pollution Remediation, Wuhan 430070, China*

Qing-long Fu − *School of Environmental Studies, China University of Geoscience, Wuhan 430074, China*; orcid.org/0000-0002-7125-6877

Bruno Lanson − *University Grenoble Alpes, CNRS, University Savoie Mont Blanc, IRD, University Gustave Eiffel, F-38000 Grenoble, France*; orcid.org/0000-0003-1187-3221

Xiaoming Wang − *Key Laboratory of Arable Land Conservation (Middle and Lower Reaches of Yangtze River), Ministry of Agriculture and Rural Affairs, College of Resources and Environment, Huazhong Agricultural University, Wuhan 430070, China; Hubei Key Laboratory of Soil Environment and Pollution Remediation, Wuhan 430070, China*; orcid.org/0000-0002-5484-3922

Hui Yin − *Key Laboratory of Arable Land Conservation (Middle and Lower Reaches of Yangtze River), Ministry of Agriculture and Rural Affairs, College of Resources and Environment, Huazhong Agricultural University, Wuhan 430070, China; Hubei Key Laboratory of Soil Environment and Pollution Remediation, Wuhan 430070, China*; orcid.org/0000-0003-3060-7025

Jingtao Hou − *Key Laboratory of Arable Land Conservation (Middle and Lower Reaches of Yangtze River), Ministry of Agriculture and Rural Affairs, College of Resources and Environment, Huazhong Agricultural University, Wuhan 430070, China; Hubei Key Laboratory of Soil Environment and Pollution Remediation, Wuhan 430070, China*

Caroline Peacock − *School of Earth and Environment, University of Leeds, Leeds LS2 9JT, U.K.*

Complete contact information is available at: https://pubs.acs.org/10.1021/acs.est.6c12201

Author Contributions

#Feng Jiang and Hong Su contributed equally to this work.

Notes

The authors declare no competing financial interest.

■ ACKNOWLEDGMENTS

This work is financially supported by the National Natural Science Foundation of China (Nos. 42377303, W2521004, and 42030709), and the Fundamental Research Funds for the Central Universities (2662025ZHPY005). We gratefully acknowledge A.E. and six anonymous reviewers for their thoughtful reviews and constructive comments.

■ REFERENCES

(1) Díaz-Martínez, P.; Maestre, F. T.; Moreno-Jiménez, E.; Delgado-Baquerizo, M.; Eldridge, D. J.; Saiz, H.; Gross, N.; Le Bagousse-Pinguet, Y.; Gozalo, B.; Ochoa, V.; et al. Vulnerability of mineral-associated soil organic carbon to climate across global drylands. *Nat. Clim. Change* **2024**, *14* (9), 976−982.

(2) Hashimoto, S.; Ito, A.; Nishina, K. Divergent data-driven estimates of global soil respiration. *Commun. Earth Environ.* **2023**, *4* (1), 460.

Downloaded from pubs.acs.org/esthag/article-pdf/60/44/31669/6899314/acs.est.6c12201.pdf by UNIV GRENOBLE ALPES user on 10 November 2026

(3) Kleber, M.; Bourg, I. C.; Coward, E. K.; Hansel, C. M.; Myneni, S. C. B.; Nunan, N. Dynamic interactions at the mineral−organic matter interface. *Nat. Rev. Earth Environ.* **2021**, *2*, 402−421.
(4) Wagai, R.; Mayer, L. M. Sorptive stabilization of organic matter in soils by hydrous iron oxides. *Geochim. Cosmochim. Acta* **2007**, *71* (1), 25−35.
(5) Kaiser, K.; Guggenberger, G. Mineral surfaces and soil organic matter. *Eur. J. Soil Sci.* **2003**, *54* (2), 219−236.
(6) Kleber, M.; Mikutta, R.; Torn, M. S.; Jahn, R. Poorly crystalline mineral phases protect organic matter in acid subsoil horizons. *Eur. J. Soil Sci.* **2005**, *56* (6), 717−725.
(7) Kaiser, K.; Eusterhues, K.; Rumpel, C.; Guggenberger, G.; Kögel-Knabner, I. Stabilization of organic matter by soil minerals investigations of density and particle-size fractions from two acid forest soils. *J. Plant Nutr. Soil Sci.* **2002**, *165* (4), 451−459.
(8) De Nobili, M.; Bravo, C.; Chen, Y. The spontaneous secondary synthesis of soil organic matter components: A critical examination of the soil continuum model theory. *Appl. Soil Ecol.* **2020**, *154*, 103655.
(9) Jokic, A.; Frenkel, A. I.; Vairavamurthy, M. A.; Huang, P. M. Birnessite catalysis of the Maillard reaction: Its significance in natural humification. *Geophys. Res. Lett.* **2001**, *28* (20), 3899−3902.
(10) Jokic, A.; Wang, M. C.; Liu, C.; Frenkel, A. I.; Huang, P. M. Integration of the polyphenol and Maillard reactions into a unified abiotic pathway for humification in nature: the role of δ-MnO_2. *Org. Geochem.* **2004**, *35* (6), 747−762.
(11) Shindo, H.; Huang, P. M. Role of Mn(IV) oxide in abiotic formation of humic substances in the environment. *Nature* **1982**, *298* (5872), 363−365.
(12) Xiao, K.-Q.; Zhao, Y.; Liang, C.; Zhao, M.; Moore, O. W.; Otero-Fariña, A.; Zhu, Y.-G.; Johnson, K.; Peacock, C. L. Introducing the soil mineral carbon pump. *Nat. Rev. Earth Environ.* **2023**, *4* (3), 135−136.
(13) Shindo, H.; Huang, P. M. Significance of Mn(IV) oxide in abiotic formation of organic nitrogen complexes in natural environments. *Nature* **1984**, *308* (5954), 57−58.
(14) Jokic, A.; Frenkel, A. I.; Huang, P. M. Effect of light on birnessite catalysis of the Maillard reaction and its implication in humification. *Can. J. Soil Sci.* **2001**, *81* (3), 277−283.
(15) Zhao, Y.; Jia, J.; Liu, C.; Feng, X. Carbon preservation in sedimentary deposits: Beyond mineral protection. *Innovation* **2024**, *5* (2), 100576.
(16) Moore, O. W.; Curti, L.; Woulds, C.; Bradley, J. A.; Babakhani, P.; Mills, B. J. W.; Homoky, W. B.; Xiao, K.-Q.; Bray, A. W.; Fisher, B. J.; Kazemian, M.; Kaulich, B.; Dale, A. W.; Peacock, C. L. Long-term organic carbon preservation enhanced by iron and manganese. *Nature* **2023**, *621* (7978), 312−317.
(17) Jones, M. E.; LaCroix, R. E.; Zeigler, J.; Ying, S. C.; Nico, P. S.; Keiluweit, M. Enzymes, manganese, or iron? Drivers of oxidative organic matter decomposition in sils. *Environ. Sci. Technol.* **2020**, *54* (21), 14114−14123.
(18) Li, H.; Santos, F.; Butler, K.; Herndon, E. A critical review on the multiple roles of manganese in stabilizing and destabilizing soil organic matter. *Environ. Sci. Technol.* **2021**, *55* (18), 12136−12152.
(19) Xue, X.; Hanna, K.; Abdelmoula, M.; Deng, N. Adsorption and oxidation of PCP on the surface of magnetite: Kinetic experiments and spectroscopic investigations. *Appl. Catal., B* **2009**, *89* (3−4), 432−440.
(20) Ding, Z.; Ding, Y.; Liu, F.; Yang, J.; Li, R.; Dang, Z.; Shi, Z. Coupled sorption and oxidation of soil dissolved organic matter on manganese oxides: Nano/Sub-nanoscale distribution and molecular transformation. *Environ. Sci. Technol.* **2022**, *56* (4), 2783−2793.
(21) Lan, S.; Ying, H.; Wang, X.; Liu, F.; Tan, W.; Huang, Q.; Zhang, J.; Feng, X. Efficient catalytic As(III) oxidation on the surface of ferrihydrite in the presence of aqueous Mn(II). *Water Res.* **2018**, *128*, 92−101.
(22) Berg, B.; Davey, M. P.; De Marco, A.; Emmett, B.; Faituri, M.; Hobbie, S. E.; Johansson, M.-B.; Liu, C.; McClaugherty, C.; Norell, L.; Rutigliano, F. A.; Vesterdal, L.; Virzo De Santo, A. Factors influencing limit values for pine needle litter decomposition: a synthesis for boreal and temperate pine forest systems. *Biogeochemistry* **2010**, *100* (1−3), 57−73.
(23) Keiluweit, M.; Nico, P.; Harmon, M. E.; Mao, J.; Pett-Ridge, J.; Kleber, M. Long-term litter decomposition controlled by manganese redox cycling. *Proc. Natl. Acad. Sci. U. S. A.* **2015**, *112* (38), E5253−E5260.
(24) Aponte, C.; García, L. V.; Marañón, T. Tree species effect on litter decomposition and nutrient release in mediterranean oak forests changes over time. *Ecosystems* **2012**, *15* (7), 1204−1218.
(25) Berg, B.; Steffen, K. T.; McClaugherty, C. Litter decomposition rate is dependent on litter Mn concentrations. *Biogeochemistry* **2007**, *82* (1), 29−39.
(26) Davey, M. P.; Berg, B.; Emmett, B. A.; Rowland, P. Decomposition of oak leaf litter is related to initial litter Mn concentrations. *Can. J. Bot.* **2007**, *85* (1), 16−24.
(27) Trum, F.; Titeux, H.; Cornelis, J.-T.; Delvaux, B. Effects of manganese addition on carbon release from forest floor horizons. *Can. J. For. Res.* **2011**, *41* (3), 643−648.
(28) Wei, S.; Li, Z.; Sun, Y.; Zhang, J.; Ge, Y.; Li, Z. A comprehensive review on biomass humification: Recent advances in pathways, challenges, new applications, and perspectives. *Renew. Sustain. Energy Rev.* **2022**, *170*, 112984.
(29) Jiang, F.; Su, H.; Fu, Q.-l.; Yang, Z.; Wang, X.; Yin, H.; Tan, W.; Lanson, B.; Feng, X. Manganese oxides drive divergent fates of litter-derived DOM via pH-regulated oxidative decomposition and polymerization. *Environ. Sci. Technol.* **2025**, *59* (47), 25251−25264.
(30) Dou, S.; Zhang, Y.; Shan, J.; Wu, M.; Ma, R.; Guan, S.; Jia, Z. Soil organic matter revisited: why humic substances still matter? *Pedosphere* **2026**, *36* (1), 6−11.
(31) Zhang, J.; McKenna, A. M.; Zhu, M. Macromolecular characterization of compound selectivity for oxidation and oxidative alterations of dissolved organic matter by manganese oxide. *Environ. Sci. Technol.* **2021**, *55* (11), 7741−7751.
(32) Remucal, C. K.; Ginder-Vogel, M. A critical review of the reactivity of manganese oxides with organic contaminants. *Environ. Sci.:Processes Impacts* **2014**, *16* (6), 1247−1266.
(33) Gao, Y.; Gimilaro, C.; Zhang, H. MnO_2 and oxygen facilitate organic matter formation via oxidation and catalysis in oxygenated alkaline conditions. *Environ. Sci. Technol.* **2025**, *59* (25), 12618−12629.
(34) Zou, J.; Huang, J.; Yue, D.; Zhang, H. Roles of oxygen and Mn(IV) oxide in abiotic formation of humic substances by oxidative polymerization of polyphenol and amino acid. *Chem. Eng. J.* **2020**, *393*, 124734.
(35) Zahoransky, T.; Kaiser, K.; Mikutta, C. High manganese redox variability and manganate predominance in temperate soil profiles as determined by X-ray absorption spectroscopy. *Geochim. Cosmochim. Acta* **2022**, *338*, 229−249.
(36) Zhang, Y.; Hobbie, S. E.; Schlesinger, W. H.; Berg, B.; Sun, T.; Zhu, J. Exchangeable manganese regulates carbon storage in the humus layer of the boreal forest. *Proc. Natl. Acad. Sci. U.S.A.* **2024**, *121* (13), No. e2318382121.
(37) Zhao, C.; Du, Y.; Wang, H.; Zhou, W.; Xun, F.; Liu, S.; Li, B.; Lu, X.; Wu, Q. L.; Xiao, K.-Q.; et al. Geopolymerization threatens the persistence of organic carbon associated with iron in anoxic environments. *Nat. Commun.* **2025**, *16* (1), 6717.
(38) McKenzie, R. M. The synthesis of birnessite, cryptomelane, and some other oxides and hydroxides of manganese. *Mineral. Mag.* **1971**, *38* (296), 493−502.
(39) Duckworth, O. W.; Sposito, G. Siderophore−manganese(III) interactions II. Manganite dissolution promoted by desferrioxamine B. *Environ. Sci. Technol.* **2005**, *39* (16), 6045−6051.
(40) Kostka, J. E.; Luther, G. W.; Nealson, K. H. Chemical and biological reduction of Mn(III)-pyrophosphate complexes: Potential importance of dissolved Mn(III) as an environmental oxidant. *Geochim. Cosmochim. Acta* **1995**, *59* (5), 885−894.
(41) Ward, C. P.; Cory, R. M. Complete and partial photo-oxidation of dissolved organic matter draining permafrost soils. *Environ. Sci. Technol.* **2016**, *50* (7), 3545−3553.

Downloaded from pubs.acs.org/esthag/article-pdf/60/44/31669/6899314/acs.est.6c12201.pdf by UNIV GRENOBLE ALPES user on 10 November 2026

(42) Wang, X.; Xiang, W.; Wang, S.; Ge, J.; Qu, R.; Wang, Z. Oxidative oligomerization of phenolic endocrine disrupting chemicals mediated by Mn(III)-L complexes and the role of phenoxyl radicals in the enhanced removal: Experimental and theoretical studies. *Environ. Sci. Technol.* **2020**, *54* (3), 1573−1582.
(43) Wang, C.; Ying, C.; Wang, W.; Zhou, S.; Wan, B.; Tan, W.; Feng, X. Sunlight-driven transformation of ferrihydrite via ligand-to-metal charge transfer: The critical factors and arsenic repartitioning. *Environ. Sci. Technol.* **2025**, *59* (13), 6567−6578.
(44) Zhang, Y.; Yue, D.; Ma, H. Darkening mechanism and kinetics of humification process in catechol-Maillard system. *Chemosphere* **2015**, *130*, 40−45.
(45) Zhang, X.; Zong, Y.; Xu, L.; Mao, Y.; Wu, D. Enhanced abiotic integrated polyphenol-Maillard humification by Mg/Fe layered double hydroxide (LDH): Role of Fe(III)-polyphenol complexation. *Chem. Eng. J.* **2021**, *425*, 130521.
(46) Gao, Z.; Liu, J.; Skurie, C.; Zhu, Y.; Jun, Y.-S. Photochemical reactions of dissolved organic matter and bromide ions facilitate abiotic formation of manganese oxide solids. *Water Res.* **2022**, *222*, 118831.
(47) Wu, P.; Fu, Q.-L.; Zhu, X.-D.; Liu, C.; Dang, F.; Müller, K.; Fujii, M.; Zhou, D.-M.; Wang, H.-L.; Wang, Y.-J. Contrasting impacts of pH on the abiotic transformation of hydrochar-derived dissolved organic matter mediated by δ-MnO_2. *Geoderma* **2020**, *378*, 114627.
(48) Chen, Y.; Jiang, C.; Wang, Y.; Song, R.; Tan, Y.; Yang, Y.; Zhang, Z. Sources, environmental fate, and ecological risks of antibiotics in sediments of Asia's longest river: A whole-basin investigation. *Environ. Sci. Technol.* **2022**, *56* (20), 14439−14451.
(49) Ganbat, B.; Tseden-Ish, B. Characteristics and properties of soil reaction (pH) of Mongolian forest. *Mongol. J. Geogr. Geoecol.* **2024**, *61* (45), 208−217.
(50) Dai, W.; Li, Y.; Fu, W.; Jiang, P.; Zhao, K.; Li, Y.; Penttinen, P. Spatial variability of soil nutrients in forest areas: A case study from subtropical China. *J. Plant Nutr. Soil Sci.* **2018**, *181* (6), 827−835.
(51) Poghosyan, L.; Lehtovirta-Morley, L. E. Investigating microbial and environmental drivers of nitrification in alkaline forest soil. *ISME Commun.* **2024**, *4* (1), ycae093.
(52) Zhang, Y.; Bi, Z.; Tian, W.; Ge, Z.; Xu, Y.; Xu, R.; Zhang, H.; Tang, S. Synergistic effect triggered by Fe_2O_3 and oxygen-induced hydroxyl radical enhances formation of amino-phenolic humic-like substance. *J. Environ. Manage.* **2023**, *348*, 119312.
(53) Zhang, Y.; Yue, D.; Fang, D.; Dong, X.; Li, W. Enhanced darkening effect from the interaction of MnO_2 and oxygen on the component evolution of amino-phenolic humic-like substances. *Chemosphere* **2021**, *263*, 127956.
(54) Zhang, Y.; Yue, D.; Wang, X.; Song, W. Mechanism of oxidation and catalysis of organic matter abiotic humification in the presence of MnO_2. *J. Environ. Sci.* **2019**, *77*, 167−173.
(55) Peng, H.; Yang, H.; Han, J.; Liu, X.; Su, D.; Yang, T.; Liu, S.; Pao, C.-W.; Hu, Z.; Zhang, Q.; Xu, Y.; Geng, H.; Huang, X. Defective $ZnIn_2S_4$ nanosheets for visible-light and sacrificial-agent-free H_2O_2 photosynthesis via O_2/H_2O redox. *J. Am. Chem. Soc.* **2023**, *145* (50), 27757−27766.
(56) Manceau, A.; Marcus, M. A.; Grangeon, S. Determination of Mn valence states in mixed-valent manganates by XANES spectroscopy. *Am. Mineral.* **2012**, *97* (5−6), 816−827.
(57) Fu, Q.-L.; Fujii, M.; Riedel, T. Development and comparison of formula assignment algorithms for ultrahigh-resolution mass spectra of natural organic matter. *Anal. Chim. Acta* **2020**, *1125*, 247−257.
(58) Zhou, Z.; Fu, Q.-L.; Fujii, M.; Waite, T. D. Complementary elucidation of the molecular characteristics of groundwater dissolved organic matter using ultrahigh-resolution mass spectrometry coupled with negative- and positive-ion electrospray ionization. *Environ. Sci. Technol.* **2023**, *57* (11), 4690−4700.
(59) Martell, A. E.; Smith, R. M. Critical Stability Constants. In *Other Organic Ligands*; Plenum Press: New York, 1977; Vol. 3.
(60) Morgan, J. J. Kinetics of reaction between O_2 and Mn(II) species in aqueous solutions. *Geochim. Cosmochim. Acta* **2005**, *69* (1), 35−48.
(61) Chatterjee, A.; Zhao, L.; Zhang, L.; Pradhan, D.; Zhou, X.; Leung, K. T. Core-level electronic structure of solid-phase glycine, glycyl-glycine, diglycyl-glycine, and polyglycine: X-ray photoemission analysis and Hartree−Fock calculations of their zwitterions. *J. Chem. Phys.* **2008**, *129* (10), 105104.
(62) Yu, Z.; Liu, X.; Chen, C.; Liao, H.; Chen, Z.; Zhou, S. Molecular insights into the transformation of dissolved organic matter during hyperthermophilic composting using ESI FT-ICR MS. *Bioresour. Technol.* **2019**, *292*, 122007.
(63) Song, J.; Li, M.; Jiang, B.; Wei, S.; Fan, X.; Peng, P. Molecular characterization of water-soluble humic-like substances in smoke particles emitted from combustion of biomass materials and coal using ultrahigh-resolution electrospray ionization Fourier transform ion cyclotron resonance mass spectrometry. *Environ. Sci. Technol.* **2018**, *52* (5), 2575−2585.
(64) Wang, C.; Chen, F.; Hu, C.; Ma, T.; Zhang, Y.; Huang, H. Efficient piezocatalytic H_2O_2 production of atomic-level thickness $Bi_4Ti_3O_{12}$ nanosheets with surface oxygen vacancy. *Chem. Eng. J.* **2022**, *431*, 133930.
(65) Sheriff, T. S. Production of hydrogen peroxide from dioxygen and hydroxylamine or hydrazine catalysed by manganese complexes. *J. Chem. Soc., Dalton Trans.* **1992**, No. 6, 1051−1058.
(66) Yu, C.; Zhang, Y.; Lu, Y.; Qian, A.; Zhang, P.; Cui, Y.; Yuan, S. Mechanistic insight into humic acid-enhanced hydroxyl radical production from Fe(II)-bearing clay mineral oxygenation. *Environ. Sci. Technol.* **2021**, *55* (19), 13366−13375.
(67) Zhong, C.; Cao, H.; Huang, Q.; Xie, Y.; Zhao, H. Degradation of sulfamethoxazole by manganese(IV) oxide in the presence of humic acid: Role of stabilized semiquinone radicals. *Environ. Sci. Technol.* **2023**, *57* (36), 13625−13634.
(68) Ulas, G.; Lemmin, T.; Wu, Y.; Gassner, G. T.; DeGrado, W. F. Designed metalloprotein stabilizes a semiquinone radical. *Nat. Chem.* **2016**, *8* (4), 354−359.
(69) Ibarra, J. V.; Muñoz, E.; Moliner, R. FTIR study of the evolution of coal structure during the coalification process. *Org. Geochem.* **1996**, *24* (6−7), 725−735.
(70) Hamciuc, C.; Lisa, G.; Hamciuc, E.; Epure, E.-L.; Tudorachi, N. Thermal behavior study and degradation mechanism by TG/MS/FTIR technique of some poly(aryl ether ether ketone)s. *J. Anal. Appl. Pyrolysis* **2020**, *150*, 104877.
(71) Gong, Y.; Shen, J.; Wu, Y.; Shen, L.; Zhao, S.; Zhou, Y.; Li, Y.; Cui, L.; Kang, J.; Chen, Z. Ligands-triggered evolution of catalytic intermediates during periodate activation via soluble Mn(II) for organic contaminants' abatement. *Appl. Catal. B Environ.* **2023**, *322*, 122093.
(72) Mu, Y.; Jiang, X.; Ai, Z.; Jia, F.; Zhang, L. Mn^{2+} promoted Cr(VI) reduction with oxalic acid: The Indispensable Role of In Situ Generated Mn^{3+}. *J. Hazard. Mater.* **2018**, *343*, 356−363.
(73) Maitra, U.; Naidu, B. S.; Govindaraj, A.; Rao, C. N. R. Importance of trivalency and the e_g^1 configuration in the photocatalytic oxidation of water by Mn and Co oxides. *Proc. Natl. Acad. Sci. U. S. A.* **2013**, *110* (29), 11704−11707.
(74) Qian, A.; Zhang, W.; Shi, C.; Pan, C.; Giammar, D. E.; Yuan, S.; Zhang, H.; Wang, Z. Geochemical stability of dissolved Mn(III) in the presence of pyrophosphate as a model ligand: Complexation and disproportionation. *Environ. Sci. Technol.* **2019**, *53* (10), 5768−5777.
(75) Luther, G. W. The frontier-molecular-orbital theory approach in geochemical processes. In *Aquatic Chemical Kinetics: Reaction Rates of Processes in Natural Waters*; Stumm, W., Ed.; John Wiley & Sons: New York, 1995; pp 173−198.
(76) Emerson, J. P.; Kovaleva, E. G.; Farquhar, E. R.; Lipscomb, J. D.; Que, L. Swapping metals in Fe- and Mn-dependent dioxygenases: evidence for oxygen activation without a change in metal redox state. *Proc. Natl. Acad. Sci. U. S. A.* **2008**, *105* (21), 7347−7352.
(77) Costas, M.; Mehn, M. P.; Jensen, M. P.; Que, L. Dioxygen activation at mononuclear nonheme iron active sites: enzymes, models, and intermediates. *Chem. Rev.* **2004**, *104* (2), 939−986.

Downloaded from pubs.acs.org/esthag/article-pdf/60/44/31669/6899314/acs.est.6c12201.pdf by UNIV GRENOBLE ALPES user on 10 November 2026

(78) Hansard, S. P.; Easter, H. D.; Voelker, B. M. Rapid reaction of nanomolar Mn(II) with superoxide radical in seawater and simulated freshwater. *Environ. Sci. Technol.* **2011**, *45* (7), 2811−2817.
(79) Waters, W. A. Comments on the mechanism of one-electron oxidation of phenols: a fresh interpretation of oxidative coupling reactions of plant phenols. *J. Chem. Soc. B* **1971**, 2026−2029.
(80) Sun, Z.; Wang, X.; Liu, C.; Fang, G.; Chu, L.; Gu, C.; Gao, J. Persistent free radicals from low-molecular-weight organic compounds enhance cross-coupling reactions and toxicity of anthracene on amorphous silica surfaces under light. *Environ. Sci. Technol.* **2021**, *55* (6), 3716−3726.
(81) Gao, X.; Yang, Z.; Zhang, W.; Pan, B. Carbon redirection via tunable Fenton-like reactions under nanoconfinement toward sustainable water treatment. *Nat. Commun.* **2024**, *15* (1), 2808.
(82) Wang, X.; Tian, L.; Li, Y.; Zhong, C.; Tian, C. Effects of exogenous cellulose-degrading bacteria on humus formation and bacterial community stability during composting. *Bioresour. Technol.* **2022**, *359*, 127458.
(83) Johnson, K.; Purvis, G.; Lopez-Capel, E.; Peacock, C.; Gray, N.; Wagner, T.; März, C.; Bowen, L.; Ojeda, J.; Finlay, N.; Robertson, S.; Worrall, F.; Greenwell, C. Towards a mechanistic understanding of carbon stabilization in manganese oxides. *Nat. Commun.* **2015**, *6* (1), 7628.
(84) Stone, A. T. Reductive dissolution of manganese(III/IV) oxides by substituted phenols. *Environ. Sci. Technol.* **1987**, *21* (10), 979−988.
(85) Gulkowska, A.; Krauss, M.; Rentsch, D.; Hollender, J. Reactions of a sulfonamide antimicrobial with model humic constituents: assessing pathways and stability of covalent bonding. *Environ. Sci. Technol.* **2012**, *46* (4), 2102−2111.
(86) Bittner, S. When quinones meet amino acids: chemical, physical, and biological consequences. *Amino Acids* **2006**, *30* (3), 205−224.
(87) Rizzi, G. P. Formation of Strecker aldehydes from polyphenol-derived quinones and α-amino acids in a nonenzymic model system. *J. Agric. Food Chem.* **2006**, *54* (5), 1893−1897.
(88) Delgado, R. M.; Zamora, R.; Hidalgo, F. J. Contribution of phenolic compounds to food flavors: Strecker-type degradation of amines and amino acids produced by o- and p-diphenols. *J. Agric. Food Chem.* **2015**, *63* (1), 312−318.
(89) Gao, S.; Gao, L.; Meng, H.; Luo, M.; Zeng, X. Iron-catalyzed synthesis of benzoxazoles by oxidative coupling/cyclization of phenol derivatives with benzoyl aldehyde oximes. *Chem. Commun.* **2017**, *53* (71), 9886−9889.
(90) Wang, H.-Y.; Qian, H.; Yao, W.-R. Melanoidins produced by the Maillard reaction: structure and biological activity. *Food Chem.* **2011**, *128* (3), 573−584.
(91) Jones, M. E.; Nico, P. S.; Ying, S.; Regier, T.; Thieme, J.; Keiluweit, M. Manganese-driven carbon oxidation at oxic−anoxic interfaces. *Environ. Sci. Technol.* **2018**, *52* (21), 12349−12357.
(92) Lacroix, E. M.; Aeppli, M.; Boye, K.; Brodie, E.; Fendorf, S.; Keiluweit, M.; Naughton, H. R.; Noël, V.; Sihi, D. Consider the anoxic microsite: acknowledging and appreciating spatiotemporal redox heterogeneity in soils and sediments. *ACS Earth Space Chem.* **2023**, *7* (9), 1592−1609.
(93) Hofrichter, M. Review: lignin conversion by manganese peroxidase (MnP). *Enzyme Microb. Technol.* **2002**, *30* (4), 454−466.

Downloaded from pubs.acs.org/esthag/article-pdf/60/44/31669/6899314/acs.est.6c12201.pdf by UNIV GRENOBLE ALPES user on 10 November 2026

https://doi.org/10.1021/acs.est.6c12201
Environ. Sci. Technol. 2026, 60, 31669−31684

Supporting Information for

Mn(II)-Mediated Abiotic Humification via Synergistic Interactions with Molecular Oxygen

Feng Jiang[1,2†], Hong Su[1,2†], Qing-long Fu[3], Bruno Lanson[4], Xiaoming Wang[1,2], Hui Yin[1,2], Jingtao Hou[1,2], Wenfeng Tan[1,2]*, Xionghan Feng[1,2]*, Caroline Peacock[5]

[1]Key Laboratory of Arable Land Conservation (Middle and Lower Reaches of Yangtze River), Ministry of Agriculture and Rural Affairs, College of Resources and Environment, Huazhong Agricultural University, Wuhan 430070, China

[2]Hubei Key Laboratory of Soil Environment and Pollution Remediation, Wuhan 430070, China

[3]School of Environmental Studies, China University of Geoscience, Wuhan 430074, China

[4]University Grenoble Alpes, CNRS, University Savoie Mont Blanc, IRD, University Gustave Eiffel, ISTerre, F-38000 Grenoble, France

[5]School of Earth and Environment, University of Leeds, Leeds LS2 9JT, United Kingdom

*Corresponding author: Xionghan Feng, Tel: +86 27 87280271; fax: +86 27 87288618; E-mail: fxh73@mail.hzau.edu.cn; tanwf@mail.hzau.edu.cn

Downloaded from pubs.acs.org/esthag/article-supplement/5459299/pdf/es6c12201_si_001/ by guest on 10 November 2026

1 **Table of Contents:**

2 Text S1 - Text S10: Page 2 - 23

3 Figure S1 - Figure S26: Page 24 - 49

4 Table S1- Table S7: Page 50 - 58

5 Reference: Page 58 - 68

6

Downloaded from pubs.acs.org/esthag/article-supplement/5459299/pdf/es6c12201_si_001/ by guest on 10 November 2026

Text S1: Chemical reagents

Catechol (CT) (99%, Sigma-Aldrich, U.S.A); Hydroquinone (Hyd) (99%, Sigma-Aldrich, U.S.A); Resorcinol (Re) (99%, Sigma-Aldrich, U.S.A); Phenol (Phe) (99%; Aladdin, China); Glucose (Glu) (99%, Sigma-Aldrich, U.S.A); Glycine (Gly) (99%, Sigma-Aldrich, U.S.A); Manganese chloride (II) tetrahydrate (Mn^{2+}) (99%, Sinopharm Chemical Reagent, China); Calcium chloride (Ca^{2+}) (99%, Sinopharm Chemical Reagent, China); Barium chloride (Ba^{2+}) (99%, Sinopharm Chemical Reagent, China); Magnesium chloride (Mg^{2+}) (99%, Sinopharm Chemical Reagent, China); Boric acid (99%, Sinopharm Chemical Reagent, China); Sodium tetraborate decahydrate (99%, Sinopharm Chemical Reagent, China); Sodium pyrophosphate decahydrate (PP) (99%, Sinopharm Chemical Reagent, China); Manganese(III) fluoride (98%, Alfa Aesar, China); 5,5-dimethyl-1-pyrroline-N-oxide (DMPO) (97%, DOJINDO, Japan); Methanol (LC-MS, Thermo Fisher Scientific, U.S.A); Hydrochloric acid (HCl) (AR, Chron Chemicals, China); Potassium permanganate ($KMnO_4$) (AR, Chron Chemicals, China);

Text S2: Preparation methods for δ-MnO_2, γ-MnOOH, and the Mn(III)-PP complex

δ-Mn(IV)O_2 (Birnessite) was synthesized using $KMnO_4$ and HCl, as previously reported (Mckenzie, 1971).[1] $KMnO_4$ (31.61 g) was mixed with 300 mL of deionized water, stirred at 450 rpm, and heated to a boil. HCl (35 mL, 12 M) was added to the $KMnO_4$ solution at a 0.7 mL min^{-1} rate and continued to react for 30 min after titration. The formed precipitates were washed with deionized water repeatedly until the conductivity dropped below 10 μS cm^{-1}. The product was then centrifuged and freeze-

Downloaded from pubs.acs.org/esthag/article-supplement/5459299/pdf/es6c12201_si_001/ by guest on 10 November 2026

dried. The dried powder was ground and passed through a 100-mesh sieve to obtain the final birnessite sample.

γ-Mn(III)OOH (Manganite) was synthesized following the procedure described by Duckworth and Sposito.[2] In brief, 250 mL of 0.4 mol L^{-1} NH_4OH and 250 mL of 1.4 mol L^{-1} $MnSO_4 \cdot H_2O$ were thoroughly mixed in a beaker. This mixture was then transferred to a triangular flask and stirred vigorously on a magnetic stirrer. A controlled addition of 90 mL of 30% H_2O_2 was made at a flow rate of approximately 2 mL min^{-1} into the aforementioned mixture. After the addition, the solution was refluxed for 24 h in an oil bath at 105 °C and subsequently allowed to cool naturally. The supernatant was decanted, and the precipitate was transferred into a 1 kDa dialysis bag and dialyzed until the conductivity was <10 μS cm^{-1}. The product was then dried in an oven at 40 °C, ground into a fine powder, and filtered through a 100-mesh sieve to obtain the manganite.

The preparation of Mn(III)-PP stock solution followed the procedures outlined by Kostka et al.[3] Manganese(III) fluoride was gradually added to a sodium pyrophosphate (PP) solution (pH=8) at a 1:20 molar ratio under vigorous stirring. The concentration and purity (> 99%) of the Mn(III)−PP stock solution were confirmed using inductively coupled Plasma Optical Emission Spectrometry (ICP-OES) for total Mn and iodometric titration for the oxidation state.[4]

Text S3: Extraction and purification of the humic-like acid (HLA) and fulvic-like acid (FLA) fraction

The extraction and purification of HLA were conducted following the method

Downloaded from pubs.acs.org/esthag/article-supplement/5459299/pdf/es6c12201_si_001/ by guest on 10 November 2026

recommended by the International Humic Substances Society.[5] (1) Initially, a 10 mL aliquot of both the reaction suspension and filtrate, after 96 h of incubation, was transferred to a 15 mL centrifuge tube and acidified to pH 1 using concentrated HCl. This mixture was allowed to stand at room temperature for 24 h to precipitate the HLAs. (2) Subsequent centrifugation at 10,000 rpm for 20 minutes facilitated the separation of the precipitate from the supernatant. (3) The HLA precipitate was then subjected to repeated washing with dilute HCl until the filtrate turned colorless. The purified precipitate was fully dissolved in 0.1 M NaOH. (4) Concurrently, the supernatant containing FLA was passed through a column containing 1 mL of XAD-8 resin to adsorb the FLA. The column underwent rinsing with approximately 30 mL of ultrapure water until the effluent was colorless, followed by desorption of FLA using 0.1 M NaOH. (5) The solutions containing HLAs and FLAs were adjusted to pH 7, and then their dissolved organic carbon (DOC) concentrations were quantified. The solid-phase HLA obtained after the wash step was freeze-dried for subsequent solid-phase characterization. It is noteworthy that HLA and FLA extracted from the filtrate represent the solution-phase fractions, whereas those extracted from the unfiltered suspension encompass the total HLA and FLA. The discrepancy between these measurements indicates the degree of HLA and FLA precipitation. In systems involving manganese oxides (δ-MnO_2 and γ-MnOOH), total humic-like substances were determined as the cumulative sum of HLA and FLA extracted from both the filtrate and the mineral surface. Specifically, a 10 mL aliquot of the reaction solution was centrifuged to separate the filtrate, and the HLA and FLA adsorbed on the mineral

Downloaded from pubs.acs.org/esthag/article-supplement/5459299/pdf/es6c12201_si_001/ by guest on 10 November 2026

surface were extracted by dissolving them in NaOH until the solution turned colorless. The volume was then adjusted to 10 mL using deionized water, and the previously outlined protocol steps (1)–(5) were repeated to ascertain the concentrations of HLA and FLA adsorbed on the mineral surface.

To assess the performance of the extraction protocol, recovery experiments were conducted using standard reference materials, Suwannee River fulvic acid (SRFA) and humic acid (SRHA). Both SRFA and SRHA were separately dissolved in 0.1 M NaOH and adjusted to a TOC concentration of 100 mg L^{-1}, followed by extraction using the same procedure as applied in this study. Triplicate extractions yielded consistent recoveries, with HA recoveries of 93.4 ± 0.5% and FA recoveries of 91.9 ± 1.6%. These results indicate that the method performs consistently for standard humic substances under the applied conditions. In addition, to examine the extractability of organic carbon bound to mineral surfaces, the surface-associated organic carbon after reaction was desorbed using 0.1 M NaOH. The carbon contents before and after extraction were quantified by elemental analysis to estimate the corresponding extraction efficiency. For the birnessite–CGG system, the carbon content decreased from 6.31 ± 0.82 wt% to 0.55 ± 0.07 wt% after extraction, corresponding to an extraction efficiency of 91.35 ± 0.73%. Similarly, for the manganite–CGG system, the carbon content decreased from 1.97 ± 0.04 wt% to 0.15 ± 0.04 wt%, yielding an extraction efficiency of 92.21 ± 1.83%.

Text S4: Detailed physicochemical characterization and computational methodology

(1) UV-vis analysis

Downloaded from pubs.acs.org/esthag/article-supplement/5459299/pdf/es6c12201_si_001/ by guest on 10 November 2026

UV-visible spectrophotometer (UV-vis, Agilent Technologies Cary 8454) was used to record the UV–visible absorbance of the reaction filtrate, which was diluted ten-fold, across the wavelength range of 200 to 800 nm with a 1 nm sampling interval. The absorbance at 400 nm (A_{400}) was recorded to monitor the changes in organic chromophores and the formation of browning substances during humification.[6, 7, 8] The absorbance of filtrate at 600 nm (A_{600}) was measured, and the extinction coefficient (E_{600}) was calculated using the following equation to evaluate the formation of dark-colored products during the humification process.[8, 9, 10, 11]

$$E_{600} = \frac{A_{600}}{DOC(g/L) \times L(cm) \times 1000}$$

where A_{600} represents the absorbance at 600 nm, DOC is the dissolved organic carbon concentration (g L^{-1}), and L (1 cm) is the light path length. A_{400} and A_{600} are dimensionless, whereas E_{600} is expressed in L g^{-1} cm^{-1}.

(2) AAS analysis

The Mn concentration in the solution was measured using atomic absorption spectrometry (AAS, Agilent Technologies 200 series). The Mn standard was prepared by dilution of a 1000 mg L^{-1} standard.

(3) DOC and TN determination

Dissolved organic carbon (DOC) and total nitrogen (TN) in the reaction filtrate were analyzed using a multi-N/C 2100 analyzer (Analytik Jena, Germany).

(4) HPLC analysis

Catechol concentration was quantified by high-performance liquid chromatography (HPLC, Agilent Technologies 1260 Infinity) equipped with an SB-

Downloaded from pubs.acs.org/esthag/article-supplement/5459299/pdf/es6c12201_si_001/ by guest on 10 November 2026

C18 column (5 μm, 4.6×150 mm) maintained at 35 ℃. The mobile phase comprised acetonitrile and water (50:50, v/v) at a flow rate of 0.8 mL min^{-1}, with an injection volume of 10 μL. The UV detector was set to 280 nm.

(5) EEM spectroscopy analysis

Excitation-emission matrix (EEM) fluorescence spectra were recorded using a fluorescence spectrophotometer (F-7100, Hitachi Co., Japan) at room temperature with excitation wavelengths of 250-500 nm, and emission wavelengths of 280 to 550 nm. The scan mode was set to 5 nm excitation/emission slits, a scanning speed of 2400 nm min^{-1}, and a PMT voltage of 600 V. To minimize inner-filter effects, the filtrate used for fluorescence measurements was diluted to ensure the DOC concentration was below 7.2 mg L^{-1}. The humification index (HIX) was calculated using the peak area under the emission spectra 435–480 nm divided by 300–345 nm at constant excitation of 254 nm.[12]

(6) Gas Products Analysis

CO_2 production was quantified to evaluate potential mineralization during the reaction. Independent sealed-bottle experiments were conducted under the same reaction conditions as the main Mn(II)–CGG system. Before reaction initiation, the headspace was purged with CO_2-free air to establish an oxic atmosphere while minimizing background CO_2. Parallel bottles purged with N_2 were used as anoxic controls. At selected reaction times, 25 mL of headspace gas was withdrawn from each bottle and analyzed for CO_2 using a gas chromatograph (Agilent 8890 GC, Germany) equipped with a thermal conductivity detector. After each sampling, the bottles were

Downloaded from pubs.acs.org/esthag/article-supplement/5459299/pdf/es6c12201_si_001/ by guest on 10 November 2026

re-purged with CO_2-free air or N_2 to remove residual headspace CO_2 and restore the designated atmosphere. Cumulative CO_2-C production was calculated by summing the amount of CO_2-C accumulated during each sampling interval. The carbon mass released as CO_2 at each sampling time was calculated according to:

$$m_{CO_2\text{-}C,i} = \frac{C_i \times V_h \times 12}{24450}$$

where $m_{CO_2\text{-}C,i}$ is the carbon mass accumulated as headspace CO_2 during sampling interval (μg C), C_i is the measured headspace CO_2 concentration at the end of sampling interval (*i*) (ppmv), V_h is the total headspace volume of the sealed bottle (mL), 12 is the molar mass of carbon (g mol^{-1}), and 24450 is the molar volume of an ideal gas at 25 °C and 1 atm (mL mol^{-1}).

(7) Determination of hydrogen peroxide

The concentration of hydrogen peroxide (H_2O_2) was determined following previously reported methods.[13] A 500 μL aliquot of the tenfold-diluted reaction solution was mixed with 2 mL of potassium iodide (KI) (0.1 M) and 50 μL of ammonium molybdate ($H_{32}Mo_7N_6O_{28}$) (0.01 M), followed by a 10-minute reaction. The absorbance at 352 nm was then recorded. To account for background interference, a control was prepared by mixing 500 μL of the reaction solution with 2.05 mL of deionized water. The absorbance of this background solution was subtracted from the sample absorbance using differential spectroscopy to obtain the H_2O_2 concentration.

(8) EPR measurement

All electron spin resonance (EPR) measurements were performed using a Magnettech ESR5000 spectrometer (Bruker, Germany). reactive oxygen species (ROS)

Downloaded from pubs.acs.org/esthag/article-supplement/5459299/pdf/es6c12201_si_001/ by guest on 10 November 2026

were detected using 5,5-dimethyl-1-pyrroline-N-oxide (DMPO) as the spin-trapping agent. A 400 μL aliquot of the reaction mixture was combined with 1 mL of 0.12 M DMPO (dissolved in methanol to capture superoxide ($\cdot O_2^-$) radicals and in water to capture hydroxyl (·OH) radicals), then vortexed for 1 minute prior to EPR analysis.

For the characterization of HLA solid particles, a precise mass of HLA was weighed and analyzed using the following EPR parameters: modulation frequency of 100 kHz, modulation amplitude of 0.2 mT, microwave power of 10 mW, sweep time of 100 seconds, and a magnetic field range of 3130 to 3630 G. The same EPR parameters were utilized for both HLA and ROS and measurements.

For the *in situ* determination of Mn^{2+} spin signals intensity in reaction solutions, a kinetic series was conducted using the EPR spectrometer with parameters set as modulation frequency of 100 kHz, modulation amplitude of 0.2 mT, microwave power of 1 mW, sweep time of 30 seconds, the kinetic sampling time of 150 seconds, 41 kinetic samples, and a magnetic field range of 3000 to 3700 G. The Mn^{2+} signal intensity changes were determined by averaging the maximum intensities of six spin signal peaks.

Semiquinone radical trapping experiments were conducted during the Mn^{2+}–CGG reaction by adding 400 μM $ZnCl_2$ as a trapping agent.[14, 15] The resulting mixtures were directly analyzed using the same EPR parameters applied for HLA and ROS measurements described above."

(9) XRD analysis

The powder X-ray diffraction (XRD) patterns of the reaction deposit were

Downloaded from pubs.acs.org/esthag/article-supplement/5459299/pdf/es6c12201_si_001/ by guest on 10 November 2026

acquired using a Rigaku D/max-1200 diffractometer with CuKα radiation (λ = 1.54 Å, 40 kV, 40 mA). Data were collected over a 2 θ range of 5−85° at a scan speed of 10° min^{-1} to characterize the crystal phases and structures.

(10) TEM visual inspection

The high-resolution transmission electron microscopy (HRTEM, Talos F200X, Thermo Scientific, USA) was equipped with an energy dispersive spectrometer (EDS) to identify morphology, particle size, and element distribution.

(11) ATR-FTIR spectroscopy

Attenuated total reflectance-Fourier transform infrared spectroscopy (ATR-FTIR, Bruker Optics Inc., Ettlingen, Germany) was employed to investigate the surface functional groups of the HLA. An average of 128 scans was recorded at a resolution of 4 cm^{-1} over the spectral range of 400−4000 cm^{-1} for each measurement. Two-dimensional correlation spectroscopy (2D-COS) analysis of the FTIR spectra was conducted using varying concentrations of Mn^{2+} as external perturbations. A detailed description of the theory can be found in the literature.[16] All COS computations and graphical analyses were performed using the "2D Shige" software.

In situ ATR-FTIR spectroscopy was performed using a ZnSe crystal.[17] Specifically, functional group structure information of organic matter passing over the surface of the ZnSe crystal can be acquired in infrared spectroscopy. We utilized a peristaltic pump to allow the reaction solution to flow through the ZnSe crystal at a rate of 0.5 mL min^{-1}. The sample spectrum was continuously recorded at 4 cm^{-1} resolution in the spectral range of 900−1700 cm^{-1} for 2 h. Data processing, including smoothing and baseline

Downloaded from pubs.acs.org/esthag/article-supplement/5459299/pdf/es6c12201_si_001/ by guest on 10 November 2026

206 correction, was carried out using Omnic software.

207 **(12) XANES analysis**

208 The Mn X-ray absorption near-edge structure (XANES) spectroscopy data were
209 obtained at room temperature on the 1W1B beamline at the Beijing Synchrotron
210 Radiation Facility (BSRF) within the 6.4–7.0 keV range (Mn K-edge). Prior to data
211 collection, energy calibration was systematically conducted using a Mn metal foil. The
212 Mn K-edge spectra were averaged and background-subtracted with the following
213 parameters: E_0 = 6538 eV, Rbkg = 1 Å, and k-weight = 2. Fluorescence mode was used
214 for solution samples, while solid samples were measured in transmission mode. The
215 Mn K-edge XANES spectra, including δ-MnO_2, γ-MnOOH, $MnCl_2$ solid, and reaction
216 solution and sediment, were fitted using the Combo method, adhering to the protocols
217 and reference standards established in previous studies for determining Mn valence.[18]

218 **(13) XPS analysis**

219 X-ray photoelectron spectroscopy (XPS) was conducted on an ESCALAB 250XI
220 spectrometer (XPS, Escalab 250Xi, Thermo Fisher Scientific, USA) using an Al Kα X-
221 ray source to analyze the composition and valence state of surface elements. The high-
222 resolution C 1s spectrum was deconvoluted into four regions: (i) aliphatic and aromatic
223 carbons (C-C, C=C, C-H; 284.7), (ii) carbons in carbohydrates and amino groups (C-
224 O, C-N; 286.3), (iii) carbons in aldehyde, quinone, and amide groups (C=O, O-C-O,
225 O=C-N), and (iv) carbons in carboxylic acid groups (O-C=O; 289.1).[19, 20, 21] The high-
226 resolution N 1s spectrum was deconvoluted into three regions: aromatic nitrogen (399.2
227 eV), including pyridine, imine, and aniline derivatives; peptide bond nitrogen (400.4

Downloaded from pubs.acs.org/esthag/article-supplement/5459299/pdf/es6c12201_si_001/ by guest on 10 November 2026

228 eV), encompassing other amides, pyrrole, and secondary and tertiary amines; and
229 primary amine nitrogen (402.2 eV), which includes protonated amines.[22] For the high-
230 resolution O 1s spectrum, deconvolution resulted in five regions: metal-bound oxygen
231 (Mn-O-Mn; 529.6 eV), oxygen double-bonded to nitrogen (O=N-C/O=C; 531.3 eV),
232 hydroxyl oxygen (C-O-H; 532.5 eV), and ether oxygen and carboxylate (C-O-C/COOH;
233 533.7 eV).[23]

234 **(14) Computational Models and Methods**

235 Density Functional Theory (DFT) computations were performed using the ORCA
236 quantum-chemical package for geometric optimizations, frequency calculations, and
237 single-point energy evaluations.[24] The correlation energy was computed using TPSSh
238 Meta-hybrid functional and Grimme dispersion correction.[25, 26, 27] The TPSSh Meta-
239 hybrid functional was found to give better geometric and energetic properties between
240 transition metals and main-group elements.[28] The polarized all-electron basis sets of
241 triple-zeta quality (def2-TZVP) developed by Ahlrichs and co-workers were used for
242 the H, C, N, O, and Mn atoms.[29] The solvent effect was considered using the Polarizable
243 Continuum Model (PCM) of the SMD embedded in ORCA. Different initial
244 coordination geometries of the CT–Mn(II)–O_2 complex were evaluated, including
245 monodentate and bidentate coordination modes of CT to Mn(II). Upon geometry
246 optimization at the present level of theory, both initial geometries converged to the
247 same optimized structure featuring bidentate coordination of CT to Mn(II). This
248 structure was therefore adopted for subsequent analyses. The energy of the highest
249 occupied molecular orbital (HOMO) and the lowest unoccupied molecular orbital

Downloaded from pubs.acs.org/esthag/article-supplement/5459299/pdf/es6c12201_si_001/ by guest on 10 November 2026

(LUMO) of the optimized configuration was determined. The energy gap (E_g) is defined as the difference between E(HOMO) and E(LUMO).

Text S5: Solid-phase extraction (SPE) of humification product

Reaction solutions were diluted to 2.4 mg L^{-1} DOC using distilled water, yielding a final volume of 300 mL. The SPE columns were preconditioned with 18 mL of methanol followed by 18 mL of 0.01 M HCl. The samples were then acidified to pH 2.0 with 6.0 M HCl and gradually passed through the columns. After complete loading, the columns were flushed with an additional 18 mL of 0.01 M HCl to remove residual salts. The retained dissolved organic matter was subsequently eluted with 6 mL of methanol after drying the columns under a nitrogen stream. To enhance sample recovery, the flow-through fractions were collected and subjected to a second round of SPE extraction, after which the two methanolic extracts were combined. The sample was stored in a refrigerator at -20 °C and dissolved in 1 mL of methanol at a volume ratio of 1:50 before FT-ICR MS measurement.

To assess DOC recovery during SPE, 1.0 mL of the DOM eluate was dried under vacuum at 25 °C and 1,300 rpm for 180 min using a centrifugal concentrator (CV200, Beijing JM Instrument Co., Ltd., China).[30] The dried residue was subsequently re-dissolved in 7 mL of ultrapure water for further analysis. Based on DOC recoveries, this method achieved DOM extraction efficiencies exceeding 58% for all samples.[31]

Text S6: Calculation of parameters related to the molecular properties of the humification product based on FT-ICR MS

Downloaded from pubs.acs.org/esthag/article-supplement/5459299/pdf/es6c12201_si_001/ by guest on 10 November 2026

Molecular weight (MW), O/C ratio, H/C ratio, N/C ratio, double bond equivalent per carbon (DBE/C), modified aromatic index (AI_{mod}), and nominal oxidation state of carbon (NOSC) were calculated as follows：

$$O/C = o/c$$

$$H/C = h/c$$

$$N/C = n/c$$

$$DBE/C = (1 + (2c - h + n)/2)/c$$

$$AI_{mod} = (1 + c - o/2 - h/2 - s)/(c - o/2 - n - s)$$

$$NOSC = 4 - [(4c + h - 3n - 2o - 2s)/c]$$

NOSC was calculated from the chemical formula, assuming that all elements are in their initial oxidation states (H = +1, O = −2, N = −3, and S = −2).

The intensity-weighted average O/C_w, H/C_w, N/C_w, $NOSC_w$, MW_w, DBE/C_w, and AI_{modw} were calculated as follows:

$$O/C_w = \Sigma[O/C_i \times (I_i/\Sigma I_i)]$$

$$H/C_w = \Sigma[H/C_i \times (I_i/\Sigma I_i)]$$

$$N/C_w = \Sigma[N/C_i \times (I_i/\Sigma I_i)]$$

$$NOSC_w = \Sigma[NOSC_i \times (I_i/\Sigma I_i)]$$

$$MW_w = \Sigma[MW_i \times (I_i/\Sigma I_i)]$$

$$DBE/C_w = \Sigma[DBE/C_i \times (I_i/\Sigma I_i)]$$

$$AI_{modw} = \Sigma[AI_{modi} \times (I_i/\Sigma I_i)]$$

The relative abundance (RA_i) and Relative intensity (RI) of the molecule are calculated as follows:

Downloaded from pubs.acs.org/esthag/article-supplement/5459299/pdf/es6c12201_si_001/ by guest on 10 November 2026

$$RA_i = I_i/\Sigma I_i$$

where I_i represents the intensity of an individual molecule.

$$\text{Relative intensity (RI)} = I_i/I_{max}$$

where I_{max} represents the intensity of the most intense peak in the corresponding mass spectrum.

Text S7: KMD (COO/O/NH)-based homologous

KMD analysis converts the exact mass of a molecule based on the mass defect of a characteristic unit (e.g., NH or COO). Therefore, all molecules within a homologous series (i.e., molecules differing only in the number of NH or COO groups) will have the same KMD value and appear on the same horizontal line in the Kendrick plot (KMD values versus nominal mass values).[32] Herein, we screened all molecules with identical KMD values to identify homologous series characterized by varying numbers of COO, O, and NH groups. KMD (COO/O/NH) was calculated as follows:

$$\text{KMD (COO/O/NH)} = \text{nominal mass of a molecule} - \text{Kendrick mass (COO/O/NH)}$$

$$\text{Kendrick mass (COO/O/NH)} = \text{exact mass of molecule} * \frac{\text{nominal mass of COO/O/NH}}{\text{exact mass of COO/O/NH}}$$

where nominal mass of a molecule is the nearest integer of the exact mass of the molecule. Nominal mass of COO is 44, and exact mass of COO is 43.989829. Nominal mass of O is 16, and exact mass of O is 15.994915. Nominal mass of NH is 15, and exact mass of NH is 15.010898.

Text S8: Molecular similarity between Mn^{2+}-catalyzed organic polymers and natural DOM

Downloaded from pubs.acs.org/esthag/article-supplement/5459299/pdf/es6c12201_si_001/ by guest on 10 November 2026

Fourteen environmental samples (S1–S14; Table S2), encompassing agricultural and forest soils, freshwater systems across China, and a standard reference NOM, were examined to compare the molecular composition of DOM with that of Mn^{2+}-catalyzed products. Agricultural soils included S1–S6, S9, S11, and S13, collected from various regions in China: S1 from Shehong, Sichuan; S2 from Xianyang, Shanxi; S3 from Suihua, Heilongjiang; S4 from Xianning, Hubei; S5 from Changsha, Hunan; S6, a paddy soil, and S13, a dryland soil, both from Zhanjiang, Guangdong; S9 from Chengmai County, Hainan; and S11 from Ningbo, Zhejiang. Forest soils included S7 from Wuhan Botanical Garden, Hubei, and S14 from Changsha, Hunan. Freshwater samples were collected from the Yangtze River (S8) and East Lake (S10), both in Hubei Province. S12 was a standard Suwannee River NOM (SRNOM, 2R101N) obtained from the IHSS. FT-ICR MS data representing the DOM fraction were derived from previously published datasets, with portions accessed under permission from the original investigators.[33, 34, 35] All samples were analyzed on the same FT-ICR MS instrument (Solarix XR, Bruker, Germany) following consistent solid-phase extraction (SPE) and analytical protocols.

To evaluate the environmental relevance of Mn^{2+}-catalyzed products, molecular formulas identified in the 24 h Mn^{2+}-CGG reaction products were compared with those from natural samples based on FT-ICR MS data. The formula was regarded as environmentally detectable if it was also found in any natural sample. For each sample, the matching rate was calculated as the ratio of the number of product formulas detected in that sample to the total number of product formulas.

Downloaded from pubs.acs.org/esthag/article-supplement/5459299/pdf/es6c12201_si_001/ by guest on 10 November 2026

Text S9: Effect of phenolic species on Mn(II) driving humic-like substance formation

The effects of various phenolic compounds—hydroquinone (Hyd), phenol (Phe), catechol (CT), and resorcinol (Re)—on the Mn^{2+}-driven humification reaction were investigated in mixtures with glucose (Glu) and glycine (Gly), referred to collectively as HGG, PGG, CGG, and RGG, respectively. As shown in Figure S7a, only HGG exhibits a pronounced increase in A_{400} in the absence of Mn^{2+}, indicating that the spontaneous oxidative polymerization of Hyd drives humification. Figure S7b and S7c present the E_{600} values and humic-like acid (HLA) concentrations after 96 h of reaction with and without Mn^{2+}, and the enhancement effects of Mn^{2+}, calculated from these differences, are displayed in Figure S7d and S7e. The results demonstrate that Mn^{2+}-promoted humification follows the order: CGG > RGG > HGG > PGG.

To assess molecular stability, the energies of the highest occupied molecular orbital (E(HOMO)) and the lowest unoccupied molecular orbital (E(LUMO)), as well as the energy gap (E_g, E(HOMO)–E(LUMO)), were calculated using density functional theory (DFT) (Figure S7f). A higher E(HOMO) indicates greater electron-donating ability, while a lower E_g denotes less stability. Hyd exhibits the highest E(HOMO) and lowest E_g, indicating its higher instability and susceptibility to oxidation. This is consistent with the significantly higher $A_{400,}$ E_{600}, and HLA concentrations observed for HGG after 96 h of reaction in the absence of Mn^{2+}. However, in the presence of Mn^{2+}, the formed HLA in the HGG system is less than that in the CGG and RGG systems,

Downloaded from pubs.acs.org/esthag/article-supplement/5459299/pdf/es6c12201_si_001/ by guest on 10 November 2026

suggesting that the stability and reducing ability of phenolic species are not primary determinants in the Mn^{2+}-driven catalytic oxidation reaction.

A summary based on previous literature yields that the pK_a of the four phenols follows the order: Phe > Hyd > Re > CT (Phe = 9.98[36, 37], Hyd = 9.96[36, 37], Re = 9.44[36, 37], CT = 9.34[38, 39]), which is inversely related to their Mn^{2+}-driven polymerization. Lower pK_a values suggest that phenolic hydroxyl groups deprotonate more readily to form phenoxy anions, which are more likely to be complexed with Mn^{2+}. Moreover, phenoxide anions are more reactive than their protonated counterparts and readily undergo redox transformation via proton-coupled electron transfer to form phenoxyl radicals, which serve as crucial intermediates in the formation of phenolic polymers.[40, 41] Notably, the weak Mn^{2+}-induced enhancement observed in the PGG system is likely related to the structural and electronic characteristics of phenol. Its single hydroxyl group precludes bidentate coordination with Mn^{2+}, while its relatively high pK_a disfavors deprotonation, together weakening Mn^{2+}–ligand interactions and limiting the formation of reactive phenoxide species. These features likely render phenol less susceptible to Mn^{2+}-promoted oxidative polymerization than the other phenolic species examined. The lower E(HOMO) and higher E_g of phenol further suggest lower electron-donating ability and greater intrinsic stability, which may also reduce its reactivity. Thus, the minimal Mn^{2+}-driven polymerization observed for monohydroxy-substituted phenols likely arises primarily from limited coordination and less favorable deprotonation, and greater molecular stability. For dihydroxy-substituted phenols, Mn^{2+}-driven polymerization follows the order ortho > meta > para. The proximity of

Downloaded from pubs.acs.org/esthag/article-supplement/5459299/pdf/es6c12201_si_001/ by guest on 10 November 2026

379 hydroxyl groups facilitates bidentate coordination with Mn^{2+}, enabling the formation
380 of metal–organic coordination centers, while a lower pK_a further enhances the catalytic
381 reactivity. These results suggest that the spontaneous oxidative polymerization is likely
382 governed primarily by molecular stability and redox potential, whereas the catalytic
383 role of Mn^{2+} in humification is largely determined by phenol pK_a and coordination
384 mode, which are dictated by the number and positions of hydroxyl substituents.

385 **Text S10: Concentration effect of Mn(II) in driving humic-like substances**
386 **formation and deposition**

387 Figure S11a and S11b show that the initial Mn^{2+} concentrations significantly
388 influence the degree of humification, as indicated by changes in A_{400} and E_{600}. Below
389 1 mM, final A_{400} and E_{600} values increase with Mn^{2+} concentration, plateau at 1–2 mM,
390 and decline at 4–6 mM, likely due to enhanced precipitation of humification products,
391 consistent with the pronounced DOC decrease at higher Mn^{2+} levels (Figure S11c).
392 Meanwhile, cumulative CO_2-C production remains below 500 μg at all Mn^{2+}
393 concentrations, representing less than 0.3% of the initial carbon input calculated from
394 the added CGG precursors (Figure S11d). Thus, the DOC decrease is mainly
395 attributable to precipitation, whereas mineralization was negligible. Figure S12a–c
396 indicates that higher Mn^{2+} concentrations accelerate CT conversion, whereas Mn^{2+}
397 precipitation initiates at 2 mM and becomes substantial at 4–6 mM (Figure S12d),
398 consistent with the trends observed in DOC, A_{400}, and E_{600}. In the absence of CGG,
399 Mn^{2+} remains largely soluble over 96 h (Figure S12e), suggesting that Mn^{2+}
400 precipitation depends on its association with polymeric products. Collectively, these

Downloaded from pubs.acs.org/esthag/article-supplement/5459299/pdf/es6c12201_si_001/ by guest on 10 November 2026

findings suggest that elevated Mn^{2+} promotes precursor polymerization and drives the formation of Mn^{2+}–polymer complexes, facilitating their deposition.

EEM was used to track changes in fluorescence components during the reaction under different Mn^{2+} concentrations (Figure S13). At 0.5 mM Mn^{2+}, the catechol-associated fluorescence peak (Ex/Em = 275/315 nm) gradually decreases,[6] while a new peak (Ex/Em = 328/460 nm) emerges, characteristic of model humic-acid polymers.[42] At 2 and 4 mM Mn^{2+}, humic-related peaks initially intensify and then decline, reflecting their progressive deposition. At 4 mM Mn^{2+}, the fluorescence peak of the residual humic-like substances shifts to shorter wavelengths, indicating the accumulation of lower-molecular-weight components in solution.[42, 43, 44] These observations imply that the deposition process is accompanied by the fractionation of humic-like substances, with the highly aromatic and molecular weight fraction being preferentially deposited. This fractionation mechanism is further supported by the humification index (HIX), calculated from EEM spectra, which shows an initial increase followed by a decrease at 2 and 4 mM Mn^{2+}.

The concentrations of humic-like acid (HLA) and fulvic-like acid (FLA) in both the suspension and filtrate were quantified (Figure S14a). In the suspension, HLA exhibits a biphasic trend with increasing Mn^{2+} concentration, peaking at 2 mM before declining. This decline may stem from precipitation-driven fractionation, leading to partial dissociation and potentially accounting for the low-molecular-weight fluorescent products observed in EEM at higher Mn^{2+} concentrations (4 mM). The discrepancy in HLA and FLA concentrations between the suspension and filtrate

Downloaded from pubs.acs.org/esthag/article-supplement/5459299/pdf/es6c12201_si_001/ by guest on 10 November 2026

confirms the extent of precipitation (Figure S14b). Elevated Mn^{2+} additions (2-6 mM) promote greater HLA precipitation, whereas FLA remains largely in solution, indicating that HLA is the predominant contributor to the precipitate. This interpretation is supported by Figure S12c, which shows that the HLA/FLA ratio in the suspension increases with rising Mn^{2+} concentrations, whereas the corresponding ratio in the filtrate rises initially and then declines.

The formed HLA was further characterized by FTIR (Figure S15a). The functional groups corresponding to the characteristic peaks of the IR spectra are summarized in Table S7. The various functional groups of HLA always lead to overlapping IR peaks, resulting in ambiguous band assignments, thus the 2D-IR-COS was used to analyze the differences in HLA characteristic functional groups under varying Mn^{2+} concentrations (Figure S15a). Among 2D-COS synchronous maps, five autopeaks are identified (1720 cm^{-1}, 1605 cm^{-1}, 1498 cm^{-1}, 1389 cm^{-1}, 1240 cm^{-1}), the most relevant characteristic peaks concerning Mn^{2+} concentration. Positive cross-peaks are observed at (1720/1605), (1605/1385), (1605/1288), (1605/1498), and (1605/1240) cm^{-1}, indicative of their synchronous variation. The integration of IR spectra and 2D-COS synchronous maps reveal that heightened Mn^{2+} concentrations predominantly enhance the levels of C=C, C=O, C-O, and C-N bonds. These bonds predominantly emanate from the benzene ring, carboxylic acid, ketone, ether, and amide structures, suggesting an increase in aromaticity, oxygen-containing functional groups, and nitrogen substitutions. Notably, the autopeak of maximum intensity centered at 1605 cm^{-1}, underscores the pivotal role of Mn^{2+} concentration in shaping the aromaticity of humic-like acid. Furthermore, the

Downloaded from pubs.acs.org/esthag/article-supplement/5459299/pdf/es6c12201_si_001/ by guest on 10 November 2026

445 FTIR spectra reveal out-of-plane C-H deformation bands in the 900-700 cm^{-1} region
446 under varying Mn^{2+} concentrations (Figure S15a). These bands are indicative of
447 aromatic structures with isolated aromatic hydrogens (875 cm^{-1}), two adjacent
448 hydrogens per ring (825 cm^{-1}), and four adjacent aromatic hydrogens (753 cm^{-1}).[45] The
449 increased intensities of these diffraction peaks, particularly at 875 cm^{-1} and 753 cm^{-1} at
450 higher Mn^{2+} concentrations, indicate more benzene ring structures in the formed humic-
451 like acid. Furthermore, the degree of aromatic substitution and condensation in humic
452 acid can be inferred from the number of adjacent hydrogens on each aromatic ring. As
453 the Mn^{2+} concentration increases, the aromatic structures with isolated aromatic
454 hydrogens (875 cm^{-1}) significantly increase, indicating a higher degree of aromatic
455 substitution and condensation.[45]

456 The EPR spectra of the formed humic-like acid samples are presented in Figure
457 S15b. A characteristic organic free radical signal with a g value of 2.002, attributed to
458 carbon-centered persistent free radicals (PFRs),[46, 47] is detected in all samples.
459 Increasing Mn^{2+} concentrations enhance the signal intensity of PFRs, indicating greater
460 aromaticity, a higher degree of humification, and a greater number of species with
461 unpaired electrons in the formed humic-like acid.[46, 48, 49] This species accumulation with
462 unpaired electrons suggests an Mn^{2+}-driven single-electron transfer process during
463 polymerization. Previous studies have shown that PFRs are generally stabilized by
464 strong surface binding with transition metal minerals,[50, 51] cation-π interactions,[52, 53] and
465 interactions between aromatic rings.[54] Since no transition metal minerals are involved
466 in this study, we hypothesize that the stabilization of PFRs is facilitated by interactions

Downloaded from pubs.acs.org/esthag/article-supplement/5459299/pdf/es6c12201_si_001/ by guest on 10 November 2026

between organic molecules, such as aromatic conjugation, hydrophobic interactions, and hydrogen bonding, coupled with complexation with Mn^{2+} ions forming cation-π interactions.[54, 55]

Collectively, HLAs formed at higher Mn^{2+} concentrations are enriched in aromatic and oxygen-containing functionalities and exhibit increased persistent radical content. These compositional shifts are expected to promote charge- and hydrophobic-driven self-assembly of HLA–Mn^{2+} complexes, enhancing π–π stacking, hydrophobic interactions, which induce selective aggregation and precipitation of highly aromatic macromolecular fractions.

Downloaded from pubs.acs.org/esthag/article-supplement/5459299/pdf/es6c12201_si_001/ by guest on 10 November 2026

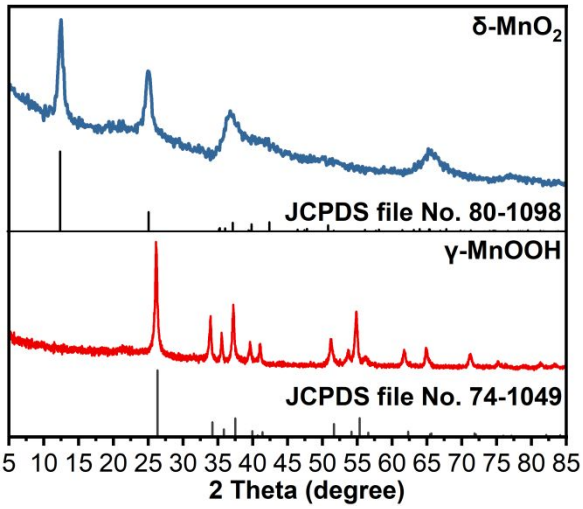


Figure S1: The XRD pattern of the synthesized δ-MnO_2 and γ-MnOOH.

Downloaded from pubs.acs.org/esthag/article-supplement/5459299/pdf/es6c12201_si_001/ by guest on 10 November 2026

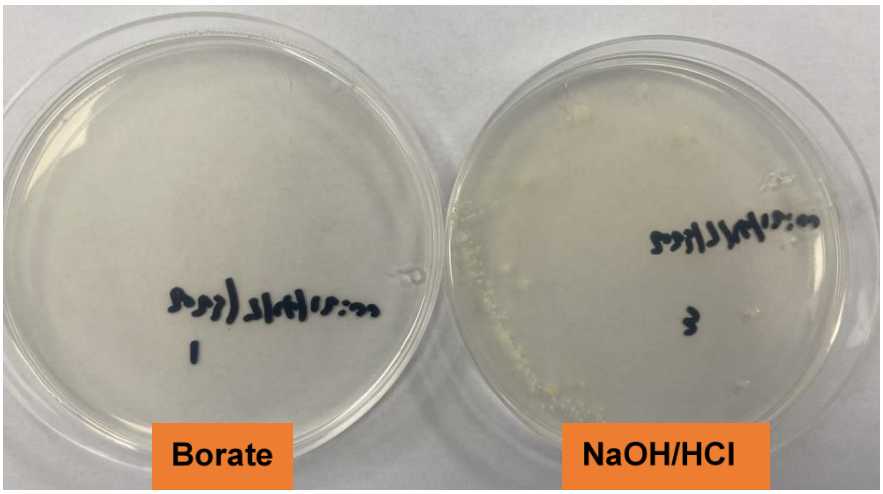


Figure S2: Antibacterial effect of Mn^{2+}–CGG reaction solutions on nutrient agar. Nutrient agar plates were inoculated with Mn^{2+}-CGG mixtures after a 96 h reaction period, with pH regulated by either borate buffer (left) or NaOH/HCl (right). After 7 days of incubation, no microbial growth was observed in the borate buffer system (left), whereas microbial growth occurred in the NaOH/HCl (right) control system. These results indicate that the borate buffer effectively meets the sterilization requirements of this experiment.

Downloaded from pubs.acs.org/esthag/article-supplement/5459299/pdf/es6c12201_si_001/ by guest on 10 November 2026

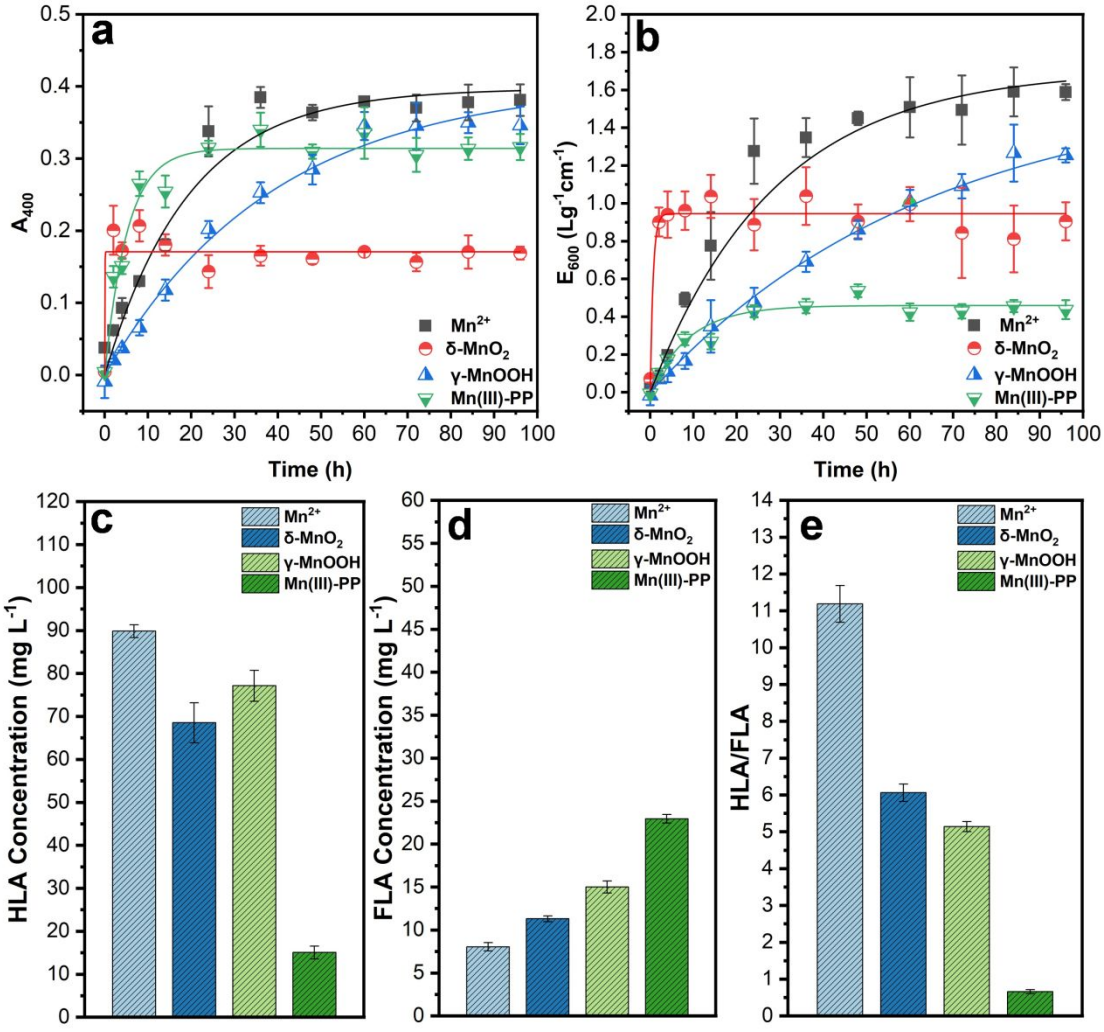


Figure S3: Humification driven by manganese species with different oxidation states. Variations in (a) A_{400} and (b) E_{600} during the reaction of catechol–glucose–glycine (CGG) with different Mn species (Mn^{2+}, δ-MnO_2, γ-MnOOH, Mn(III)-PP) under an air atmosphere (O_2), as well as (c) concentrations of humic-like acids (HLA), (d) fulvic-like acids (FLA), and (e) the ratios of HLA and FLA concentrations (HLA/FLA) following the reaction. Experimental conditions: catechol (CT) = 2 mM, glucose (Glu) = 6 mM, glycine (Gly) = 6 mM, Mn = 2 mM, pH = 8.0, 25 °C, dark. Data are presented as mean ± SD (n = 3)

Downloaded from pubs.acs.org/esthag/article-supplement/5459299/pdf/es6c12201_si_001/ by guest on 10 November 2026

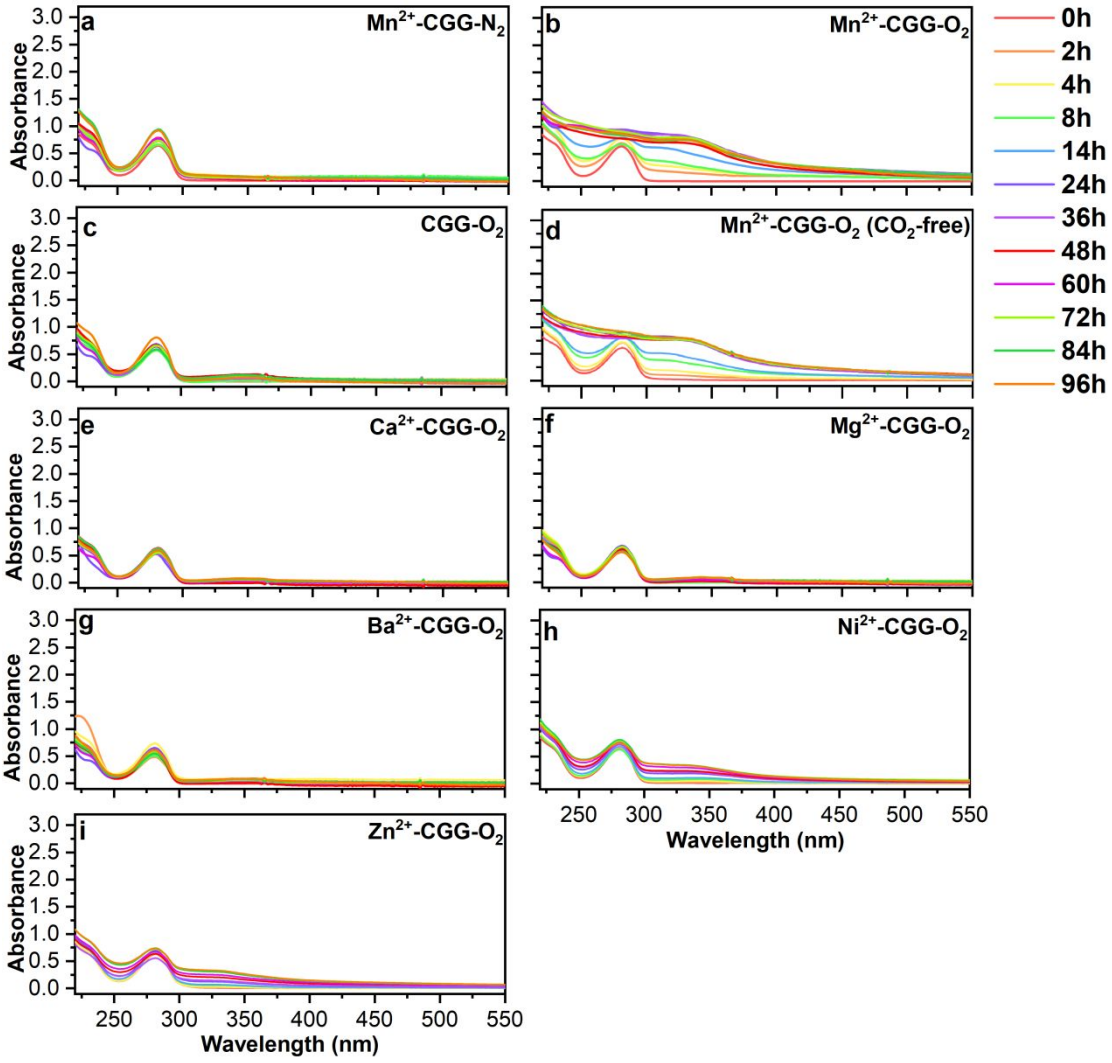


Figure S4: Effect of divalent cations and gas conditions on CGG humification monitored by UV–vis spectroscopy. Time-dependent UV–vis spectra of CGG solutions reacted with Mn^{2+} under N_2 (a), Mn^{2+} under O_2 (b), without added cations under O_2 (control; c), Mn^{2+} under O_2 (CO_2-free) (d), Ca^{2+} under O_2 (e), Mg^{2+} under O_2 (f), Ba^{2+} under O_2 (g), Ni^{2+} under O_2 (h), and Zn^{2+} under O_2 (i) over a 96 h reaction period. Experimental conditions: CT = 2 mM, Glu = 6 mM, Gly = 6 mM, cation (Ca^{2+}, Mg^{2+}, Ba^{2+}, Ni^{2+}, Zn^{2+}, or Mn^{2+}) = 2 mM, pH = 8.0, 25 °C, in the dark. The O_2 condition denotes exposure to ambient air, whereas the CO_2-free aerobic condition was established using synthetic air containing 21% O_2 and 79% N_2 (v/v).

Downloaded from pubs.acs.org/esthag/article-supplement/5459299/pdf/es6c12201_si_001/ by guest on 10 November 2026

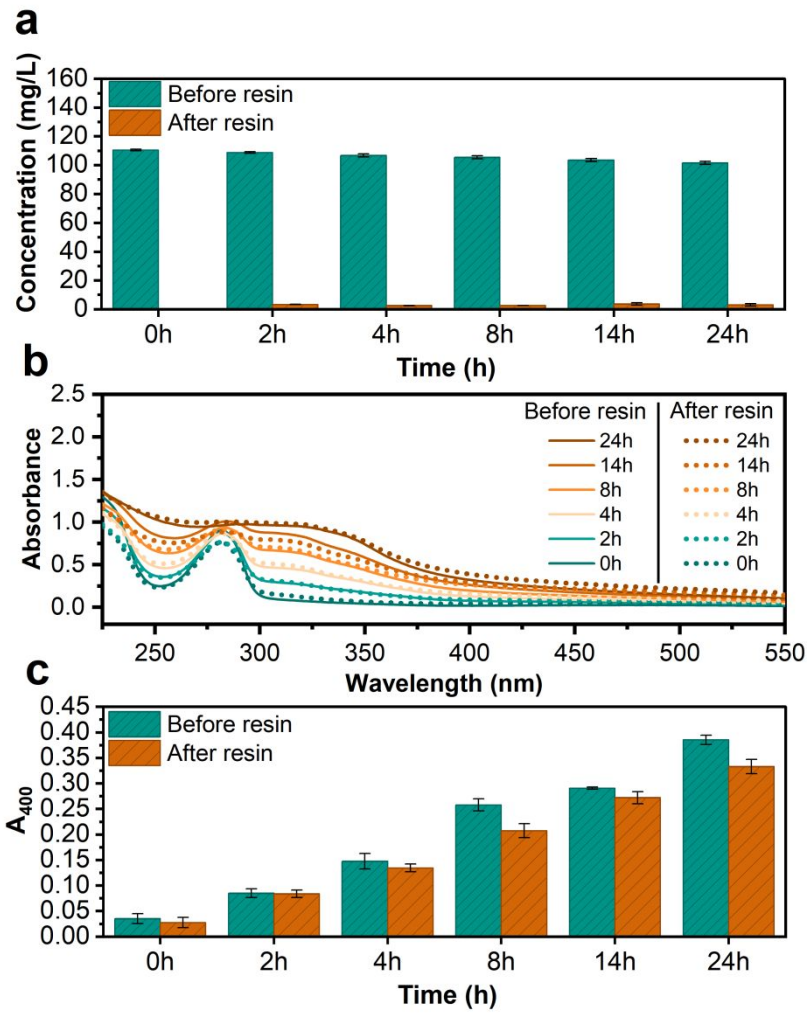


Figure S5. Effects of cation-exchange resin treatment on dissolved Mn concentrations and UV–vis spectral evolution in the Mn(II)-mediated reaction system. (a) Dissolved Mn concentrations, (b) UV–vis absorbance spectra, and (c) changes in A_{400} for untreated and resin-treated aliquots. Resin treatment was performed immediately prior to the corresponding measurements. Data are presented as mean ± SD (n = 3).

Downloaded from pubs.acs.org/esthag/article-supplement/5459299/pdf/es6c12201_si_001/ by guest on 10 November 2026

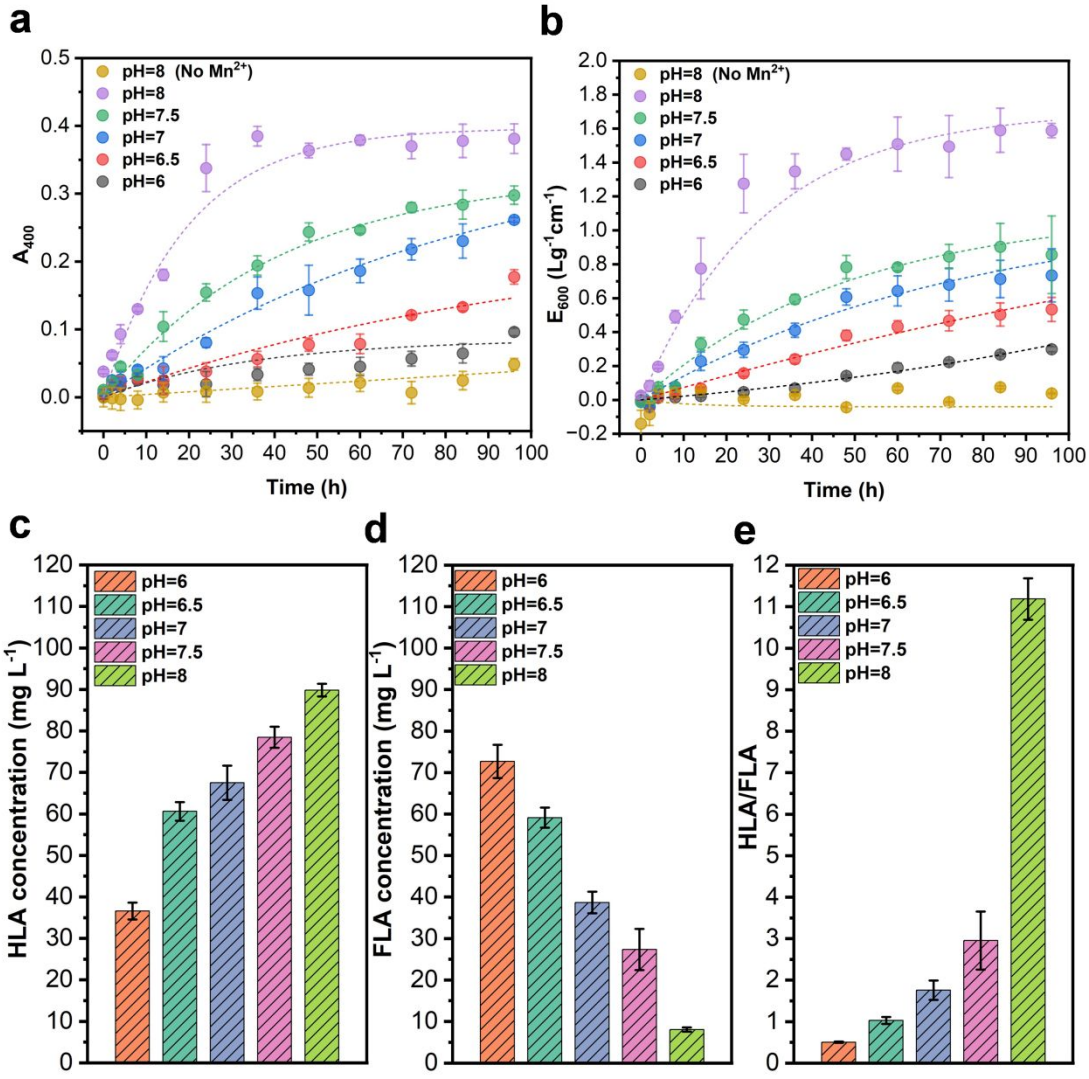
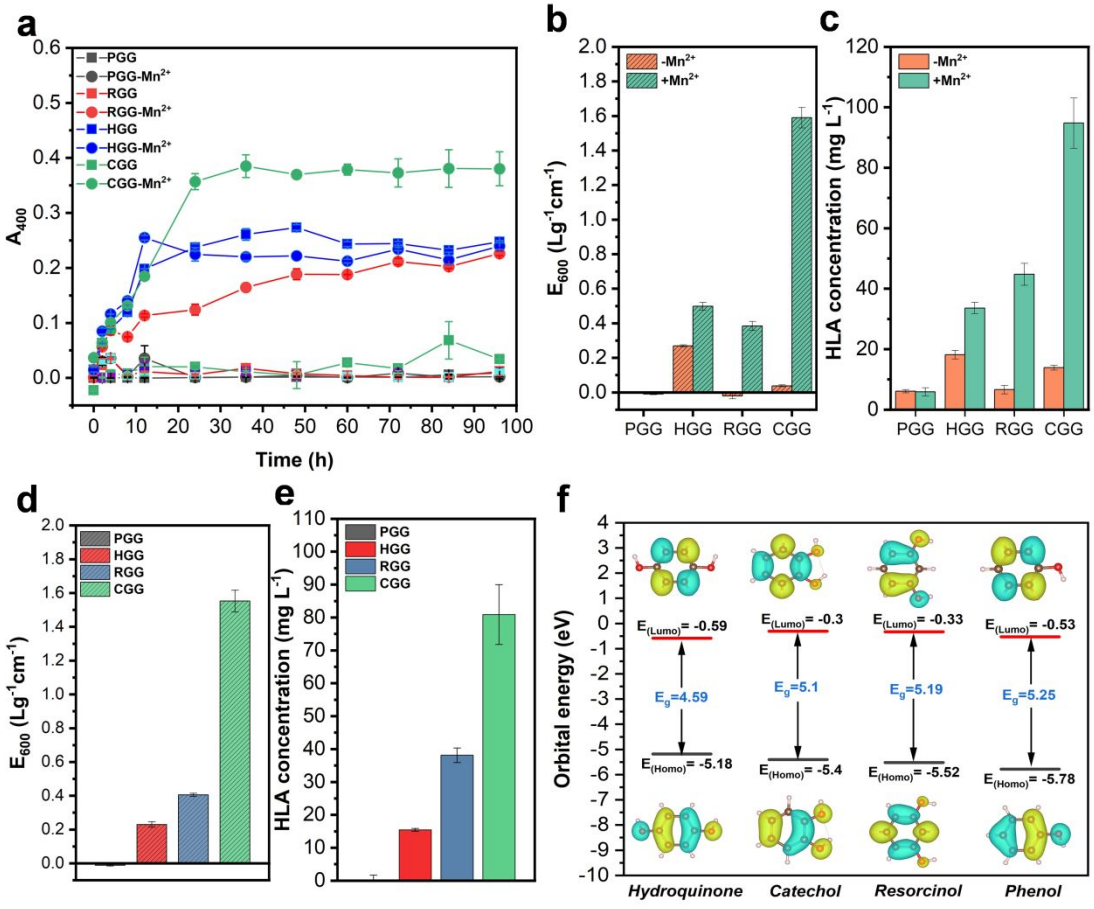


Figure S6: Effect of pH on Mn^{2+}-driven humification. Variations in (a) A_{400} and (b) E_{600} during the 96 h reaction of Mn^{2+} with CGG at pH 6.0-8.0 under O_2, along with (c) concentrations of HLA, (d) FLA, and (e) the HLA/FLA ratios after the reaction. Experimental conditions: CT = 2 mM, Glu = 6 mM, Gly = 6 mM, Mn^{2+} = 2 mM, pH = 6.0-8.0, 25 ℃, dark. Data are presented as mean ± SD (n = 3).

Downloaded from pubs.acs.org/esthag/article-supplement/5459299/pdf/es6c12201_si_001/ by guest on 10 November 2026



525

526 **Figure S7:** Effect of different phenolic precursors on Mn^{2+}-driven humification. (a)
527 Variations in A_{400} values for hydroquinone–glucose–glycine (HGG), catechol–
528 glucose–glycine (CGG), resorcinol–glucose–glycine (RGG), and phenol–glucose–
529 glycine (PGG) reacting with and without Mn^{2+} under O_2. (b) E_{600} values and (c) HLA
530 concentrations after a 96 h reaction for HGG, CGG, RGG, and PGG with and without
531 Mn^{2+}. (d) Differences in E600 values and (e) HLA concentrations between reactions
532 with Mn^{2+} ($+Mn^{2+}$) and without Mn^{2+} ($-Mn^{2+}$). (f) Frontier orbital energy levels of
533 different phenolic compounds. Experimental conditions: Phenolic compounds
534 (hydroquinone (Hyd); resorcinol (Re); catechol (CT); phenol (Phe)) = 2 mM, Glu = 6

Downloaded from pubs.acs.org/esthag/article-supplement/5459299/pdf/es6c12201_si_001/ by guest on 10 November 2026

mM, Gly = 6 mM, Mn^{2+} = 2 mM, pH = 8.0, 25 °C, dark. Data are presented as mean ± SD (n = 2)

Downloaded from pubs.acs.org/esthag/article-supplement/5459299/pdf/es6c12201_si_001/ by guest on 10 November 2026

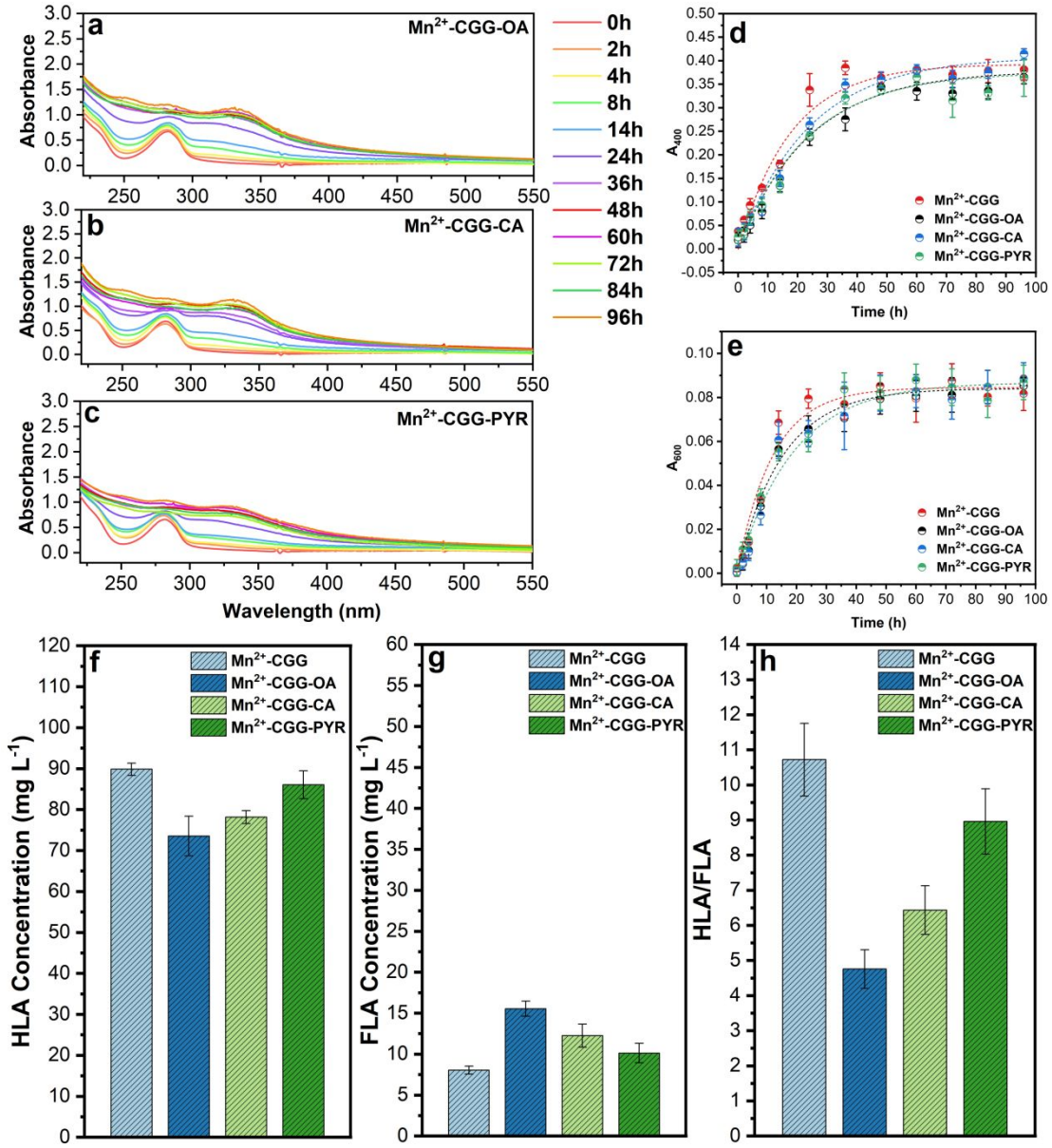


Figure S8. Effects of organic ligands on Mn^{2+}-mediated humification. Time-dependent UV–vis spectra of Mn^{2+}–CGG systems amended with oxalate (OA) (a), citrate (CA) (b), or pyruvate (PYR) (c). Temporal changes in A_{400} (d) and A_{600} (e). Concentrations of HLA (f) and FLA (g), and HLA/FLA ratios (h) after 96 h of reaction. Experimental conditions: CT = 2 mM, Glu = 6 mM, Gly = 6 mM, Mn^{2+} = 2 mM, OA, CA, or PYR = 2 mM, pH = 8.0, 25 °C, dark. Data are presented as mean ± SD (n = 3).

Downloaded from pubs.acs.org/esthag/article-supplement/5459299/pdf/es6c12201_si_001/ by guest on 10 November 2026

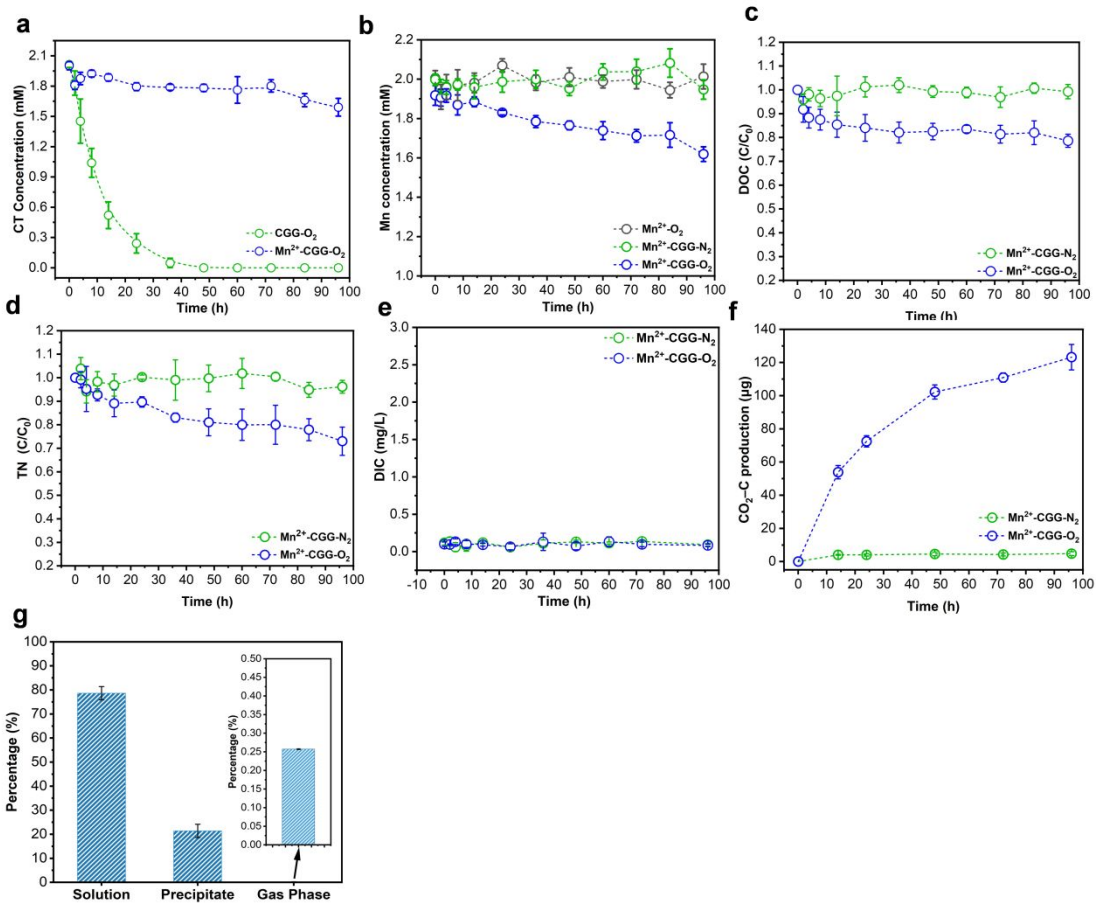


Figure S9: Temporal dynamics of key reactants and solution chemistry during Mn^{2+}-driven humification under oxic and anoxic conditions. Temporal variations in the concentrations of CT (a), Mn (b), dissolved organic carbon (DOC) (c), and total nitrogen (TN) (d) in solution during the reaction of Mn^{2+} with CGG under O_2 and N_2 conditions. Here, C and C_0 represent the DOC or TN concentration at the sampling time and the initial time, respectively. Temporal variations in dissolved inorganic carbon (DIC) under O_2 and N_2 conditions are shown in (e). CO_2 production measured at each sampling time in CO_2-free air and N_2-purged controls is shown in (f). Carbon distribution among the solution, precipitate, and gas phases at the end of the reaction is shown in (g). Experimental conditions: CT = 2 mM, Glu = 6 mM, Gly = 6 mM, Mn^{2+}

Downloaded from pubs.acs.org/esthag/article-supplement/5459299/pdf/es6c12201_si_001/ by guest on 10 November 2026

556 = 2 mM, pH = 8.0, 25 °C, dark. Data are presented as mean ± SD (n = 3)

Downloaded from pubs.acs.org/esthag/article-supplement/5459299/pdf/es6c12201_si_001/ by guest on 10 November 2026

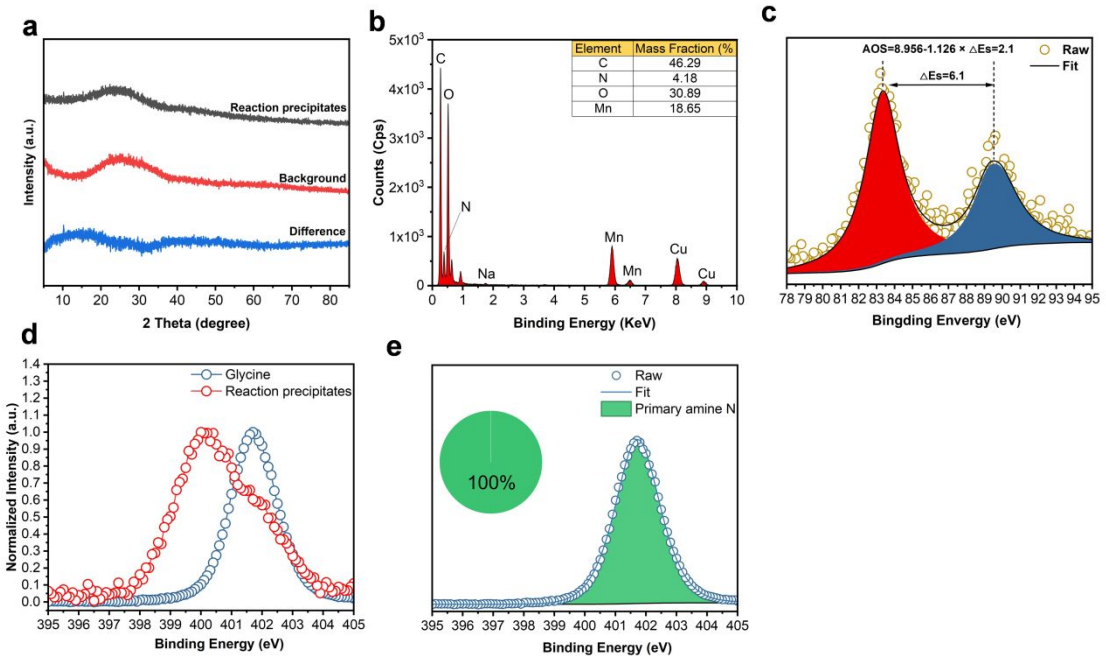


Figure S10: Characterization of precipitates formed after reaction. (a) XRD patterns, (b) surface elemental composition (Mn, O, C, N) determined by EDS analysis, and (c) high-resolution XPS spectra of Mn 3s for the post-reaction precipitates. The average oxidation state (AOS) of Mn was calculated from the Mn 3s peak splitting (ΔE_s) using the empirical relationship: $AOS = 8.956 - 1.126 \times \Delta E_s$, where ΔE_s is the separation between the Mn 3s doublet. (d) N 1s XPS spectra of pristine glycine and the CGG reaction precipitate. (e) Peak fitting of the N 1s XPS spectrum of pristine glycine.

Downloaded from pubs.acs.org/esthag/article-supplement/5459299/pdf/es6c12201_si_001/ by guest on 10 November 2026

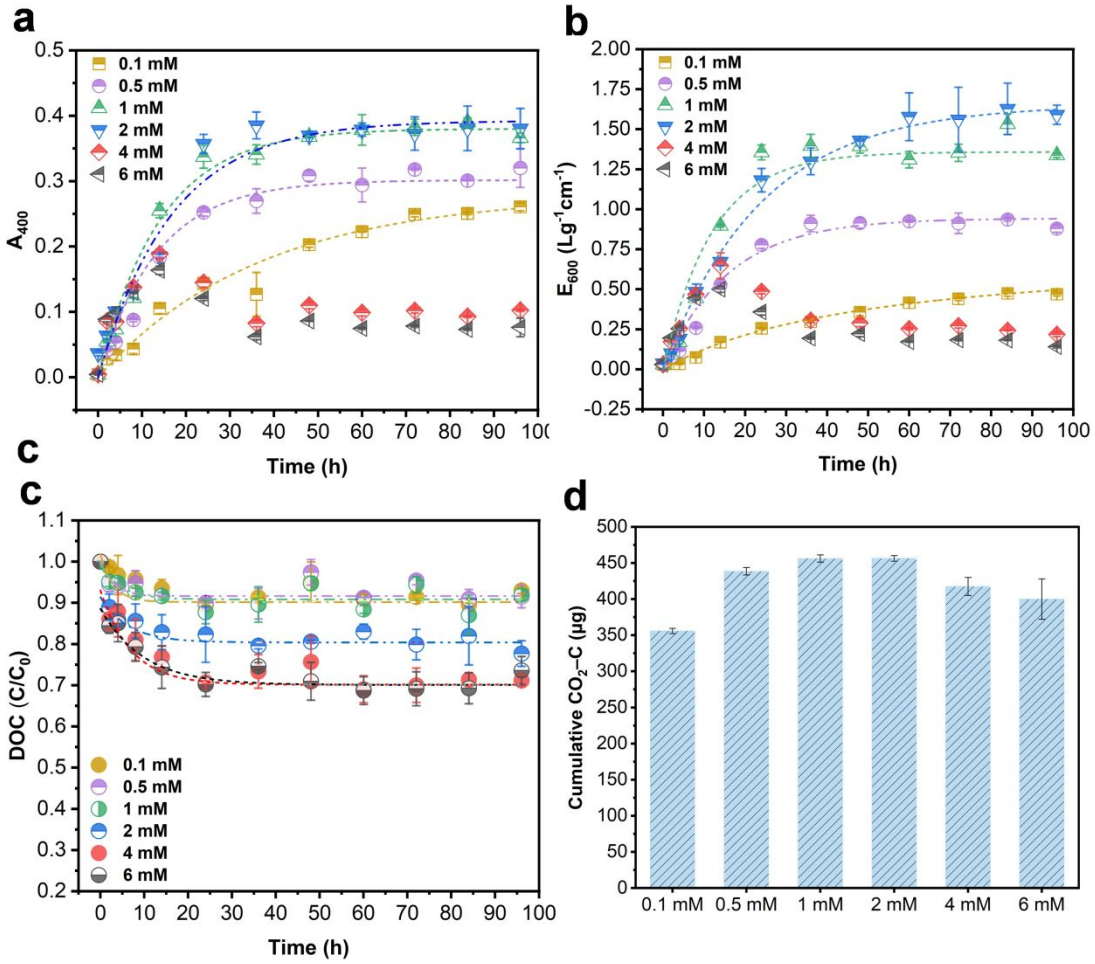


Figure S11: Effect of Mn^{2+} concentration on CGG humification and DOC dynamics. Variations in (a) A_{400}, (b) E_{600}, and (c) DOC for different concentrations of Mn^{2+} reacting with CGG. DOC values are expressed as C/C_0, where C denotes the DOC at a given reaction time, and C_0 is the initial DOC. (d) Cumulative CO_2-C after reaction under varying Mn^{2+} concentrations. Experimental conditions: CT = 2 mM, Glu = 6 mM, Gly = 6 mM, Mn^{2+} = 0.1 mM-6.0 mM, pH = 8.0, 25 ℃, dark. Data are presented as mean ± SD (n = 2)

Downloaded from pubs.acs.org/esthag/article-supplement/5459299/pdf/es6c12201_si_001/ by guest on 10 November 2026

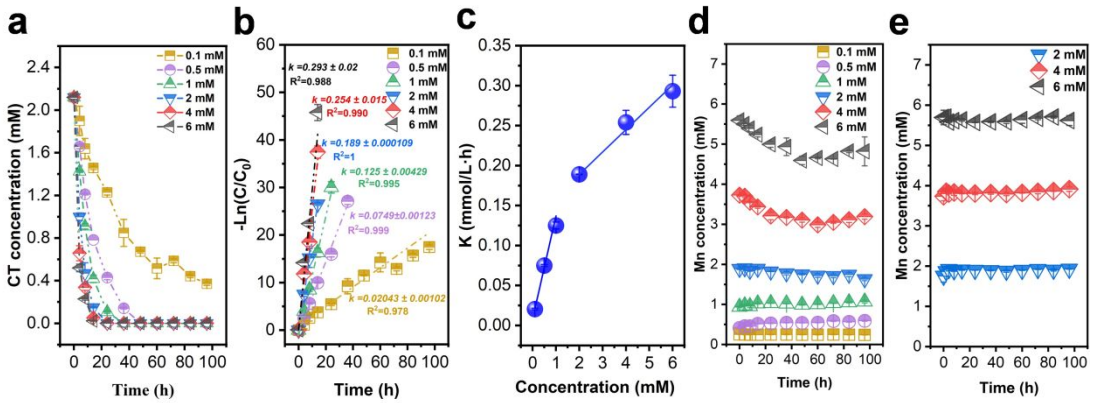


Figure S12: Kinetics of CT consumption and Mn^{2+} dynamics during CGG reactions with varying Mn^{2+} concentrations. (a) Changes in CT concentration during the reaction of CGG with different Mn^{2+} concentrations. (b) First-order kinetic fitting of CT concentration changes. (c) Variation of rate constants (k) with Mn^{2+} concentrations derived from the kinetic fitting. (d) Mn concentration changes during the reaction of CGG with different Mn^{2+} concentrations (e) Mn concentration changes without CGG. Experimental conditions: CT = 2 mM, Glu = 6 mM, Gly = 6 mM, Mn^{2+} = 2 mM, pH = 8.0, 25 ℃, dark. Data are presented as mean ± SD (n = 2)

Downloaded from pubs.acs.org/esthag/article-supplement/5459299/pdf/es6c12201_si_001/ by guest on 10 November 2026

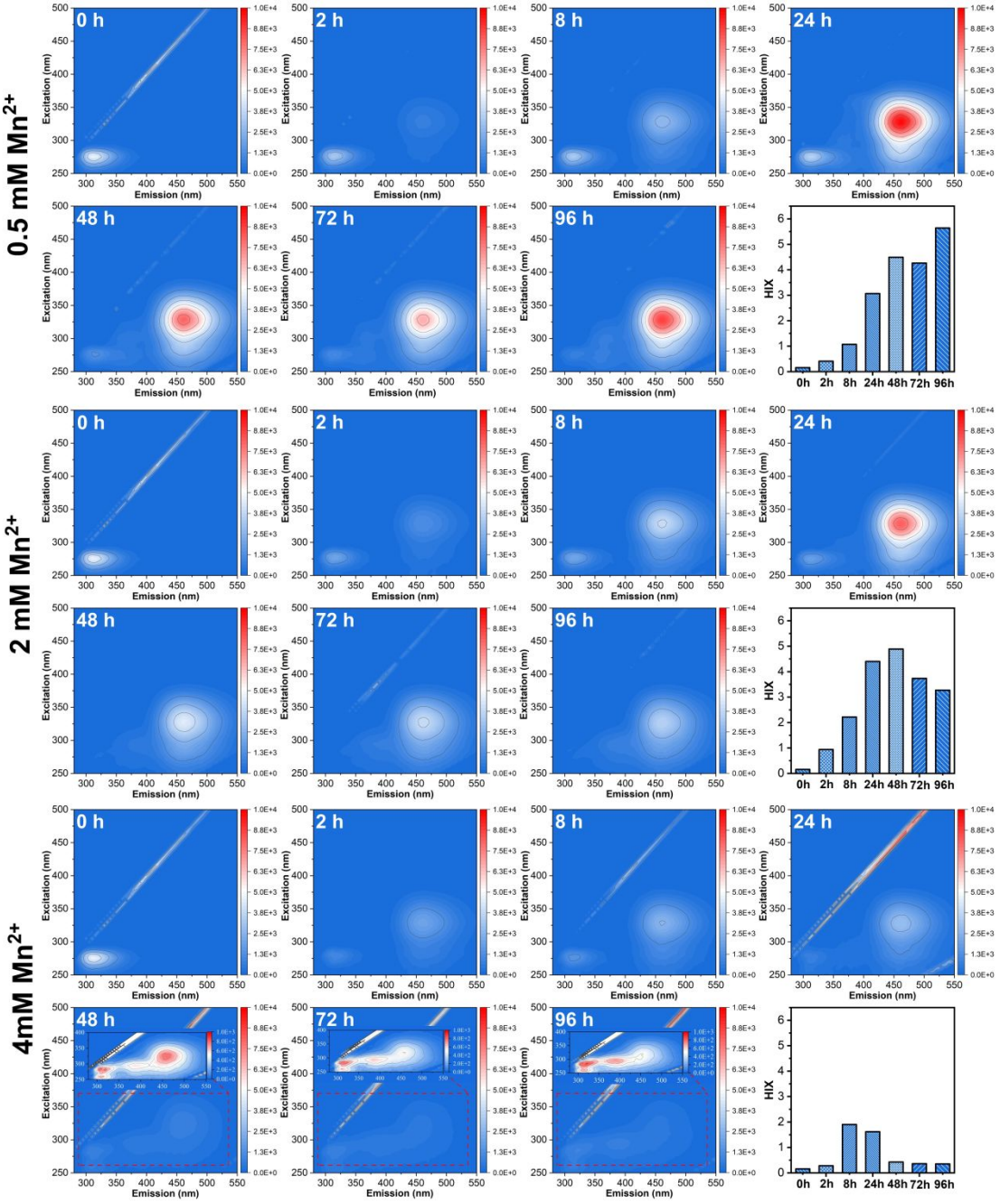
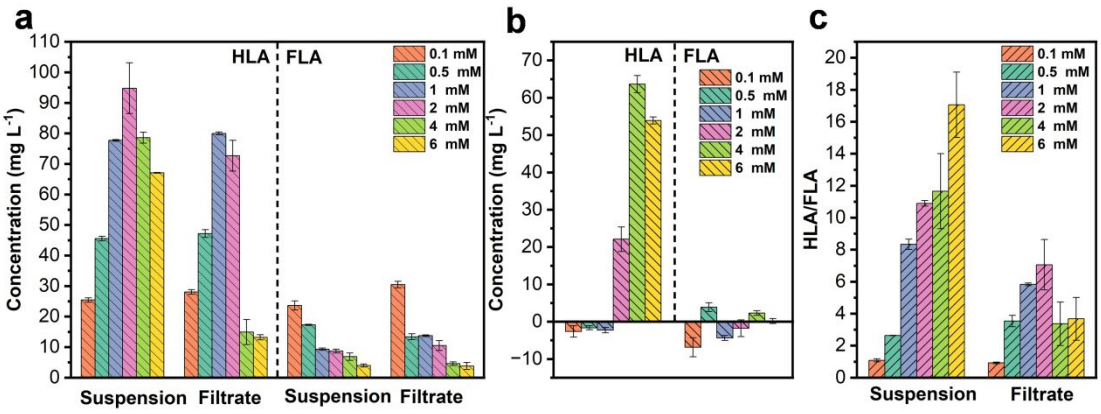


Figure S13: Variations of EEM spectrum and humification index (HIX) during the reaction of 0.5 mM, 2 mM, and 4 mM Mn^{2+} with CGG, respectively.

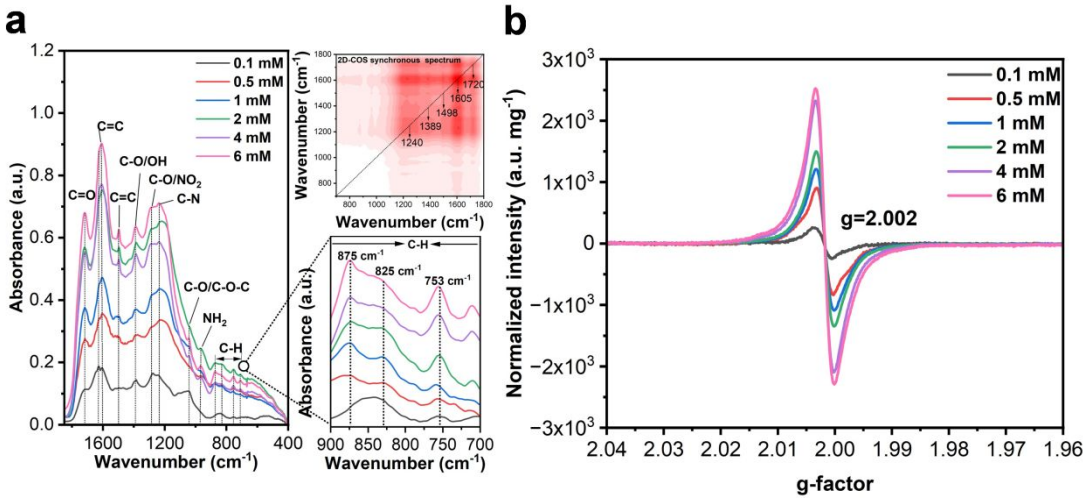
Downloaded from pubs.acs.org/esthag/article-supplement/5459299/pdf/es6c12201_si_001/ by guest on 10 November 2026

588 

589 **Figure S14:** Concentrations of HLA and FLA in suspension and filtrate under varying
590 Mn^{2+} concentrations. (a) Concentrations of HLA and FLA in suspension and filtrate;
591 (b) differences in HLA or FLA concentrations between suspension and filtrate; (c)
592 HLA/FLA ratios in suspension and filtrate, all measured after a 96 h reaction with
593 varying Mn^{2+} concentrations and CGG. Data are presented as mean ± SD (n = 2)

594

Downloaded from pubs.acs.org/esthag/article-supplement/5459299/pdf/es6c12201_si_001/ by guest on 10 November 2026



595

596 **Figure S15:** Characterization of HLA formed after Mn^{2+}-driven humification. (a) ATR-

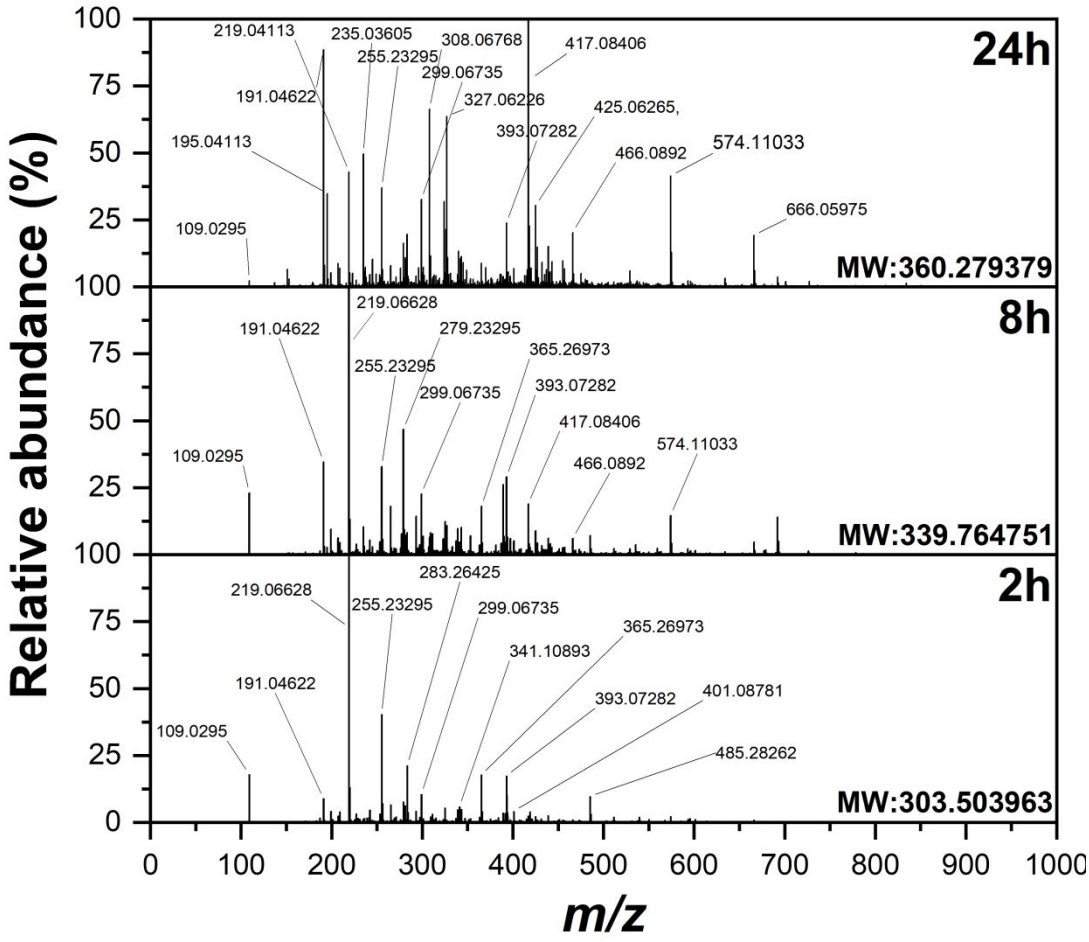
597 FTIR combined with 2D-COS spectra of HLA formed at different Mn^{2+} concentrations

598 (0.1–6.0 mM); (b) EPR spectra of HLA after a 96 h reaction with CGG at varying Mn^{2+}

599 concentrations.

600

Downloaded from pubs.acs.org/esthag/article-supplement/5459299/pdf/es6c12201_si_001/ by guest on 10 November 2026



601

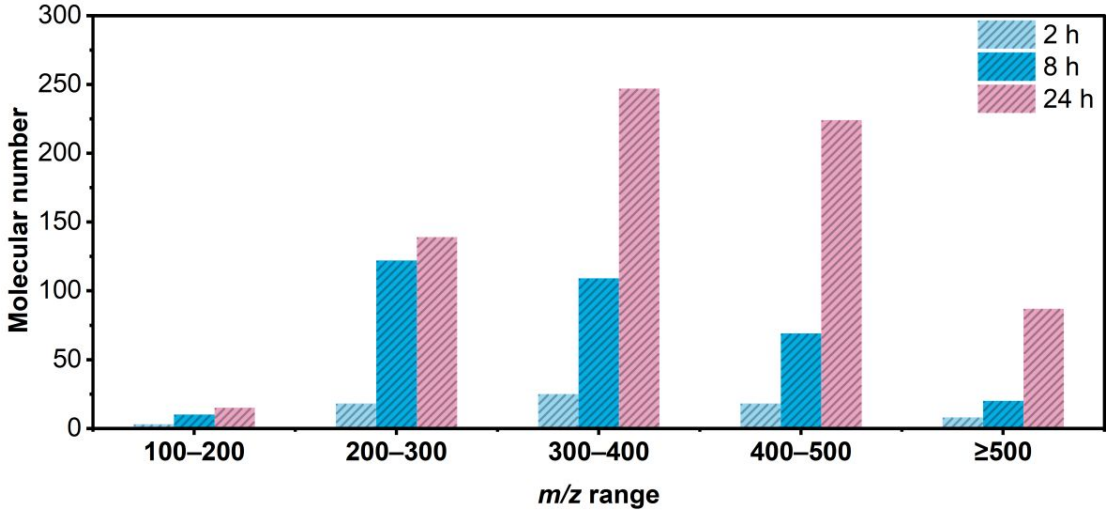
602 **Figure S16:** FT-ICR MS spectra of the products from the reaction of Mn^{2+} with CGG

603 at 2 h, 8 h, and 24 h. MW in the figure represents the signal intensity-weighted average

604 molecular weight.

605

Downloaded from pubs.acs.org/esthag/article-supplement/5459299/pdf/es6c12201_si_001/ by guest on 10 November 2026



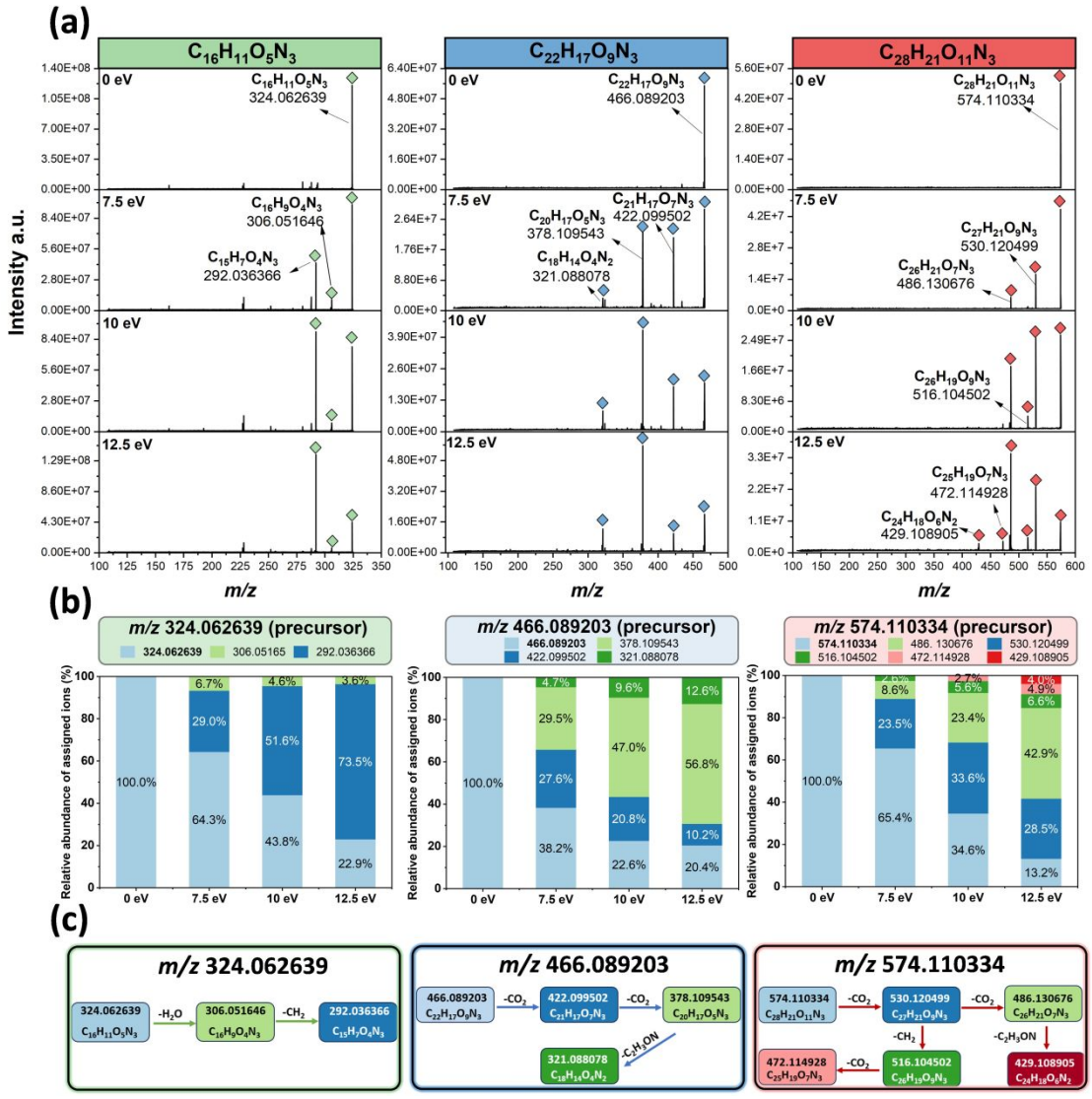
606

607 **Figure S17.** Temporal distribution of assigned CHON molecular formulas across

608 different *m/z* ranges.

609

Downloaded from pubs.acs.org/esthag/article-supplement/5459299/pdf/es6c12201_si_001/ by guest on 10 November 2026



610

611 **Figure S18.** Energy-resolved MS/MS characterization of representative high-mass N-
612 containing products. (a) MS/MS spectra of precursor ions at *m/z* 324.062639,
613 466.089203, and 574.110334 acquired at collision energies of 0, 7.5, 10, and 12.5 eV.
614 (b) Collision-energy-dependent redistribution of the precursor and major assigned
615 product ions, with relative abundances normalized to the summed intensities of the
616 precursor and major assigned product ions at each collision energy. (c) Major product-
617 ion relationships inferred from accurate-mass differences and elemental-composition
618 changes.

Downloaded from pubs.acs.org/esthag/article-supplement/5459299/pdf/esdc12201_si_001/ by guest on 10 November 2026

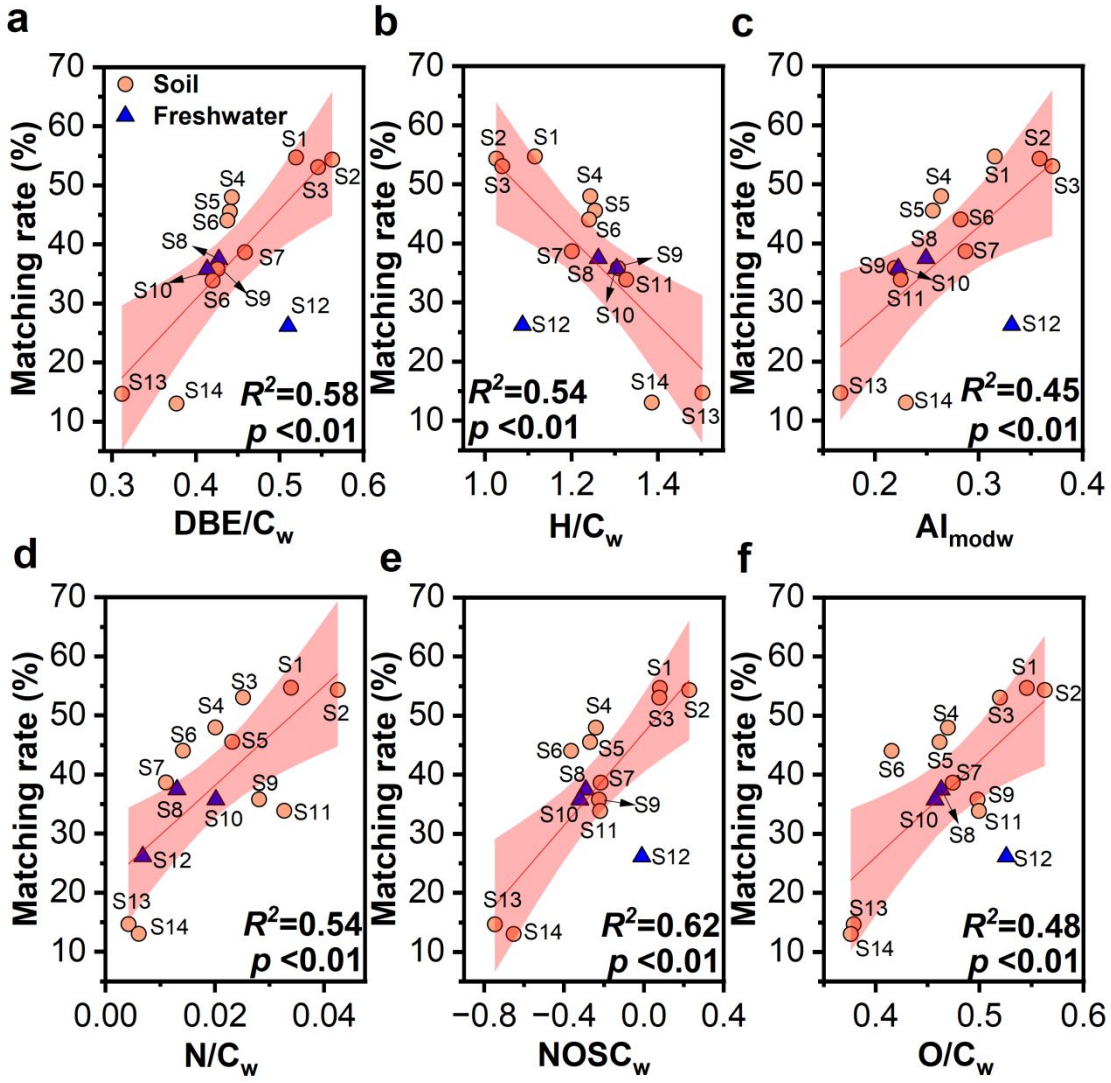
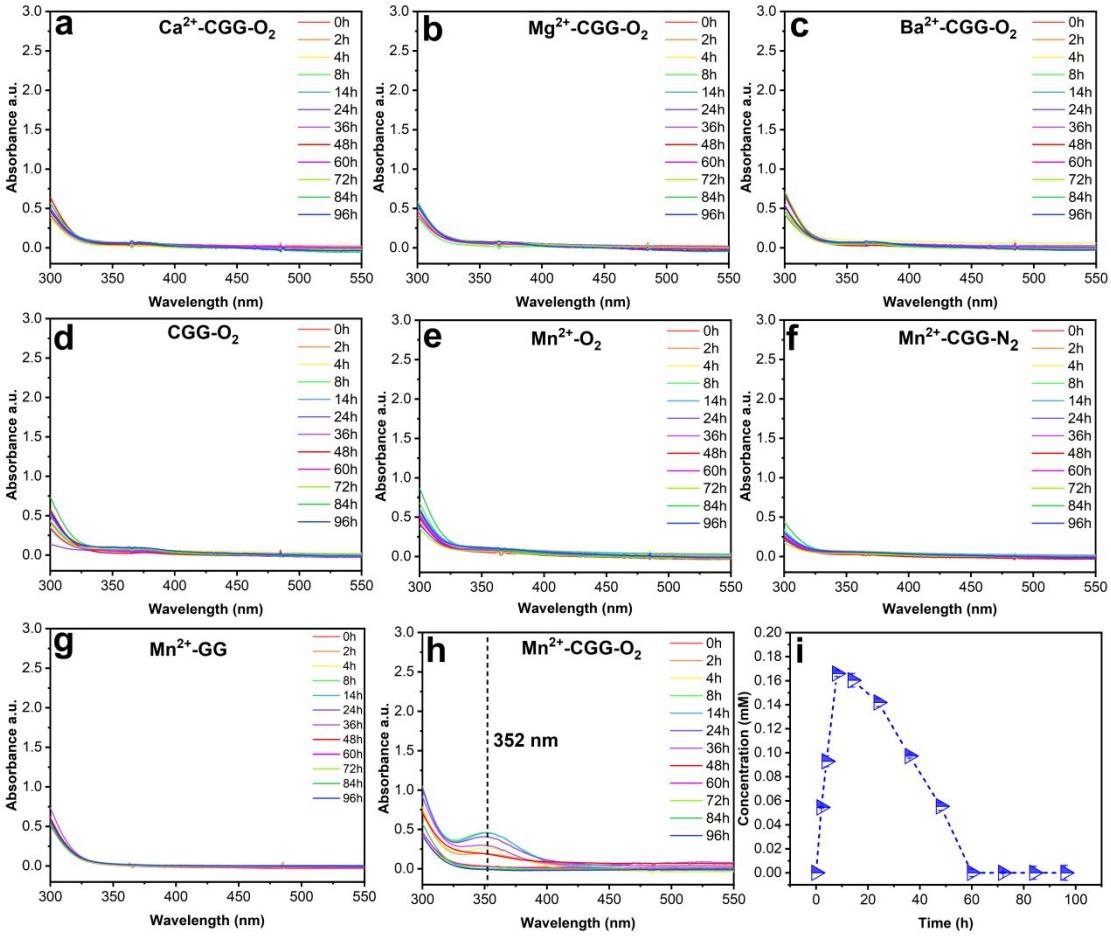


Figure S19. (a–f) Linear relationships between the formula-matching rate and weighted-average molecular indices of the 14 environmental DOM samples, including DBE/C_w, H/C_w, AI_{modw}, N/C_w, NOSC_w, and O/C_w. The formula-matching rate represents the fraction of Mn-catalyzed product formulas that overlapped with formulas assigned in each environmental sample. Solid red lines indicate linear regressions, and shaded areas denote 95% confidence intervals. The corresponding R^2 and p values are shown in each panel. Detailed information on the sample type, source, and sampling location corresponding to sample IDs S1–S14 is provided in Table S2.

Downloaded from pubs.acs.org/esthag/article-supplement/5459299/pdf/es6c12201_si_001/ by guest on 10 November 2026



628

629 **Figure S20.** H_2O_2 formation during reactions of divalent cations with CGG. H_2O_2 was

630 detected using the $H_{32}Mo_7N_6O_{28}$/KI colorimetric method by monitoring the absorbance

631 at 352 nm during the reactions of (a) Ca^{2+}–CGG–O_2, (b) Mg^{2+}–CGG–O_2, (c) Ba^{2+}–

632 CGG–O_2, (d) CGG–O_2, (e) Mn^{2+}–O_2, (f) Mn^{2+}–CGG–N_2, (g) Mn^{2+}–GG–O_2, and (h)

633 Mn^{2+}–CGG–O_2. GG denotes the glucose–glycine system without catechol. (i) H_2O_2

634 concentration during the Mn^{2+}–CGG–O_2 reaction, calculated from the

635 $H_{32}Mo_7N_6O_{28}$/KI assay. Data are presented as mean ± SD (n = 2).

636

Downloaded from pubs.acs.org/esthag/article-supplement/5459299/pdf/es6c12201_si_001/ by guest on 10 November 2026

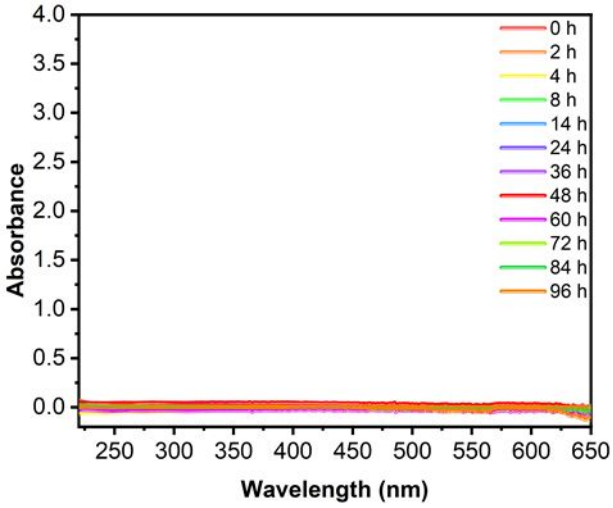
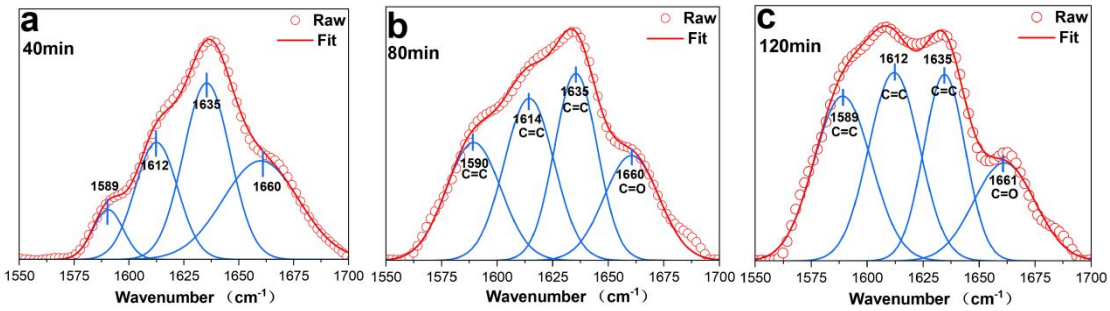


Figure S21: UV-vis spectra of Glu and Cly solution (GG) reacted with Mn^{2+} over 96 h. Experimental conditions: Glu = 6 mM, Gly = 6 mM, Mn^{2+} = 2 mM, pH = 8.0, 25 ℃, dark.

Downloaded from pubs.acs.org/esthag/article-supplement/5459299/pdf/es6c12201_si_001/ by guest on 10 November 2026



642

643 **Figure S22.** Peak deconvolution and fitting analysis of the ATR-FTIR spectra in the

644 1550–1700 cm^{-1} region during the reaction of CGG with Mn^{2+} at representative

645 reaction times: (a) 40 min, (b) 80 min, and (c) 120 min. The experimental spectra were

646 fitted using Gaussian functions, with adjusted R^2 values > 0.995.

647

Downloaded from pubs.acs.org/esthag/article-supplement/5459299/pdf/es6c12201_si_001/ by guest on 10 November 2026

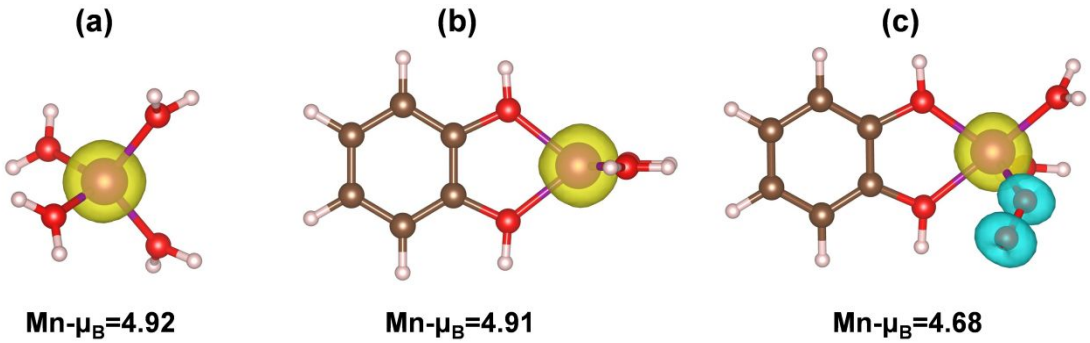


Figure S23: DFT-optimized geometries and spin densities of Mn complexes. (a) $[Mn(H_2O)_4]^{2+}$ (Mn^{2+}), (b) $[Mn(H_2O)_4]^{2+}$–catechol (Mn(II)-CT), and (c) $[Mn(H_2O)_4]^{2+}$–catechol–O_2 (Mn(II)-CT-O_2). The calculated atomic spin populations (μ_B) are indicated for each complex, reflecting the total number of unpaired electrons localized on the Mn center.

Downloaded from pubs.acs.org/esthag/article-supplement/5459299/pdf/es6c12201_si_001/ by guest on 10 November 2026

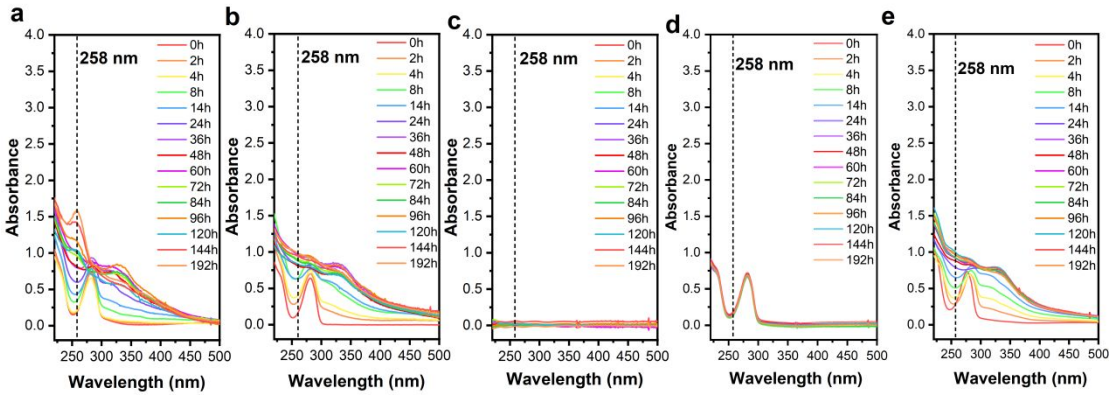


Figure S24. UV–vis characterization of the PP-trapping experiments. UV–vis spectra of the Mn^{2+}–CGG reaction in the presence (a) and absence (b) of sodium pyrophosphate (PP) under oxic conditions. (c) UV–vis spectra of Mn^{2+} with PP alone. (d) UV–vis spectra of the Mn^{2+}–CGG reaction in the presence of PP under anoxic (N_2) conditions. (e) UV–vis spectra of the Mn-depleted reaction solution after cation-exchange resin treatment (>99% removal of dissolved Mn), followed by PP addition and mixing for 1 h. Experimental conditions: CT = 2 mM, Glu = 6 mM, Gly = 6 mM, Mn^{2+} = 2 mM, PP = 40 mM, pH = 8.0, 25 °C, dark.

Downloaded from pubs.acs.org/esthag/article-supplement/s459299/pdf/es6c12201_si_001/ by guest on 10 November 2026

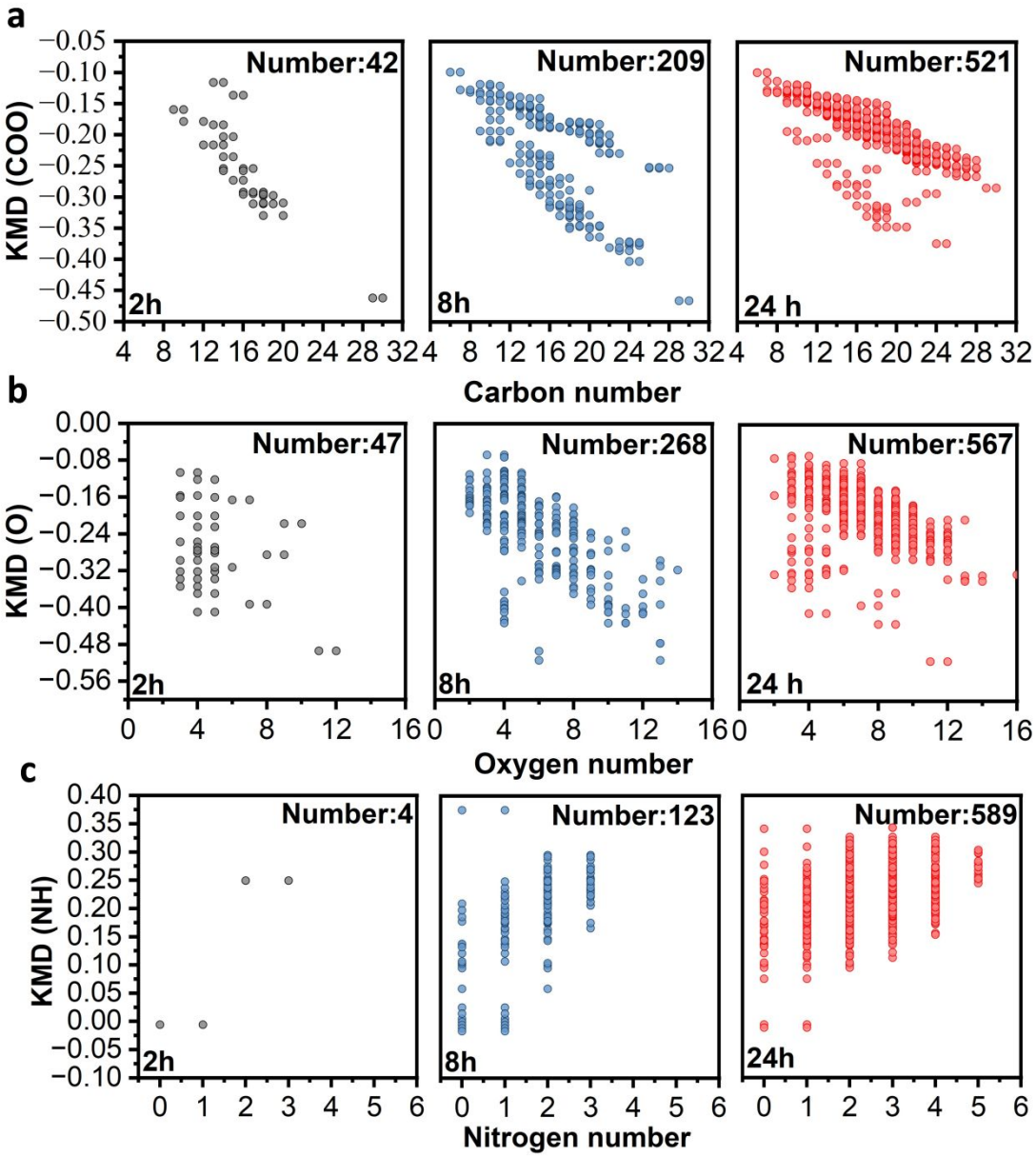
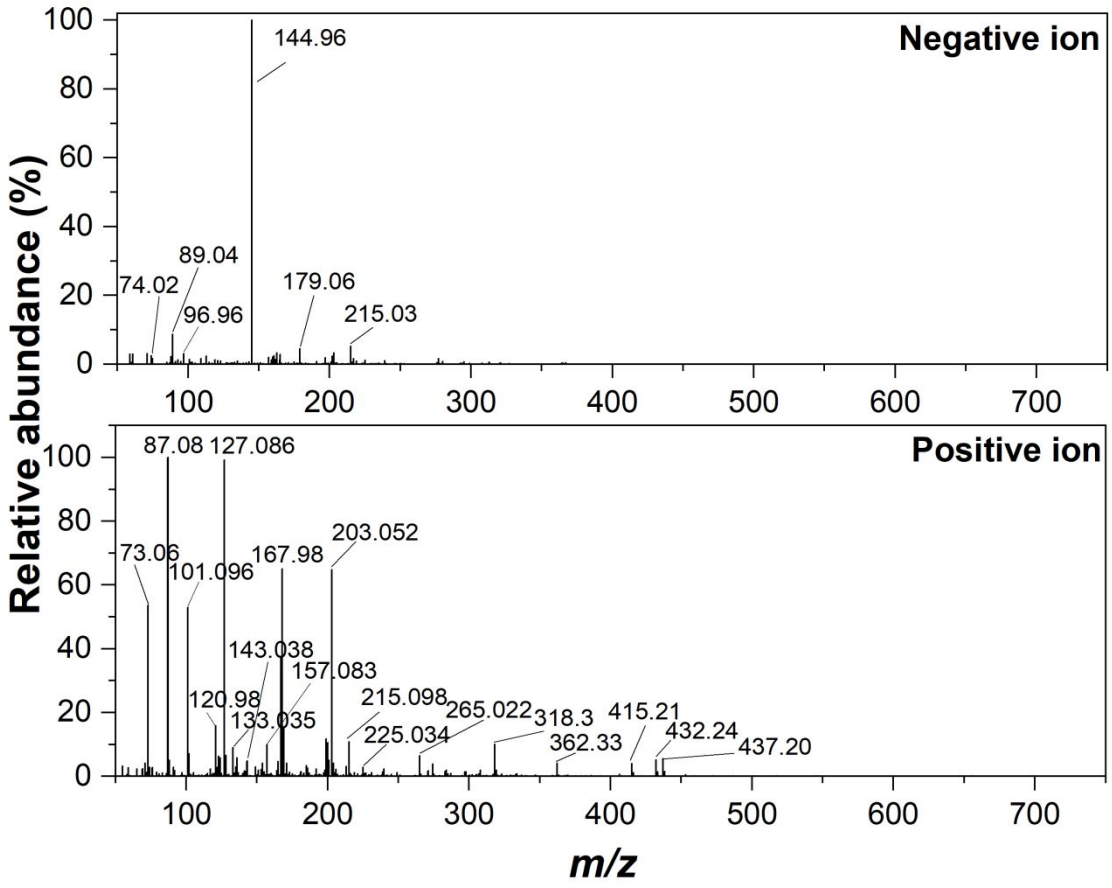


Figure S25: Kendrick mass defect (KMD) analysis of reaction products at 2 h, 8 h, and 24 h. (a) KMD(COO) versus carbon number, (b) KMD(O) versus oxygen number, and (c) KMD(NH) versus nitrogen number. The plot shows all molecules that share identical KMD values with at least one other molecule. Molecules within a homologous series—differing only in the number of COO, O, or NH—exhibit the same KMD and thus align along horizontal lines.

Downloaded from pubs.acs.org/esthag/article-supplement/5459299/pdf/es6c12201_si_001/ by guest on 10 November 2026



673

674 **Figure S26:** Q-Orbitrap-HRMS spectra of the products from the reaction of Mn^{2+}

675 with CGG.

676

Downloaded from pubs.acs.org/esthag/article-supplement/5459299/pdf/es6c12201_si_001/ by guest on 10 November 2026

677 **Table S1:** Classification of molecular compounds into major biochemical classes.

Molecular class	Critera
Carbohydrates	H/C:1.5-2.4; O/C:0.71-1.2
Amino sugars	H/C:1.5-2.2; O/C:0.52-0.71
Saturated compounds	H/C:1.5-2.2; O/C:0-0.52
Tannins	H/C:0.5-1.5; O/C:0.67-1.2
Lignins	H/C:0.7-1.5; O/C:0.1-0.67
Unsaturated hydrocarbons	H/C:0.7-1.5; O/C:0-0.1
Condensed aromatic structures	H/C:0.2-0.7; O/C:0-0.67

678 The classification method was from our previous study.[56]

679

Downloaded from pubs.acs.org/esthag/article-supplement/5459299/pdf/es6c12201_si_001/ by guest on 10 November 2026

680 **Table S2:** Description and geographic information of environmental DOM samples

681 analyzed by FT-ICR MS for molecular comparison.

Sample ID	Sample Type	City/Location	Province/Country	Coordinates	Reference
S1	Agricultural soil	Shehong City	Sichuan, China	30°48′18.69″N, 105°21′17.0″E	[34]
S2	Agricultural soil	Xianyang City	Shanxi, China	35°14′14″N, 107°42′56″E	[34]
S3	Agricultural soil	Suihua City	Heilongjiang, China	47°26′5.86″N, 126°47′38.06″E	[34]
S4	Agricultural soil	Xianning City	Hubei, China	29°55′42″N, 114°20′49″E	[34]
S5	Agricultural soil, paddy	Changsha City	Hunan, China	28°18′27.93″N, 112°46′28.25″E	[33]
S6	Agricultural soil, paddy	Zhanjiang City	Guangdong, China	20°22′17.04″N, 110°13′42.87″E	[33]
S7	Forest soil	Wuhan Botanical Garden	Hubei, China	30°32′43″N, 114°25′14″E	[34]
S8	River water	Yangtze River	Hubei, China	30°33′41.86″N, 114°18′13.46″E	[35]
S9	Agricultural soil	Chengmai County	Hainan, China	19°59′6″N, 110°19′36″E	[34]
S10	Lake water	East Lake, Wuhan City	Hubei, China	30°19′23.5″N, 114°14′35.6″E	[35]
S11	Agricultural soil	Ningbo City	Zhejiang, China	29°40′6.13″N, 121°37′7.93″E	[34]
S12	Standard river NOM	Suwannee River	Florida, USA	30°19′12″N, 82°45′00″W	[35]
S13	Agricultural soil, dryland	Zhanjiang City	Guangdong, China	20°22′22.31″N, 110°13′36.65″E	[33]
S14	Forest soil	Changsha City	Hunan, China	28°18′29.31″N, 112°46′18.51″E	[33]

682

Downloaded from pubs.acs.org/esthag/article-supplement/5459299/pdf/es6c12201_si_001/ by guest on 10 November 2026

683 **Table S3:** The fitting results of the Mn X-ray absorption near-edge structure

684 (XANES) spectroscopy were obtained using the Combo method.

Samples	Mn(IV)	Mn(III)	Mn(II)	*NSS*
δ-MnO_2	81.40 %	15.33 %	3.27 %	$4.4x10^{-5}$
γ-MnOOH	0 %	95.52 %	4.48 %	$1.23x10^{-4}$
$MnCl_2$	0 %	0 %	100 %	$0.23x10^{-4}$
Reaction sediments	0 %	0 %	100 %	$2.29x10^{-4}$
Reaction solution	0 %	0 %	100 %	$3.3x10^{-4}$

685 *NSS* is the normalized sum-squared residual = $\sum_n[\text{data} - \text{fit}]^2 / \sum_n[\text{data}]^2$.

686

Downloaded from pubs.acs.org/esthag/article-supplement/5459299/pdf/es6c12201_si_001/ by guest on 10 November 2026

687 **Table S4:** The fitting results of high-resolution X-ray photoelectron spectroscopy
688 (XPS) for C 1s, O 1s, and N 1s spectra.

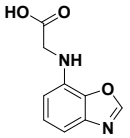
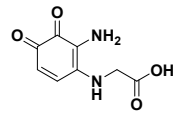
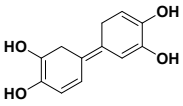
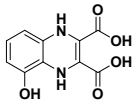
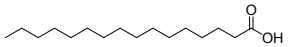
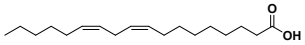
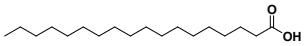
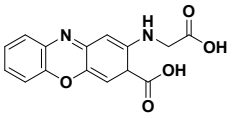
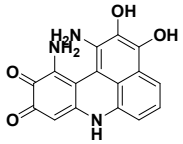
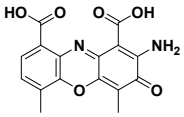
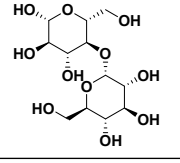
XPS spectra	Peak position (eV)	Functional group	Percentage (%)
C 1s	284.65	C-(C, H)	51.38
	286.3	C-(O, N)	35.95
	288	C=O, O-C-O	7.91
	289.1	C=O-OH	4.76
N 1s	399.2	Aromatic N	17.16
	400.4	Peptide bond N	51.68
	402.2	Primary amine N	31.16
O 1s	529.6	Mn-O-Mn	1.28
	531.3	O=N-C/O=C	44.15
	532.5	C-O-H	26.94
	533.7	C-O-C/COOH	23.53
	535	C-O-O-C/H_2O	4.1

689
690

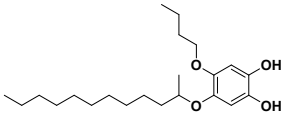
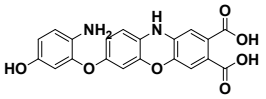
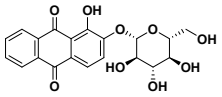
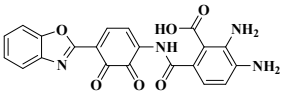
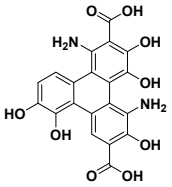
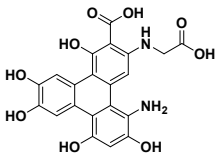
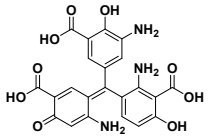
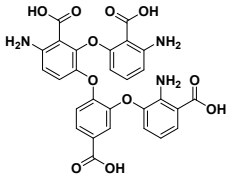
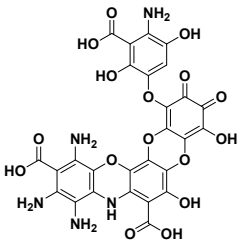
Downloaded from pubs.acs.org/esthag/article-supplement/s459299/pdf/es6c12201_si_001/ by guest on 10 November 2026

691 **Table S5:** Proposed molecular structures based on FT-ICR MS mass spectra in

692 negative ion mode.

m/z	Molecular formula	Structural formula
109.0295	F1: $C_6H_6O_2$ (M-1)	
191. 04662	F2: $C_9H_8O_3N_2$ (M-1)	
195.04113	F3: $C_8H_8O_2N_4$ (M-1)	
219.04113	F4: $C_{12}H_{12}O_4$ (M-1)	
235.03605	F5: $C_{10}H_8O_5N_2$ (M-1)	
255.23298	F6: $C_{16}H_{32}O_2$ (M-1)	
279.232953	F7: $C_{18}H_{32}O_2$ (M-1)	
283.26428	F8: $C_{18}H_{36}O_2$ (M-1)	
299.06735	F9: $C_{15}H_{12}O_5N_2$ (M-1)	
308.06768	F10: $C_{16}H_{11}O_4N_3$ (M-1)	
327.06226	F11: $C_{16}H_{12}O_6N_2$ (M-1)	
341.1089384	F12: $C_{12}H_{22}O_{11}$ (M-1)	

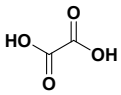
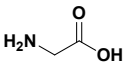
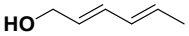
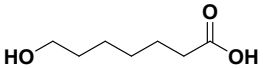
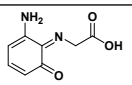
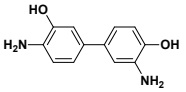
Downloaded from pubs.acs.org/esthag/article-supplement/5459299/pdf/es6c12201_si_001/ by guest on 10 November 2026

365.2697513	F13: $C_{22}H_{38}O_4$ (M-1)	
393.072868	F14: $C_{20}H_{14}O_7N_2$ (M-1)	
401.0878062	F15: $C_{20}H_{18}O_9$ (M-1)	
417.08406	F16: $C_{21}H_{14}O_6N_2$ (M-1)	
425.06265	F17: $C_{20}H_{14}O_9N_2$ (M-1)	
439.0783	F18: $C_{21}H_{16}O_9N_2$ (M-1)	
466.0892	F19: $C_{22}H_{17}O_9N_3$ (M-1)	
574.110331	F20: $C_{28}H_{21}O_{11}N_3$ (M-1)	
666.05975	F21: $C_{27}H_{17}O_{16}N_5$ (M-1)	

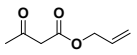
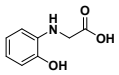
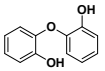
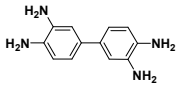
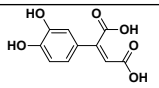
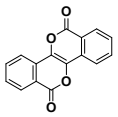
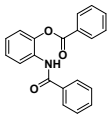
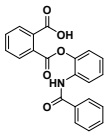
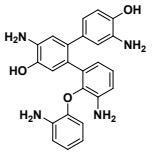
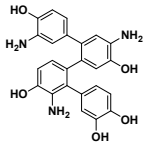
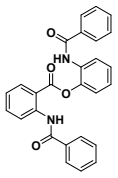
Downloaded from pubs.acs.org/esthag/article-supplement/s459299/pdf/es6c12201_si_001/ by guest on 10 November 2026

694 **Table S6:** Proposed molecular structures based on Q-Orbitrap-HRMS spectra in

695 negative and positive ion modes.

m/z	Molecular formula	Structural formula
Negative ion		
89.04	H1: $C_2H_2O_4$ (M-1)	
74.024	H2: C_2H_5NO (M-1)	
96.96	H3: $C_6H_{10}O$ (M-1)	
144.963	H4: $C_7H_{14}O_3$ (M-1)	
179.06	H5: $C_8H_8N_2O_3$(M-1)	
215.03	H6: $C_{12}H_{12}N_2O_2$(M-1)	
Positive ion		
73.06	H7: C_4H_8O (M+1)	
87.08	H8: $C_5H_{10}O$ (M+1)	
101.095	H9: $C_5H_8O_2$ (M+1)	
120.98	H10: C_7H_7NO (M)	
127.086	H11: $C_6H_6O_3$ (M+1)	
135.97	H12: $C_7H_5NO_2$ (M+1)	

Downloaded from pubs.acs.org/esthag/article-supplement/5459299/pdf/es6c12201_si_001/ by guest on 10 November 2026

143.067	H13: $C_7H_{10}O_3$ (M+1)	
167.98	H14: $C_8H_9NO_3$ (M+1)	
203.05	H15: $C_{12}H_{10}O_3$ (M+1)	
215.098	H16: $C_{12}H_{14}N_4$ (M+1)	
225.035	H17: $C_{10}H_8O_6$ (M+1)	
265.02	H18: $C_{16}H_8O_4$ (M+1)	
318.301	H19: $C_{20}H_{15}NO_3$ (M+1)	
362.327	H20: $C_{21}H_{15}NO_5$ (M+1)	
415.212	H21: $C_{24}H_{21}N_3O_4$ (M+1)	
432.238	H22: $C_{24}H_{21}N_3O_5$ (M+1)	
437.20	H23: $C_{27}H_{19}N_2O_4$ (M+1)	

Proposed structural formulas were derived from the Q-Orbitrap-HRMS spectra presented in Figure S26. The term (M-1) denotes the peak resulting from the loss of one hydrogen atom, while (M) indicates the molecular ion peak corresponding to the intact molecule. Additionally, (M+1) signifies the peak representing the addition of one hydrogen atom.

Downloaded from pubs.acs.org/esthag/article-supplement/5459299/pdf/es6c12201_si_001/ by guest on 10 November 2026

701

Downloaded from pubs.acs.org/esthag/article-supplement/5459299/pdf/es6c12201_si_001/ by guest on 10 November 2026

Table S7: Summary of peak positions and corresponding functional groups in the ATR-FTIR spectra of formed humic-like acids.

Peak position (cm^{-1})	Vibration	Band assignments
1720	C=O	Carboxylic acids, ketones[57, 58, 59]
1625	C=C	Aromatic rings[45, 57, 58]
1605	C=C	Aromatic rings[59, 60]
1497	C=C	Aromatic rings[61]
1389	C-O/OH	Carboxylic acids[62]/Phenolic defomation[60]
1277-1288	C-O/NO_2	Aryl ethers[45, 63]/Organic nitrate[64, 65]
1240	C-N/C-O-C	AmideIII[59]/Aromatic ether[66]
1136	C-O	Alcohols/Ethers[45]
1036	C-O/C-O-C	Alcohols, Ethers, and Carbohydrates[67]/Ethers[45, 68]
965	NH_2	[69]
875	C-H	Aromatic rings with isolated aromatic hydrogens[45]
825	C-H	Aromatic rings with two adjacent aromatic hydrogens[45]
753	C-H	Aromatic rings four adjacent aromatic hydrogens[45]
708	C-H	Aromatic rings[45]

Downloaded from pubs.acs.org/esthag/article-supplement/5459299/pdf/es6c12201_si_001/ by guest on 10 November 2026

REFERENCE

(1) McKenzie, R. M. The synthesis of birnessite, cryptomelane, and some other oxides and hydroxides of manganese. *Mineral. Mag.* **1971**, *38* (296), 493–502.

(2) Duckworth, O. W.; Sposito, G. Siderophore–Manganese(III) Interactions II. Manganite Dissolution Promoted by Desferrioxamine B. *Environ. Sci. Technol.* **2005**, *39* (16), 6045–6051.

(3) Kostka, J. E.; Luther, G. W., III; Nealson, K. H. Chemical and biological reduction of Mn(III)-pyrophosphate complexes: Potential importance of dissolved Mn(III) as an environmental oxidant. *Geochim. Cosmochim. Acta* **1995**, *59* (5), 885–894.

(4) Trouwborst, R. E.; Clement, B. G.; Tebo, B. M.; Glazer, B. T.; Luther, G. W., III. Soluble Mn(III) in Suboxic Zones. *Science* **2006**, *313* (5795), 1955–1957.

(5) Qi, G.; Yue, D.; Fukushima, M.; Fukuchi, S.; Nie, Y. Enhanced humification by carbonated basic oxygen furnace steel slag–I. Characterization of humic-like acids produced from humic precursors. *Bioresour. Technol.* **2012**, *104*, 497–502..

(6) Zhang, X.; Zong, Y.; Xu, L.; Mao, Y.; Wu, D. Enhanced abiotic integrated polyphenol-Maillard humification by Mg/Fe layered double hydroxide (LDH): Role of Fe(III)-polyphenol complexation. *Chem. Eng. J.* **2021**, *425*, 130521.

(7) Shindo, H.; Huang, P. M. Role of Mn(IV) oxide in abiotic formation of humic substances in the environment. *Nature* **1982**, *298*, 363–365.

(8) Hardie, A. G.; Dynes, J. J.; Kozak, L. M.; Huang, P. M. Biomolecule-induced carbonate genesis in abiotic formation of humic substances in nature. *Can. J. Soil Sci.* **2009**, *89* (4), 445–453.

Downloaded from pubs.acs.org/esthag/article-supplement/5459299/pdf/es6c12201_si_001/ by guest on 10 November 2026

(9) Jokić, A.; Frenkel, A. I.; Huang, P. M. Effect of light on birnessite catalysis of the Maillard reaction and its implication in humification. *Can. J. Soil Sci.* **2001**, *81* (3), 277–283.

(10) Zhang, Y.; Yue, D.; Fang, D.; Dong, X.; Li, W. Enhanced darkening effect from the interaction of MnO_2 and oxygen on the component evolution of amino-phenolic humic-like substances. *Chemosphere* **2021**, *263*, 127956.

(11) Zhang, Y.; Yue, D.; Wang, X.; Song, W. Mechanism of oxidation and catalysis of organic matter abiotic humification in the presence of MnO_2. *J. Environ. Sci.* **2019**, *77*, 167–173.

(12) Ohno, T. Fluorescence inner filtering correction for determining the humification index of dissolved organic matter. *Environ. Sci. Technol.* **2002**, *36* (4), 742–746.

(13) Peng, H.; Yang, H.; Han, J.; Liu, X.; Su, D.; Yang, T.; Liu, S.; Pao, C.-W.; Hu, Z.; Zhang, Q.; Xu, Y.; Geng, H.; Huang, X. Defective $ZnIn_2S_4$ nanosheets for visible light and sacrificial agent free H_2O_2 photosynthesis via O_2/H_2O redox. *J. Am. Chem. Soc.* **2023**, *145* (50), 27757–27766.

(14) Zhong, C.; Cao, H.; Huang, Q.; Xie, Y.; Zhao, H. Degradation of sulfamethoxazole by manganese(IV) oxide in the presence of humic acid: role of stabilized semiquinone radicals. *Environ. Sci. Technol.* **2023**, *57* (36), 13625–13634.

(15) Ulas, G.; Lemmin, T.; Wu, Y.; Gassner, G. T.; DeGrado, W. F. Designed metalloprotein stabilizes a semiquinone radical. *Nat. Chem.* **2016**, *8*, 354–359.

(16) Ozaki, Y.; Czarnik-Matusewicz, B.; Šašić, S. Two-Dimensional Correlation Spectroscopy in Analytical Chemistry. *Anal. Sci. Suppl.* **2002**, *17icas*, i663–i666.

Downloaded from pubs.acs.org/esthag/article-supplement/5459299/pdf/es6c12201_si_001/ by guest on 10 November 2026

(17) Li, X.; Yang, P.; Zhao, W.; Guo, F.; Jaisi, D.-P.; Mi, S.; Ma, H.; Lin, B.; Feng, X.; Tan, W.; Wang, X. Adsorption mechanisms of glyphosate on ferrihydrite: effects of Al substitution and aggregation state. *Environ. Sci. Technol.* **2023**, *57* (38), 14384–14395.

(18) Manceau, A.; Marcus, M. A.; Grangeon, S. Determination of Mn valence states in mixed-valent manganates by XANES spectroscopy. *Am. Mineral.* **2012**, *97* (5–6), 816–827.

(19) Omoike, A.; Chorover, J. Spectroscopic study of extracellular polymeric substances from *Bacillus subtilis*: Aqueous chemistry and adsorption effects. *Biomacromolecules* **2004**, *5* (4), 1219–1230.

(20) Zhang, M.; Peacock, C. L.; Cai, P.; Xiao, K.-Q.; Qu, C.; Wu, Y.; Huang, Q. Selective retention of extracellular polymeric substances induced by adsorption to and coprecipitation with ferrihydrite. *Geochim. Cosmochim. Acta* **2021**, *299*, 15–34.

(21) Poggenburg, C.; Mikutta, R.; Liebmann, P.; Koch, M.; Guggenberger, G. Siderophore-promoted dissolution of ferrihydrite associated with adsorbed and coprecipitated natural organic matter. *Org. Geochem.* **2018**, *125*, 177–188.

(22) Abe, T.; Watanabe, A. X-ray Photoelectron Spectroscopy of Nitrogen Functional Groups in Soil Humic Acids. *Soil Sci.* **2004**, *169* (1), 35–43.

(23) Shaikh, N.; Taujale, S.; Zhang, H.; Artyushkova, K.; Ali, A.-M. S.; Cerrato, J. M. Spectroscopic investigation of interfacial interaction of manganese oxide with triclosan, aniline, and phenol. *Environ. Sci. Technol.* **2016**, *50* (20), 10978–10987.

(24) Neese, F. The ORCA program system. *Wiley Interdiscip. Rev.: Comput. Mol. Sci.* **2012**, *2* (1), 73–78.

Downloaded from pubs.acs.org/esthag/article-supplement/5459299/pdf/es6c12201_si_001/ by guest on 10 November 2026

(25) Tao, J.; Perdew, J. P.; Staroverov, V. N.; Scuseria, G. E. Climbing the density functional ladder: Nonempirical meta–generalized gradient approximation designed for molecules and solids. *Phys. Rev. Lett.* **2003**, *91* (14), 146401.

(26) Grimme, S.; Ehrlich, S.; Goerigk, L. Effect of the damping function in dispersion corrected density functional theory. *J. Comput. Chem.* **2011**, *32* (7), 1456–1465.

(27) Staroverov, V. N.; Scuseria, G. E.; Tao, J.; Perdew, J. P. Comparative assessment of a new nonempirical density functional: Molecules and hydrogen-bonded complexes. *J. Chem. Phys.* **2003**, *119* (23), 12129–12137.

(28) Li, W.-L.; Li, Y.; Li, J.; Head-Gordon, T. How thermal fluctuations influence the function of the FeMo cofactor in nitrogenase enzymes. *Chem Catalysis* **2023**, *3* (7), 100662.

(29) Weigend, F.; Ahlrichs, R. Balanced basis sets of split valence, triple zeta valence and quadruple zeta valence quality for H to Rn: Design and assessment of accuracy. *Phys. Chem. Chem. Phys.* **2005**, *7* (18), 3297–3305.

(30) Wu, S.; Feng, Y.; Chen, X.; Fu, Q.-L.; Dong, H.; Yang, X.; Ma, R.; Fu, P.; Wang, Y. Deciphering the effects of quenching on the chemodiversity of low and non volatile disinfection byproducts in drinking source water using ESI(−)-FT-ICR MS. *Environ. Sci. Technol.* **2025**, *59* (33), 17834–17845.

(31) Jiang, F.; Su, H.; Fu, Q.-L.; Yang, Z.; Wang, X.; Yin, H.; Tan, W.; Lanson, B.; Feng, X. Manganese oxides drive divergent fates of litter-derived DOM via pH-regulated oxidative decomposition and polymerization. *Environ. Sci. Technol.* **2025**, *59* (47), 25251–25264.

Downloaded from pubs.acs.org/esthag/article-supplement/5459299/pdf/es6c12201_si_001/ by guest on 10 November 2026

(32) Chen, H.; Shan, X.; Qiu, X.; Ding, L.; Liang, X.; Guo, X. High-resolution mass spectrometry combined with reactive oxygen species reveals differences in photoreactivity of dissolved organic matter from microplastic sources in aqueous environments. *Environ. Sci. Technol.* **2024**, *58* (23), 10334–10346.

(33) Wang, W.; Fang, X.; Fu, Q.-L.; Huang, C.; Fang, L.; Zhang, J.; Feng, X.; Tan, W.; Liu, F.; Li, J.; Yin, H.Iron(II/III) alters the relative roles of the microbial byproduct and humic acid during chromium(VI) reduction and fixation by soil dissolved organic matter. *Environ. Sci. Technol.* **2025**, *59* (5), 2778–2790.

(34) Zhuo, S.; Qin, R.; Fu, Q.-L. Chemodiversity of soil dissolved organic matter complementally improved by stepwise elution and electrospray ionization modes. *Org. Geochem.* **2025**, *203*, 104965.

(35) Chen, X.; Fu, Q.-L.; Sun, Z. Effects of eluate drying on the chemodiversity of dissolved organic matter revealed by ultrahigh resolution mass spectrometry. *ACS Meas. Sci. Au* **2025**, *5* (4), 461–468.

(36) Liptak, M. D.; Gross, K. C.; Seybold, P. G.; Feldgus, S.; Shields, G. C. Absolute pKa determinations for substituted phenols. *J. Am. Chem. Soc.* **2002**, *124* (22), 6421–6427.

(37) Thapa, B.; Schlegel, H. B. Improved pKa prediction of substituted alcohols, phenols, and hydroperoxides in aqueous medium using density functional theory and a cluster-continuum solvation model. *J. Phys. Chem. A* **2017**, *121* (24), 4698–4706.

(38) Pillar-Little, E. A.; Guzman, M. I. Oxidation of substituted catechols at the air–water interface: production of carboxylic acids, quinones, and polyphenols. *Environ.*

Downloaded from pubs.acs.org/esthag/article-supplement/5459299/pdf/es6c12201_si_001/ by guest on 10 November 2026

Sci. Technol. **2017**, *51* (9), 4951–4959.

(39) Pillar-Little, E. A.; Camm, R. C.; Guzman, M. I. Catechol oxidation by ozone and hydroxyl radicals at the air–water interface. *Environ. Sci. Technol.* **2014**, *48* (24), 14352–14360.

(40) Stone, A. T. Reductive dissolution of manganese(III/IV) oxides by substituted phenols. *Environ. Sci. Technol.* **1987**, *21* (10), 979–988.

(41) Li, M.; Ling, C.; Zhao, L.; Hu, L.; Li, H.; Zhang, L. Surface Fe(IV)═O induced highly selective phenol polymerization via proton-coupled electron transfer. *J. Am. Chem. Soc.* **2025**, *147* (34), 31165–31174.

(42) Chen, W.; Westerhoff, P.; Leenheer, J. A.; Booksh, K. Fluorescence excitation–emission matrix regional integration to quantify spectra for dissolved organic matter. *Environ. Sci. Technol.* **2003**, *37* (24), 5701–5710.

(43) Wang, Z.; Jia, H.; Zhao, H.; Zhang, R.; Zhang, C.; Zhu, K.; Guo, X.; Wang, T.; Zhu, L. Oxygen limitation accelerates regeneration of active sites on a MnO_2 surface: promoting transformation of organic matter and carbon preservation. *Environ. Sci. Technol.* **2022**, *56* (13), 9806–9815.

(44) Doskočil, L.; Burdíková-Szewieczková, J.; Enev, V.; Kalina, L.; Wasserbauer, J. Spectral characterization and comparison of humic acids isolated from some European lignites. *Fuel* **2018**, *213*, 123–132.

(45) Ibarra, J. V.; Muñoz, E.; Moliner, R. FTIR study of the evolution of coal structure during the coalification process. *Org. Geochem.* **1996**, *24* (6–7), 725–735.

(46) Watanabe, A.; McPhail, D. B.; Maie, N.; Kawasaki, S.; Anderson, H. A.; Cheshire,

Downloaded from pubs.acs.org/esthag/article-supplement/5459299/pdf/es6c12201_si_001/ by guest on 10 November 2026

837 M. V. Electron spin resonance characteristics of humic acids from a wide range of soil
838 types. *Org. Geochem.* **2005**, *36* (7), 981–990.
839 (47) Pan, B.; Li, H.; Lang, D.; Xing, B. Environmentally persistent free radicals:
840 Occurrence, formation mechanisms and implications. *Environ. Pollut.* **2019**, *248*, 320–
841 331.
842 (48) Li, H.; Pan, B.; Liao, S. H.; Zhang, D.; Xing, B. S. Formation of environmentally
843 persistent free radicals as the mechanism for reduced catechol degradation on
844 hematite-silica surface under UV irradiation. *Environ. Pollut.* **2014**, *188*, 153–158.
845 (49) Shi, Y.; Zhang, C.; Liu, J.; Dai, Q.; Jiang, Y.; Xi, M.; Jia, H. Distribution of
846 persistent free radicals in different molecular weight fractions from peat humic acids
847 and their impact in reducing goethite. *Sci. Total Environ.* **2021**, *797*, 149173.
848 (50) Lang, D.; Jiang, F.; Gao, X.; Yi, P.; Liu, Y.; Li, H.; Chen, Q.; Pan, B.; Xing, B.
849 Generation of environmentally persistent free radicals on faceted TiO_2 in an ambient
850 environment: roles of crystalline surface structures. *Environ. Sci.: Nano* **2022**, *9* (7),
851 2521–2533.
852 (51) Peng, Y.; Chen, Q.; Li, H.; Lang, D.; Zhao, Q.; Pan, B.; Xing, B. A comparative
853 study on the formation of environmentally persistent free radicals (EPFRs) on hematite
854 and goethite: contribution of various catechol degradation byproducts. *Environ. Sci.*
855 *Technol.* **2019**, *53* (23), 13713–13719.
856 (52) Jia, H.; Zhao, S.; Shi, Y.; Zhu, L.; Wang, C.; Sharma, V. K. Transformation of
857 polycyclic aromatic hydrocarbons and formation of environmentally persistent free
858 radicals on modified montmorillonite: the role of surface metal ions and polycyclic

Downloaded from pubs.acs.org/esthag/article-supplement/5459299/pdf/es6c12201_si_001/ by guest on 10 November 2026

aromatic hydrocarbon molecular properties. *Environ. Sci. Technol.* **2018**, *52* (10), 5725–5733.

(53) Jia, H.; Nulaji, G.; Gao, H.; Wang, F.; Zhu, Y.; Wang, C. Formation and stabilization of environmentally persistent free radicals induced by the interaction of anthracene with Fe(III)-modified clays. *Environ. Sci. Technol.* **2016**, *50* (12), 6310–6319.

(54) Saab, S. C.; Martin-Neto, L. Studies of semiquinone free radicals by ESR in the whole soil, HA, FA and humin substances. *J. Braz. Chem. Soc.* **2004**, *15* (1), 34–37.

(55) Piccolo, A. The supramolecular structure of humic substances. *Soil Sci.* **2001**, *166* (11), 810–832.

(56) Fu, Q.-L.; Fujii, M.; Riedel, T. Development and comparison of formula assignment algorithms for ultrahigh-resolution mass spectra of natural organic matter. *Anal. Chim. Acta* **2020**, *1125*, 247–257.

(57) Tao, W.; Zhang, P.; Li, H.; Yang, Q.; Oleszczuk, P.; Pan, B. Generation mechanism of persistent free radicals in lignocellulose-derived biochar: roles of reducible carbonyls. *Environ. Sci. Technol.* **2022**, *56* (15), 10638–10645.

(58) Parsons, J. W. Humus Chemistry—Genesis, Composition, Reactions. *Soil Sci.* 1983, *135* (2), 129–130.

(59) Smidt, E.; Meissl, K. The applicability of Fourier transform infrared (FT-IR) spectroscopy in waste management. *Waste Manag.* **2007**, *27* (2), 268–276.

(60) Guo, X.-J.; He, X.-S.; Li, C.-W.; Li, N.-X. The binding properties of copper and lead onto compost-derived DOM using Fourier-transform infrared, UV-vis and

Downloaded from pubs.acs.org/esthag/article-supplement/5459299/pdf/es6c12201_si_001/ by guest on 10 November 2026

881 fluorescence spectra combined with two-dimensional correlation analysis. *J. Hazard.*
882 *Mater.* **2019**, *365*, 457–466.
883 (61) Gao, X.; Tan, W.; Zhao, Y.; Wu, J.; Sun, Q.; Qi, H.; Xie, X.; Wei, Z. Diversity in
884 the mechanisms of humin formation during composting with different materials.
885 *Environ. Sci. Technol.* **2019**, *53* (7), 3653–3662.
886 (62) Mitchell, G. D.; Davis, A.; Chander, S. Surface properties of photo-oxidized
887 bituminous vitrains. *Int. J. Coal Geol.* **2005**, *62* (1–2), 33–47.
888 (63) Busetti, F.; Berwick, L.; McDonald, S.; Heitz, A.; Joll, C.; Loh, J.; Power, G.
889 Physicochemical characterization of organic matter in Bayer liquor. *Ind. Eng. Chem.*
890 *Res.* **2014**, *53* (15), 6544–6553.
891 (64) Bruns, E. A.; Perraud, V.; Zelenyuk, A.; Ezell, M. J.; Johnson, S. N.; Yu, Y.; Imre,
892 D.; Finlayson-Pitts, B. J.; Alexander, M. L. Comparison of FTIR and particle mass
893 spectrometry for the measurement of particulate organic nitrates. *Environ. Sci. Technol.*
894 **2010**, *44* (3), 1056–1061.
895 (65) Kirchner, U.; Scheer, V.; Vogt, R. FTIR Spectroscopic investigation of the
896 mechanism and kinetics of the heterogeneous reactions of NO_2 and HNO_3 with soot. *J.*
897 *Phys. Chem. A* **2000**, *104* (39), 8908–8915.
898 (66) Hamciuc, C.; Lisa, G.; Hamciuc, E.; Epure, E.-L.; Tudorachi, N. Thermal behavior
899 study and degradation mechanism by TG/MS/FTIR technique of some poly(aryl ether
900 ether ketone)s. *J. Anal. Appl. Pyrolysis* **2020**, *150*, 104877.
901 (67) Xue, S.; Zhao, Q.-L.; Wei, L.-L.; Ren, N.-Q. Behavior and characteristics of
902 dissolved organic matter during column studies of soil aquifer treatment. *Water Res.*

Downloaded from pubs.acs.org/esthag/article-supplement/5459299/pdf/es6c12201_si_001/ by guest on 10 November 2026

903 **2009**, *43* (2), 499–507.

904 (68) Socrates, G. Infrared and Raman characteristic group frequencies: Tables and

905 Charts, 3rd ed.; John Wiley & Sons: Chichester, U.K., **2001**.

906 (69) Zhang, H.; Magoshi, J.; Becker, M.; Chen, J. Y.; Matsunaga, R. Thermal properties

907 of *Bombyx mori* silk fibers. *J. Appl. Polym. Sci.* **2002**, *86* (8), 1817–1820.

908

Downloaded from pubs.acs.org/esthag/article-supplement/5459299/pdf/es6c12201_si_001/ by guest on 10 November 2026